FACULTY OF SCIENCE
UNIVERSITY OF COPENHAGEN

Master's Thesis in Physics

Maria Chatzieleftheriou

Iron-based Superconductors

Electronic correlations and orbital selectivity

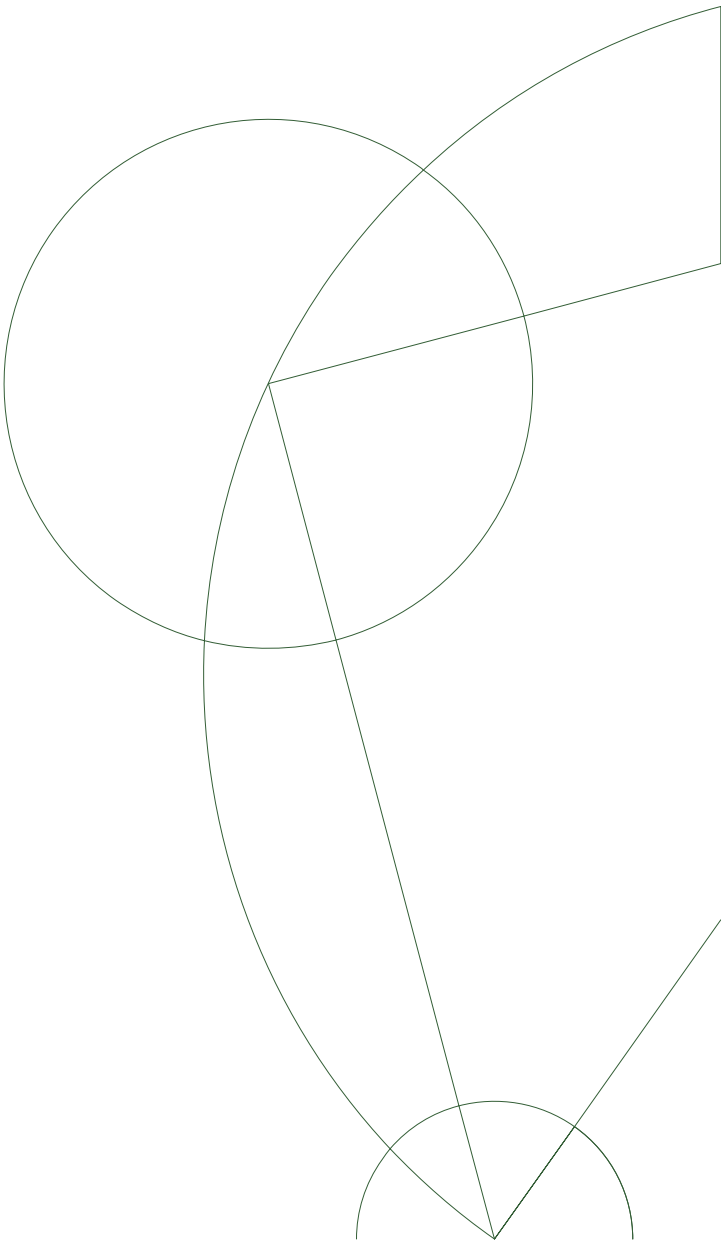

Supervisor: Brian M. Andersen

04/09/2017

Abstract

A common belief is that the multi-orbital character of the high-T_c iron-based superconductors plays a major role in the physical processes. In this thesis we apply two methods to assess the strength of electronic correlations in these materials. We use a local slave spin method to show the presence of a strong mass renormalization, as well as the emergence of an orbital selective phase, with co-existence of weakly and strongly correlated electrons. In order to include the momentum dependence of the self-energy and estimate its impact on the correlations, we consider the effect of spin fluctuations. Furthermore, motivated by a recent experiment carried out on iron selenide, we investigate whether a small energy difference between the xz and yz iron d-orbitals in the nematic phase of the system, can be accompanied by a large discrepancy in their quasiparticle weights, thus in their degree of correlation. We show qualitatively that indeed, if the system in the nematic state is close to a magnetic instability, such an effect can be observed.

Acknowledgements

First of all, I would like to thank Brian for welcoming me in the superconducting family. Thank you for guiding me throughout the year and of course for introducing me to "The obsession". I learned a lot from you, tak!
A super special thanks to you, store Daniel for being extremely patient and always answering my never-ending questions.
Thank you Morten for being a savior when my slave spin code was driving me crazy, and for reminding me that I am doing better than I think I am.
Thank you Kristofer for sharing the passion to get the self-energy code to work.
Thanks Peter Hirschfeld and Andreas Kreisel for valuable conversations.
I would also like to thank the members of the CMT group for making everyday-office-life enjoyable. Especially thank you lille Daniel for being an awesome office-mate, thank you Carlos for telling me to DO IT and of course thanks to you Panos for the general supervision.
A huge thank you to the habitants of my CPH bubble, for sharing with me two years full of beautiful memories.
Finally, to my family...thank you for always supporting me and being there for me, even from lots and lots of kilometers away!

Contents

Chapter 1

Introduction to the iron-based superconductors

Superconductivity was first discovered in the beginning of the 20th century, more specifically in 1911 by H. K. Onnes [1], while he was studying solid mercury and its resistance at cryogenic temperatures, using liquid helium. He found that at T=4.2K the resistance suddenly dropped to zero. Since then more materials exhibiting this abnormal behavior were found, but it was only in the 1950's when the scientific community managed to explain the mechanism leading to it. After the important input by V. L. Ginzburg and L. Landau with their theory [2] at the beginning of the decade, it was in 1957 when J. Bardeen, L. Cooper and J. R. Schrieffer formulated the so-called BCS theory of superconductivity [3], that microscopically described the phenomenon as the generation of electron pairs ("Cooper pairs") mediated by phonons.

All the materials that had been found to be superconducting exhibited this behavior below a critical temperature that was of the order of a few Kelvins. In 1986, though, G. Bednorz and K. A. Muller discovered superconductivity in ceramics [4] and shortly after more compounds of copper and oxygen were found with transition temperatures exceeding $T = 100K$ [5]. These constitute the family of the so-called cuprates. The most surprising aspect of these materials is that magnetism exists close to superconductivity, despite their antagonistic nature and it turns out that the electron pairing is not mediated by phonons. This means that there must be another mechanism leading to superconductivity and scientists have struggled to come up with a theory for it.

1.1 Fe-based superconductors

In 2008 Y. Kamihara et al. found that LaFeAsO becomes superconducting at T=26K [6], and that finding opened the road for the discovery of multiple iron-based materials that exhibit high critical temperature superconductivity (T_c>50K). Even though the iron-based superconductors (FeSC) for now do not reach the critical temperatures of the cuprates, they both belong to the family of the "unconventional superconductors", meaning superconductors that are not related to phonon-mediated interactions. The full understanding of the pairing mechanism associated with the FeSC is very important, because it can set the basis for theoretical predictions of more compounds, exhibiting superconducting properties, even in room temperature.

1.2 Crystal and electronic structure

There are various types within the family of the FeSC, but they all share a common feature in their crystal structure. The chemical block that appears in all of them is a layer (actually a tri-layer that we call FeX), which consists of a plane of iron atoms, above and below which there is an atomic layer of elements within the pnictogen or chalcogen groups, such as As, P, S, Se and Te. The planes of those elements above and below the iron one are arranged in an alternating pattern, as shown in Fig.1.1. According to the relevant group of the X element, the compounds are categorized into iron-pnictides and iron-chalcogenides.

In some compounds these tri-layers appear subsequently one after the other, creating in this way the whole structure. In other compounds there is a different layer separating the FeX blocks between them. The existence of those "bridging" layers and their amount in the chemical composition give rise to certain families within the FeSC. The ratio between the different element concentrations can be directly read off from the formula of each compound and that is identified as the family name, for example FeSe is part of the 11-family, while $SrFe_2As_2$ is part of the 122-family. In figure 1.1 we can see some examples of the most commonly met families, where the FeX tri-layer is illustrated with a yellow stripe.

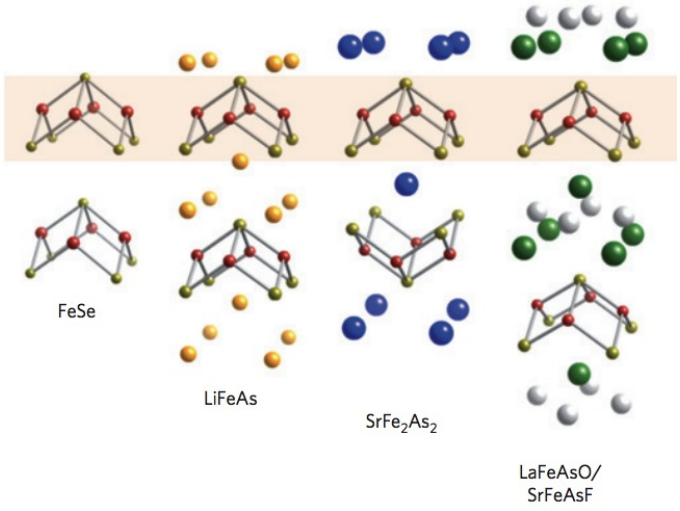

Figure 1.1: Crystal structure of some FeSC. From their formulas we can read off the families they belong to: FeSe 11, LiFeAs 111, $SrFe_2As_2$ 122, LaFeAsO/SrFeAsF 1111. From [7].

The average distance between the iron atoms in plane throughout all of those compounds is ∼5.6Å, while the distance in the perpendicular axis scales with the number of atomic planes forming the primitive cell, and it is ∼6Å for the 11-family, ∼6.5Å for the 111, ∼8.5Å for the 1111 and ∼12-13Å for the 122 one [8].

The electronic structure of any material determines most of its properties and in our case the FeSC are semimetals. In the language of the semiconductors there is a lower band called the valence band and an upper band called the conduction band. In the semimetals those two bands are horizontally displaced and they exhibit an overlap in energy so that there is a transfer of electrons from the valence band to

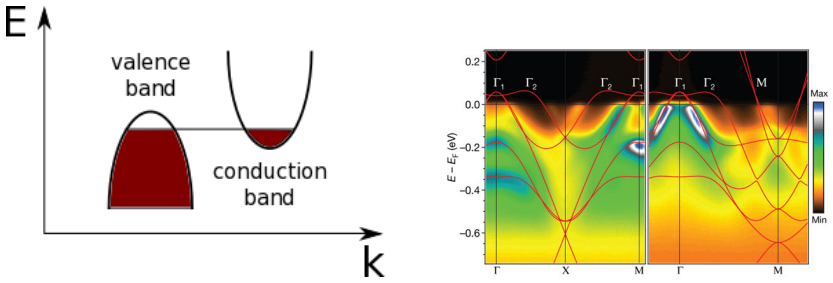

(a) (b)

Figure 1.2: (a) Sketch of semimetalic band-structure illustrating the valence and conduction bands related to the hole and electron pockets. (b) Spectra of LaFePO from ARPES measurements combined with calculated band dispersions through density functional theory (DFT). We can see the two hole pockets that appear around the Γ points and the electron one around the M point (Γ and M points defined in Fig.1.3. Figure (b) taken from [10].

the conduction one until they are at the same level, as shown in Fig.1.2a. This means that in the presence of some external field, there will be current coming from holes in the valence band and current coming from electron transport in the conduction band. Those features of the FeSC become clear from Fermi surface measurements through angle-resolved photoemission spectroscopy (ARPES), where one finds both electron and hole "pockets" [9]. To understand what that means we need to remind ourselves of the concept of the Fermi surface, which is nothing more than a boundary in reciprocal momentum space, where the unit cell of the k-space lattice is the Brillouin Zone (BZ). The shape of the Fermi surface is derived from the occupation (and non-occupation) of the electronic energy bands, according to the symmetries and periodicities of the crystalline lattice. A hole pocket appears when a dispersion band crosses the Fermi level in two subsequent points leaving an empty region above the level, while an electron pocket appears when the subsequent crosses leave a filled region below the Fermi level (Fig.1.2b).

As mentioned above, the atoms of the element X in the tri-layer FeX are positioned above and below the iron plane in a tetrahedral way, so the crystallographic unit cell consists of 2 Fe atoms. However, as shown in Fig.1.3, the primitive cell can be folded and by rotating its axes by a $\pi/4$ rotation we get the 1 Fe unit cell which has half the size of the initial one. The physics is the same, the use of the two different representations is a matter of convention and Fig.1.3 shows the Fermi surface in the 1 Fe/cell and the 2 Fe/cell BZs. The advantage of the unfolded version is that it simplifies the calculations since the energy bands needed to describe the systems are now reduced to half. (Note that the band-structure shown previously in Fig.1.2b is drawn using the 1 Fe/cell representation.)

ARPES measurements combined with first-principle band-structure calculations show that all the various families of FeSC, despite their structural differences, exhibit very similar Fermi surfaces, which in 3D consist of hole cylinders around the $\Gamma = (0, 0)$ point and electron cylinders around the $M = (\pi/\alpha, \pi/\alpha)$ point of the 2 Fe/cell BZ, as illustrated in Fig.1.4a [9, 11, 12]. This form of the Fermi surface makes it clear that there is a two-dimensional character in the electronic structure, and that there is a dominance of the FeX tri-layer introduced above. Thus the 2D cut of the Fermi surface consists of hole and electron "pockets" around the Γ and M points as shown in Fig.1.4b from ARPES. The two-dimensional nature of the FeSC comes out more formally from density functional theory (DFT) calculations, where it becomes clear

that close to the Fermi energy and over a logical range, the states that constitute the electron bands are of predominantly iron character and specifically originate from the 3d valence electrons of the Fe layers. The next closest contribution comes from the electrons of the X element in the tri-layer, which lie within the bandwidth of the 3d Fe electrons.

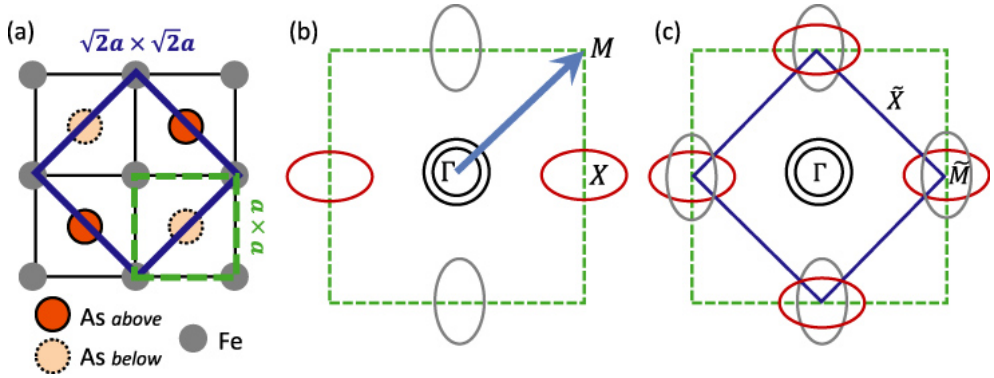

Figure 1.3: (a) Specific case of FeAs tri-layer, the blue line encloses the 2 Fe crystallographic unit cell and the green line the 1 Fe unit cell. (b)-(c) Fermi surface in the 1 and 2 Fe unit cell respectively. The black circles denote hole pockets while the grey and red ellipses are electron pockets. From [11].

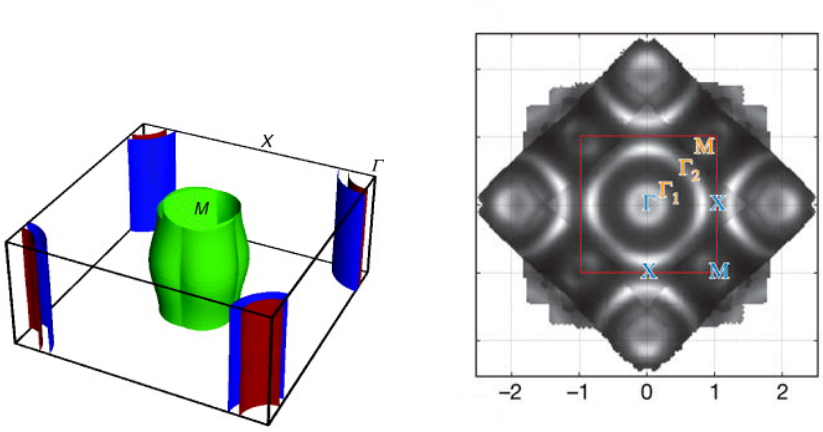

(a) (b)

Figure 1.4: (a) The Fermi surface of LaOFeAs exhibiting hole cylinders around the Γ point and electron cylinder around M. From [13]. (b) Fermi surface measurement in 2D in the 2 Fe/cell BZ through ARPES, illustrating two hole pockets around the Γ point and an electron pocket around M. The axes are in momentum space and the units are π/α, with α being the lattice constant. From [10].

All the above lead to the conclusion that the relevant physics in a low energy range comes solely from the d-orbital valence iron electrons, and so we can approximate the crystal structure with an effective two-dimensional iron plane. Calculations within the context of DFT support that all five d-orbitals of iron have weight around the Fermi level region [14, 15] and so we need to include them in any model we make. Those orbitals are the $xz, yz, x^2 - y^2, xy$ and z^2 and they are schematically shown in Fig.1.5,

where it becomes obvious that in the case where we have C4 rotational symmetry the xz and yz orbitals are degenerate. From DFT calculations it is shown that all those d-orbitals are relevant and this multi-orbital character of the systems we will deal with gives rise to very interesting phenomena, that will be the main focus of this thesis.

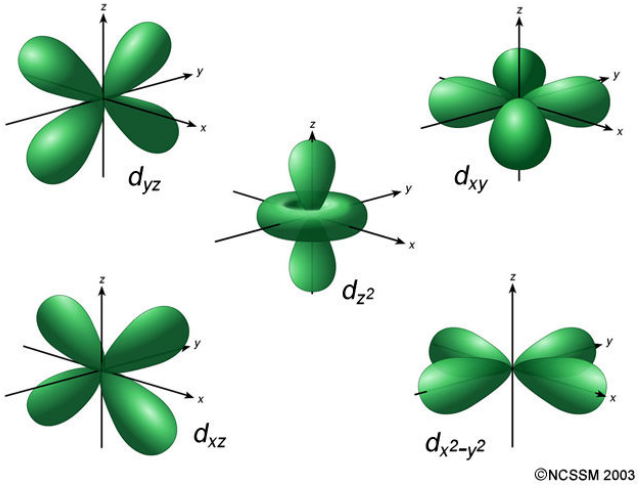

Figure 1.5: Sketch of the 5 Fe d-orbitals $d_{xz}, d_{yz}, d_{x^2-y^2}, d_{xy}, d_{z^2}$.

1.3 Phase diagram and critical temperatures

After the discovery of the first iron-based superconducting compounds, naturally the community got interested in exploring their behavior upon changing different parameters. The variation of the chemical composition by electron and hole doping, combined with temperature variation, gave rise to the very informative FeSC phase diagrams. These exist in different forms depending on the compound in question, but they all follow a similar pattern. In Fig.1.6 we give a general phase diagram plot, including the main phases that can appear in the FeSC. There are three characteristic transition temperatures that (may) appear:

- A structural transition of the lattice from tetragonal to orthorhombic with critical temperature T_S, related to a nematic order (the term will be introduced in this section).
- A magnetic transition with critical temperature T_N.
- A superconducting transition with critical temperature T_S.

The existence of all the transitions mentioned above depends on the particular material. Another major difference among the various compounds is the possible existence of an overlap area between the magnetic and the superconducting region. We will give a small overview of each region that appears in the phase diagram.

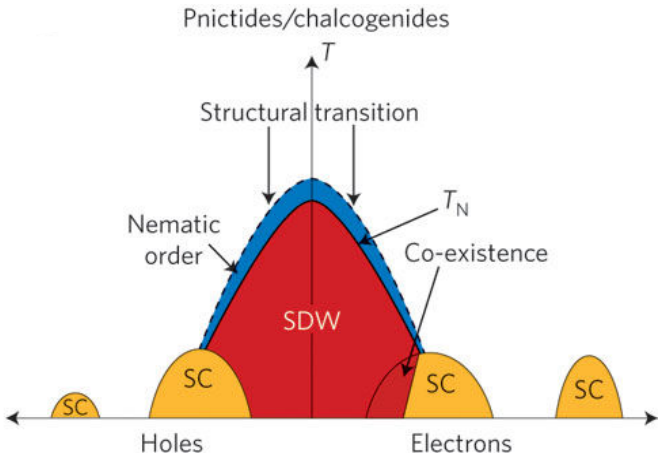

Figure 1.6: General phase diagram of the FeSC. Around zero doping there is a magnetic region (SDW) and superconductivity emerges upon electron or hole doping, with a possible area of co-existence between the two phases. At temperatures higher than the critical one for magnetic ordering, there is also a regime where the system exhibits nematic order. From [16].

Normal state

In their normal state all compounds are paramagnetic, since the iron atoms have magnetic moments with spin projections in random configurations, thus resulting in a zero total magnetization. As we already mentioned earlier in this chapter, the FeSC far from any transitions exhibit concrete band-structures and Fermi surfaces. However, it has been shown experimentally that in many cases they behave as "bad metals", which means that they appear to have large electrical resistivity [17]. This is related to the existence of strong correlation effects, leading to an electron mass renormalization. We will present these experimental findings in detail in chapter 2. The FeSC in most case can be described within a Fermi liquid theory context and, as we will discuss in the following chapters, it can be shown that some of them are actually in proximity to a Mott insulating phase, a state of matter that will be introduced in chapter 2.

Spin density wave state

The main dome in the FeSC phase diagram is the one located near zero doping, and it is related to the magnetic state of the system. We, therefore, call this transition a Neel transition, with critical temperature T_N. The magnetic phase has been studied in detail and the main idea is to relate the state with an ordering vector, arising from the geometry of the Brillouin zone. The usual path is to study the spin susceptibility and figure out the origin of the main contributions to it. It turns out that the dominant contributions come from the so-called *nesting vectors* $\mathcal{Q}$, which are vectors that connect parallel regions in the Fermi surface map [18]. This $\mathcal{Q}$ will then be the ordering vector of the spin density wave (SDW), which is nothing more than the magnetic state of the system. In the typical FeSC Fermi surfaces the dominant nesting vectors are $\mathcal{Q} = (0, \pi)$ and $\mathcal{Q} = (\pi, 0)$, giving rise to a competition between the alignment and the anti-alignment of spins for the lowering of the system's energy. In the absence of a preceding nematic state, the system under the critical temperature T_N spontaneously chooses one of the two ordering vectors and in Fig.1.7 the two possible

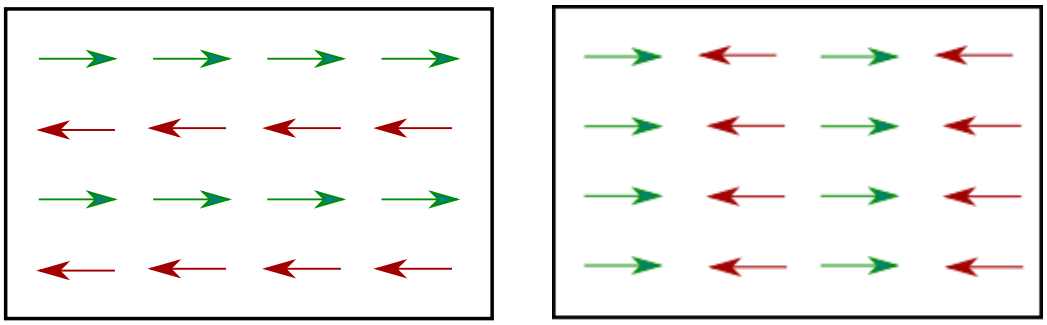

(a) (b)

Figure 1.7: Antiferromagnetic spin configuration on the 2D lattice with ordering vector (a) $\mathcal{Q} = (0, \pi)$ and (b) $\mathcal{Q} = (\pi, 0)$.

antiferromagnetic "stripe" orders are shown. The system, then, exhibits ferromagnetic alignment along one axis of the 2D plane, and anti-ferromagnetic alignment along the perpendicular axis. Moreover, combinations of $\mathcal{Q} = (0, \pi)$ and $\mathcal{Q} = (\pi, 0)$ have been proved to give rise to other, more complicated magnetic states, depending on the specific band-structure and other parameters like the filling of the compound [19]. We are not going to get into the details of those states in this thesis.

Nematic state

In some FeSC compounds, there is a critical temperature above the one of the magnetic transition, which signals the breaking of rotational symmetry and the transition of the system from a tetragonal C4 symmetric to an orthorhombic C2 symmetric state. It is worth noting that the actual structural distortion is relatively small and the anisotropy induced between the x and y axis is of the order of 0.3%. Surprisingly, though, according to experimental findings the energy splitting of d_{xz} and d_{yz} is significantly larger, leading to the conclusion that it is probably the electronic degrees of freedom inducing the structural transition, and not lattice vibrations [20]. In this nematic, as it is named, phase one can find non-zero order parameters related both to charge and spin fluctuations. A divergence of charge fluctuations induces different occupations for the d_{xz} and d_{yz} orbitals, while the one of spin fluctuations leads to a spontaneous symmetry breaking between the $\mathcal{Q} = (0, \pi)$ and $\mathcal{Q} = (\pi, 0)$ ordering vectors, introduced earlier. From symmetry considerations it is known that the appearance of one of these orders will directly induce the other one [21]. This complication makes it really hard to distinguish and state which is actually the driving mechanism for nematicity. The spin fluctuations scenario is the most commonly supported one, due to the proximity of the nematic to the magnetic phase. In the presence of nematicity preceding magnetism, the system has already "chosen" a preferred ordering vector and the spin density wave appears naturally upon temperature lowering. It is clear that the understanding of the nematic state's driving mechanism will be a very good starting point towards the understanding of the spin density wave and the superconducting phases that appear in the phase diagram.

Superconducting state

By increasing the doping in the electron-doped case (and reducing it in the hole-doped one) below some critical temperature T_c the system enters the superconducting phase, which is eventually the most interesting one. The situation now is different than in the

conventional BCS superconductivity, since the phonon mediated pairing mechanism cannot account for the large critical temperatures appearing in the FeSC. There must be another pairing mechanism and the fact that magnetism exists side-to-side with superconductivity points towards the direction of magnetic interactions inducing the electron coupling. In BCS theory the superconducting gap is given by [22]:

$$\Delta(k) = -\sum_{kk'} V_{kk'} \frac{\Delta(k')}{2E_k} \tanh\left(\frac{E_{k'}}{2T}\right) \tag{1.1}$$

with $E_k = \sqrt{\xi_k^2 + |\Delta(k)|^2}$, where ξ_k are the eigenenergies of the system's initial Hamiltonian and $V_{kk'}$ is the interaction parameter. In the case of conventional superconductors $V_{kk'} = V < 0$ and subsequently $\Delta(k) = \Delta_o$, so the gap is isotropic. In the case of unconventional FeSC superconductors, though, if we assume that spin fluctuations induce the coupling then we can allow for a repulsive pairing interaction $V_{kk'} > 0$, as long as the gap changes sign across the points of the Fermi surface. In such a situation $\Delta(k) = -\Delta(k+\mathcal{Q})$ and $\mathcal{Q}$ is a nesting vector of the Fermi surface, a concept we already introduced when talking about the spin density wave phase. The existence of such a nesting vector can cause a divergence in the spin susceptibility leading to the pairing of electrons through this mechanism.

The possible nesting vectors, in combination with the multi-orbital character of the Fermi surface, give rise to multiple possibilities for the structure of the superconducting gap, the most common of which is shown in Fig.1.8b. The simple s-wave form is not met in the case of the FeSC since it implies a constant interaction, while the spin fluctuation mediated mechanism demands a sign change of $V_{kk'}$ along the Fermi surface.

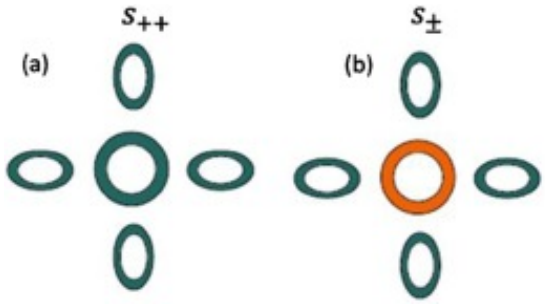

Figure 1.8: Sketch of (a) usual s-wave gap structure, which is related to a constant $V < 0$ and is not met in the FeSC, (b) s_{+-}-wave gap structure, where there is a sign change of the interaction parameter along the Fermi surface and is the most commonly met structure in the FeSC. From [22].

1.4 Thesis outline

This thesis is focused on the study of electronic correlations in the FeSC. In **Chapter 2** we start by giving an overview of the existing theories on the strength of correlations in these materials and the role they play in the electronic properties. We also present a number of relevant experiments highlighting the evidence for relatively strong correlations and for orbital selectivity, a concept we will focus on. Before we proceed with our models and calculations, we introduce some necessary theoretical background related to the Fermi liquid theory and the Mott insulators. Next we move on to **Chapter 3**, where we formulate the slave spin method to deal with strongly correlated fermions and show our results on the exhibited orbital selectivity in the normal and nematic phase. The slave spin method is very powerful but it describes only local interactions, neglecting momentum dependence. Therefore, it is interesting to explore the effect of k-dependence on the electronic correlations and on nematicity. To do so in **Chapter 4** we implement another method, where spin fluctuations play an important role and the calculation of the system's self-energy will provide the information on the degree of correlations. Finally, in **Chapter 5** we give some concluding remarks, together with an outlook on future studies related to the topics covered in this thesis.

Chapter 2

The role of electronic correlations

The physical mechanisms responsible for the properties of the FeSC, have been a field of intense debate and the role of electronic correlations one of the main issues of disagreement in the community. The reason is that there are many conflicting evidences, some pointing towards the direction of weak and others of strong coupling.

The scenario of weak coupling is mainly supported by the success of DFT (density functional theory) calculations to reproduce band-structures and Fermi surfaces of the FeSC systems, which are signs of metallicity and of minor correlations. Moreover, a common belief that the magnetic phase emerges from metallic itinerant carriers has been promoted, due to the existence of nesting vectors on the Fermi surface, which are the same as the antiferromagnetic ordering vectors [15].

On the other hand, the supporters of the strong correlations scenario base their assumption mainly on the fact that strong band renormalization has been observed in relevant experiments. Also, the metallicity in the normal state of some FeSC compounds is actually a bad metallicity, since large electrical resistivity has been measured [23, 24]. In addition to the above, the scenario is related to the fact that there has always been an effort to create a unified theory for iron-based superconductors and cuprates. It is true that their phase diagrams are very similar and that makes it is easy to jump to the conclusion that their electronic properties also behave similarly. The cuprates are strongly correlated materials that become Mott insulators, so it has been proposed that electronic correlations play a major role in the FeSC as well. In this picture, the electrons are mostly localized and the interactions appear in the form of a Heisenberg model [24].

To address the system from one or the other side, different approaches are needed. For weak correlations, the interaction is seen as a small parameter and thus can be treated perturbatively, while for strong correlations the interaction is a significant parameter and the problem is usually addressed through Hubbard physics [25].

However, recent experiments have shown that maybe the truth lies somewhere in between of the two approaches, with the multi-orbital character of the FeSC being a dominant parameter. It has been observed that several compounds, upon tuning some parameters, enter a so-called *orbital selective Mott phase* (OSMP). In this phase, it appears that certain orbitals get very strongly renormalized, thus become "heavier" and act as localized [26]. At the same time, other orbitals remain relatively "light" and so they keep an itinerant behavior. The determining parameters are the relevant energy scales, the kinetic energy (related to the hopping terms and the associated bandwidth), Coulomb repulsion U, Hund's coupling J and temperature T, as well as the total electron filling n. Under a certain tuning of those parameters, the system can enter a *Mott insulating phase*, meaning that the orbitals will get localized and

the compound will act as an insulator [27]. At a different point in the parameters phase space, this can happen only for certain orbitals and not for others. We will give a detailed description of Mott insulators later in this chapter. The OSMP, however, refers to a situation where all the orbitals exhibit an individual band renormalization, different among them, even with none of them actually entering the Mott phase.

In the following section we will give a short overview of various experiments that have been carried out, which provide an insight on the strength of the electron-electron correlations in the iron pnictides as well as the **emergence of the OSMP**. Next, we discuss the specific case of **iron selenide (FeSe)** and its unique properties, by looking at a recent experiment, which has motivated the part of our studies related to the nematic phase. Following that, we introduce the concept of **Mott insulators** and give a small description of those materials. Finally, in the end of this chapter we include a section about the basic concepts of **Fermi liquid theory**. The goal of this chapter is to provide the reader with the necessary experimental and theoretical background, in order to proceed to the specific models and calculations of the following chapters.

2.1 Experiments on the iron pnictides

Various types of experiments have been carried out during the past years on different compounds of FeSC. We are going to show the results obtained from certain of them in order to discuss the role of correlations. However, we are not going to go into the details of the experimental setups and measuring processes. We will rather focus on the information we can gain from them.

Optical conductivity measurements provide a signature of -at least- not weak correlations in compounds of the iron pnictides family [28]. From such experiments we can calculate the quantity $K_{exp} \propto \int d\omega \sigma_{Drude}(\omega)$ (where σ_{Drude} is the measured Drude part of the optical conductivity), which is associated with the kinetic energy related to the coherent part of the spectrum. The ratio of this with the kinetic energy K_{band} of the non-interacting system, K_{exp}/K_{band}, gives a measure of the degree of correlations. As we can see in Fig.2.1a this ratio is a lot smaller than 1, indicating the existence of mediocre or strong correlations in the compound.

Next we look at a **measurement of the specific heat** as a function of temperature and we focus on its slope at low temperatures. This slope is identified with the Sommerfeld coefficient, which is proportional to the quasiparticle density of states at the Fermi energy $\gamma \propto N^*(\epsilon_F)$ [29]. If there is mass enhancement, then the density of states is equally enhanced, according to $N^*(\epsilon_F)/N(\epsilon) = m^*/m$, meaning that the same will hold for the Sommerfeld coefficient. Looking at the inset of Fig. 2.1b, we see that at low temperatures upon hole doping γ is growing, giving an indication for the existence of strong electronic correlations [30].

The experiments we mentioned so far are very indicative in order to estimate the correlations' size. Another feature, however, of the FeSC that we will address now is the orbital selectivity, which we already introduced in the beginning of the chapter. This becomes evident if we look at the quasiparticle mass enhancement as a function of electron filling, where a discrepancy appears between the values calculated within different experimental methods. We give in Fig.2.2 a compact plot, including results from specific heat, optical conductivity, ARPES (angle resolved photo-emission spectroscopy) and quantum oscillations measurements.

Let us, for example, compare the black dots related to the specific heat, with

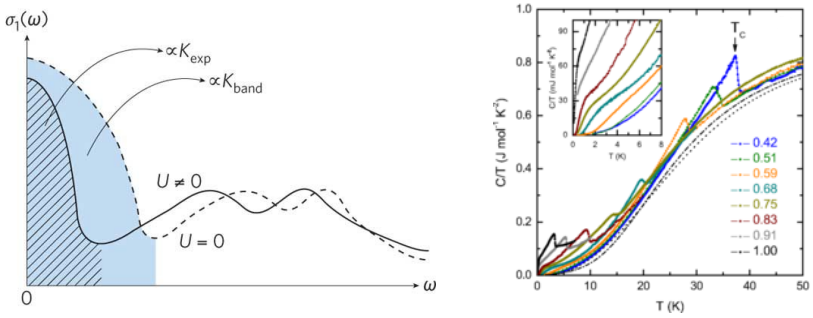

(a) (b)

Figure 2.1: (a) Optical conductivity as a function of frequency. The ratio K_{exp}/K_{band} is related to the strength of electron-electron correlations. From [31]. (b) Temperature dependence of the heat capacity of doped $Ba_{1-x}K_xFe_2As_2$ single crystals. The inset focuses on the low temperature region, where we see how the slope changes with doping [30].

the blue triangles related to optical conductivity in Fig.2.2. We notice that upon increasing the hole doping, the black dots have a strongly increasing tendency, while the blue triangles remain almost constant. The argument behind this bizarre result is that there is *coexistence of electrons with different mass renormalization*, so the behavior of the system is not orbitally uniform. To justify that, we carefully specify the actual measured object of each experiment. In the specific heat case, the measured parameter is the Sommerfeld coefficient, which as we discussed above is proportional to the mass enhancement m^*/m. On the other hand, though, in the case of optical conductivity the relevant parameter is the ratio K_{exp}/K_{band}, where K_{band} is calculated theoretically and is proportional to the inverse of the mass enhancement $(m^*/m)^{-1}$. This means that what we are actually comparing is $\gamma_{exp}/\gamma_{DFT}$ and $(K_{exp}/K_{band})^{-1}$. If the mass renormalization of all the orbitals was the same, then the two ratios would be equal. However, if the different orbitals exhibit different renormalization, then the density of states, which determines $\gamma_{exp}/\gamma_{DFT}$, is proportional to $\sum_k (m^*/m)_k$, while K_{band}, determining K_{exp}/K_{band}, is proportional to $\sum_k (m/m^*)_k$. If we look carefully at the two expressions we will see that $\gamma_{exp}/\gamma_{DFT}$ will be dominated by the largest mass enhancements, so the heaviest quasiparticles and K_{exp}/K_{band} by the lightest ones [32]. Therefore, in Fig.2.2 the black dots will correspond to the strongly renormalized orbitals, while the blue triangles to the weakly renormalized ones, causing a discrepancy and providing evidence for the OSMP.

A similar picture holds for the **ARPES (angular resolved photo-emission spectroscopy) measurements**. In Fig.2.2 there are two different types of such results, the red squares named "ARPES whole" and the red crosses named "ARPES sheets". As we already stated, we are not going to enter into the details of the experimental methods, however we can say that using the ARPES results and comparing with the DFT ones, one can gain information about the individual orbitals as well [33, 34]. In "ARPES whole" the DFT band-structure is renormalized by a global factor to match the experimental results. On the other hand, the "ARPES sheets" points come from a comparison with DFT calculations on the individual Fermi sheets. Thus, the mass enhancement can be different depending on the sheet, and so on the relevant dominating orbital. As we see in the figure, upon electron doping all Fermi sheets exhibit similar mass enhancement, but moving towards the hole-doped side we observe a large differentiation among them. Finally, **quantum oscillations measurements** also illustrate

the effect of orbital selectivity as seen by the yellow crosses in Fig.2.2.

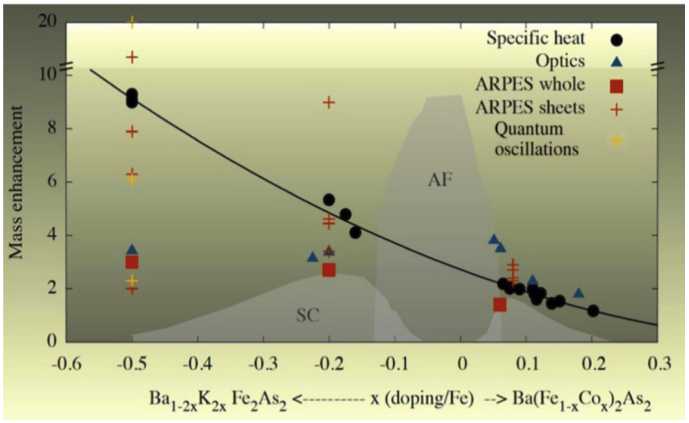

Figure 2.2: Experimental results from specific heat, optical conductivity, ARPES and quantum oscillations measurements in doped $BaFe_2As_2$. The mass enhancement increases with decreasing filling and there is a big discrepancy among the various techniques, attributed to the co-existence of strongly and weakly correlated electrons. In the background there is the experimental phase diagram. From [32].

2.2 The special case of FeSe

Among the various types of FeSC that have been discovered in the past recent years, iron selenide (FeSe) stands out due to its special properties. First of all, we must mention that it is structuraly the simplest FeSC compound, obtained by simple repetition of FeSe tri-layers. One of its most prominent characteristics is the absence of the spin density wave phase [35]. At T$\simeq$ 90K the material undergoes a tetragonal to orthorhombic structural transition and enters a nematic phase. Upon the breaking of rotational symmetry the system exhibits strong electronic anisotropy and so it has been studied a lot in order to gain information about the origins of nematicity. The parent compound, below T$\simeq$ 9K enters the superconducting phase. This is a relatively low temperature, compared to those reached for other FeSC compounds. However, it has been shown that under pressure and by intercalation, the superconducting critical temperature can be significantly enhanced, reaching almost 50K. Moreover, it has been reported that monolayers of FeSe epitaxially grown on $SrTiO_3$ surfaces can lead to a T_c of over 100K [36].

The most commonly accepted explanation for driving the Cooper pairing has been the one of spin fluctuations. This is most easily described by the weak coupling approach of electronic correlations that we introduced earlier in this chapter. This method combined with DFT analysis has managed to give some qualitative results in agreement with experiments, it has failed however to account for the Fermi surface and band-structure of FeSe as measured from ARPES. These experimental results, upon comparison with DFT, reveal that the electronic bands in FeSe get renormalized and the renormalization factor varies among the different orbitals [37, 38].

As discussed earlier, there is evidence for orbital selective physics in FeSC systems, with electrons of one orbital character being weakly correlated, while electrons of other orbital characters strongly correlated. This could then also lead to orbital selective superconductivity, with Cooper pairs being created from electrons of a specific

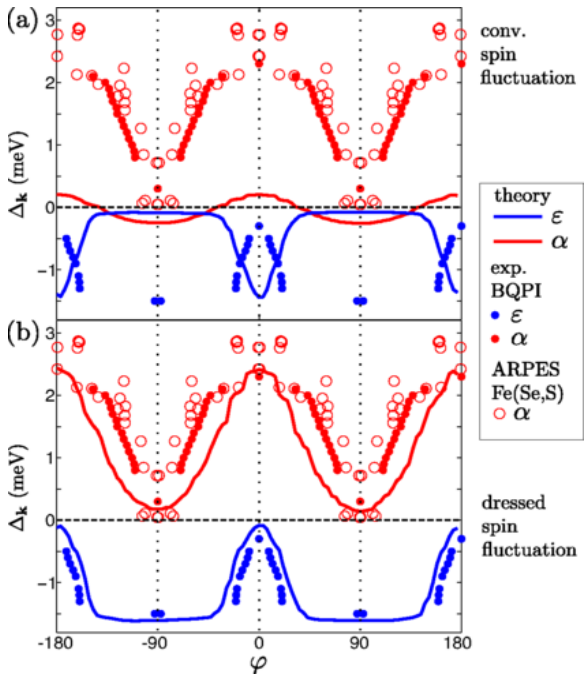

Figure 2.3: (a) FeSe's gap function around the α and ϵ Fermi surface pockets. The dots are experimental data and the solid lines come from conventional spin fluctuation calculations. (b) Same plot, but now the solid lines represent results from spin fluctuation calculations including the orbitally dependent quasiparticle weights. We see the agreement between experiments and theoretical results. From [40].

orbital origin, giving rise to highly anisotropic gap structures. If that is the case, the superconducting gap should be large only for those regions on the Fermi surface where this specific orbital dominates. However, until recently orbital selective Cooper pairing had never been observed experimentally.

A recent study using Bogoliubov quasiparticle interference (BQPI) has provided evidence for strong orbital selectivity effects [39]. The focus of this work was to search for such orbital selective Cooper pairing in FeSe, by imaging impurity-scattered quasiparticles through BQPI. Once again, we will not discuss the details of the experimental measurement but rather focus on the results. In the nematic orthorhombic phase the Fermi surface of FeSe consists of a hole band around $\Gamma = (0, 0)$, named α and an electron band ϵ around $X = (\pi, 0)$. Conventional spin fluctuation calculations support a structure where the gap is weak and almost isotropic on the α-band, while being strong and anisotropic on the ϵ one, but with the anisotropy exhibiting the opposite orientation of the one found experimentally as seen in Fig.2.3(a). In this work though (more details can be found in [39–41]), the orbital selective pairing was included in the calculations and the results shown in Fig.2.3(b), are in very good agreement with the experiments. This constitutes evidence of an orbital selective Cooper pairing mechanism in FeSe. The authors of this study, though, used a rather phenomenological approach, where they chose the quasiparticle weights related to each orbital, by fitting them to the collected data. Then they included those renormalization factors into the spin fluctuation pairing theory and it turned out that the results were surprisingly close to reality. From the calculations, they conclude that the xy orbital is most strongly renormalized, in agreement with experiments. Moreover, it is shown that the xz and yz orbitals, despite their very small energy splitting due to nematicity, exhibit a large

difference in their quasiparticle weights, such that $Z_{yz} \simeq 2Z_{xz}$. Obviously, the challenge now is to give a microscopical explanation of orbital selectivity and obtain the orbitally dependent renormalization through a consistent theoretical approach. We will explore this problem in the following chapters of this thesis.

2.3 Mott insulators

In this section we will introduce the concept of Mott insulators by looking at the simple case of a single band system. From non-interacting band theory we know that when such a system contains a number of electrons equal to the number of sites (so it is at half-filling) it behaves like a metal. That is because it has a partially filled band, so an electronic excitation can happen with zero energy cost.

However, in this picture we assume that electron interactions are weak and we ignore them. If instead the system is strongly correlated, meaning that a single-particle description is insufficient, electronic interactions play a dominant role in its properties. In principle, the delocalization of electrons is favored by the kinetic energy, but when strong correlations come in play the situation becomes more complicated. Now Coulomb repulsion between electrons makes the double occupancy of a state unfavored, so there is a competition between kinetic energy and Coulomb interaction. When the later becomes larger than the former, the energy gets minimized by localization of the electrons in different sites, thus the system becomes insulating. This state is then called Mott insulator after N. Mott who discovered it [42]. It is important to mention that the Mott transition can happen only at half-filling, where there are no more sites for the electrons to move without an energy cost. Away from half-filling the correlations hold a major role in the electronic properties but will never lead to a complete Mott localization.

In order to illustrate the mechanism of the Mott insulators, we give in Fig.2.4 a sketch of the density of states (DOS). At zero interactions the DOS consists of two degenerate bands, whose shape is defined by the hoppings of the Hamiltonian. Usually in a single band case the hopping term is of the form $E_k = -2t(\cos kx + \cos ky)$, by assuming only nearest neighbor interactions. The size of the bands is related to the bandwidth W. By tuning up the interactions the two bands are no longer degenerate and start to split, with the difference between them being equal to the interaction strength [25]. At some critical value U_c a gap appears, separating the two bands and that is the Mott gap. These separated energy bands are the so-called upper and lower Hubbard bands. As it can be more clearly seen in the figure, the Mott gap is equal to the difference between the interaction and the bandwidth $\Delta_{Mott} = U - W$ and the transition happens when it becomes zero $\Delta_{Mott} = U_c - W = 0 \rightarrow U_c = W$. Of course this is not exact, because the size of the Hubbard bands is only approximately equal to W, but it gives a good estimate for the Mott gap.

When the system is multi-orbital the situation becomes complicated because now there are more degrees of freedom. There is the individual on-site energy of each orbital and the various hoppings that one has to take into consideration and that is why in this case an integer filling (rather than only half-filling) can lead to a Mott insulator. A parameter that has a major effect in the multi-orbital systems is Hund's coupling. According to Hund's rule, it is favorable for electrons to have their spins aligned. Thus they start occupying different orbitals and if the number of electrons is larger than the number of orbitals, then they start doubly occupying them. We will not get into the details of the multi-orbital systems but one can find, for example from [43], that

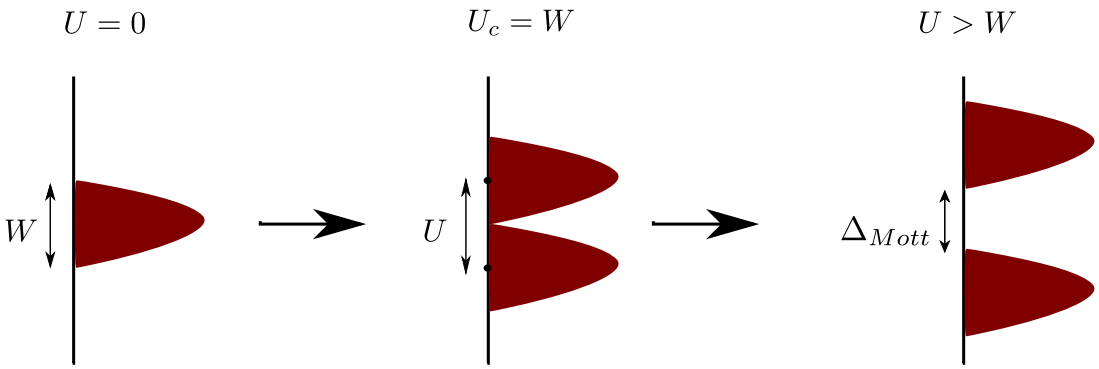

Figure 2.4: Density of states sketch of a metal to Mott insulator transition. The horizontal axis is the DOS and the vertical the energy. At $U = 0$ the system is a metal with two spin degenerate bands. As we increase the interactions the bands are no longer degenerate and after a critical U_c they separate creating between them the Mott gap.

Hund's coupling J modifies the Mott gap equation into $\Delta_{Mott} = U + (N-1)J$ at half-filling and $\Delta_{Mott} = U - 3J$ away from half-filling.

2.4 Fermi liquid theory

In the previous section we discussed Mott insulators and how they can appear by tuning the interactions in strongly correlated metals. Some metals exhibit correlations, but not strong enough to cause carrier localization and these materials are usually described within Fermi liquid theory. It is a phenomenological approach and the main logic behind it is that a gas of interacting fermions is in correspondence with a gas of non-interacting ones [44]. There are though certain conditions: (1) the system must be at low energy and temperature, (b) the system can not be close to any phase transition and (c) there must be "adiabatic continuity". This last condition means that starting from a non-interacting system in an excited state, if we begin increasing the interactions slowly enough for the occupation numbers to stay the same (adiabatically), we will end up in an excited state of the interacting system. The quantum numbers of the interacting system will remain the same as the ones of the non-interacting one.

In a free electron gas the excitations are given by different configurations of the single-particle eigenstates and are related to the creation and annihilation of fermions. In the interacting system, within the context of Fermi liquid theory, the excitations are identified as quasiparticle states, which are not the exact eigenstates of the system. They have a finite lifetime which should be large enough to ensure a well-defined energy but also shorter than any decay processes originating from electron-electron scattering. It can be shown that the inverse lifetime is proportional to the quasiparticle energy (with respect to the Fermi level):

$$\frac{1}{\tau_k} \propto \xi_k^2, \tag{2.1}$$

if $\xi_k < T$. When the temperature exceeds the quasiparticle energy, the typical excitation energy is $k_B T$ (with k_B the Boltzmann constant) and thus we can write:

$$\frac{1}{\tau_k} \propto T^2. \tag{2.2}$$

We see that the closer we get to the Fermi level the larger the lifetime gets, so the Fermi liquid picture is consistent at small energy scales and the same holds for temperature, which must be smaller than the Fermi energy. Indeed this is a fairly good approximation since the typical metal's Fermi energy is a relatively large scale, leaving room for some temperature variation.

According to the above statements, an excitation of the interacting system can be viewed as a free quasiparticle with a finite lifetime. The information about the interactions must then be encoded is some effective parameters. In order to understand this we look at the Green's function:

$$G(k,\omega) = \frac{1}{\omega - \xi_k - \Sigma(k,\omega)}, \tag{2.3}$$

where ω is the frequency, ξ_k the free electron energy (with respect to the Fermi level) and $\Sigma(k,\omega)$ the self-energy, an object that shifts the particle's energy due to interactions with its environment. Often the self-energy is calculated using the random phase approximation (RPA), a method that includes only the most divergent of all possible diagrams. We are interested in the low frequency region and in momenta close to the Fermi momentum k_F. We know that at the Fermi wave number the real part of the particle's energy vanishes, so we first separate the real from the imaginary part of the self-energy and we get $\xi_{k_F} + Re\Sigma(k_F, 0) = 0$. Now we can expand the real part of the denominator of the Green's function in powers of the small $k - k_F$ and ω:

$$G(k,\omega) = \frac{1}{\omega - [\xi_k + Re\Sigma(k,\omega)] - iIm\Sigma(k,\omega)} \simeq$$

$$\simeq \frac{1}{\omega - \omega\partial_\omega Re\Sigma(k,\omega)\big|_{k=k_F}^{\omega=0} - (k-k_F)\partial_k(\xi_k + Re\Sigma(k,\omega))\big|_{k=k_F}^{\omega=0} - iIm\Sigma(k,\omega)} =$$

$$= Z\left[\omega - \tilde{\xi}_k + \frac{i}{2\tilde{\tau}_k(\omega)}\right]^{-1}. \tag{2.4}$$

In the above expression we have defined the quasiparticle weight Z as:

$$Z^{-1} = 1 - \partial_\omega Re\Sigma(k_F,\omega)\big|_{\omega=0}, \tag{2.5}$$

with the effective energy:

$$\tilde{\xi}_k = (k-k_F)Z\partial_k(\xi_k + Re\Sigma(k,0))\big|_{k=k_F}. \tag{2.6}$$

However, usually the effective energy is given by:

$$\tilde{\xi}_k = \frac{1}{m^*}(k-k_F)k_F, \tag{2.7}$$

where m^*/m expresses the effective mass. This quantity encapsulates the effect of electron-electron interactions, which limit the particle's motion thus making it more "heavy". So from the last two expressions we get for the effective mass:

$$\frac{m}{m^*} = Z\left(1 + \frac{m}{k_F}\partial_k Re\Sigma(k,0)\big|_{k=k_F}\right). \tag{2.8}$$

If the self-energy does not depend on momentum, which will be our assumption in Chapter 3, the effective mass is equal to the inverse of the quasiparticle weight:

$$\frac{m^*}{m} = \frac{1}{Z}. \tag{2.9}$$

We still have not said anything about the imaginary part of the self-energy which is defined through:

$$\frac{1}{\tilde{\tau}_k(\omega)} = -2ZIm\Sigma(k,\omega). \tag{2.10}$$

In order for the Fermi liquid picture to hold, the imaginary part should be a small quantity, so that the Green's function and the spectral function exhibit a Lorentzian with a sharp peak related to the quasiparticle. In an interacting system, Z is always less than unity ($0 < Z < 1$), however the spectral function upon integration should be equal to one, which means that there is a residual part of the function arising from excitations which are not related to the Green's function's pole. This is the incoherent part of the spectrum and is usually seen as a background contribution that in some cases can be neglected, but in others becomes important and should always be treated carefully.

Chapter 3

Slave spin method

In the previous chapter we gave an overview of the dominating theories related to the electronic correlations and their role in the behavior of the FeSC. In this chapter we will explore the limit of strong correlations, and the electronic interactions will be a dominant factor, so they cannot be treated as a small parameter. We will assume that the self-energy is local, thus its momentum dependence will be omitted. The system will be described within Fermi liquid theory, with the strong correlations causing electrons to become incoherent. A crucial ingredient in the description will be the multi-orbital character of the FeSC's electronic structure, which is responsible for many interesting properties.

The physics of strongly correlated systems with electron-electron correlations leading to Mott localization, cannot be described in the context of a single-particle picture, excluding the traditional mean-field methods like Hartree-Fock. It has been a common trend when dealing with such systems to make use of the so-called "slave" particle approaches. The *slave boson technique*, for example, has been widely implemented in similar situations [45]. Within this approach, the physical fermion of the system is represented by a pseudo-fermionic variable and a bosonic one (the "slave" particle). An appropriate mean-field approximation is then performed, decoupling those two degrees of freedom, with the pseudofermion describing the itinerant quasiparticle fraction and the boson the localized one. However, in order for the new Hamiltonian to contain the physics of the original one, some constraints need to be fulfilled and this technique brings up the issue of necessitating two constraints and also vastly enlarging the problem's Hilbert space [46]. The technique we choose to treat the system is the *slave spin method* (SS) [47–49], which has two advantages: (1) we only need one constraint to solve the problem, (2) it can be easily applied to multi-orbital models. We will follow the formulation introduced in [46, 47] and address the problem on a local mean-field level.

3.1 Model for slave spin representation

As it is customarily done in the context of correlated electrons, we will describe the system with the Hubbard model:

$$\hat{H} = \sum_{ijmm'\sigma} t_{ij}^{mm'} d_{im\sigma}^{\dagger} d_{jm'\sigma} + \frac{1}{2} \sum_{ijkl} \sum_{mm'nn'} \sum_{\sigma\sigma'} V_{ijkl}^{mm'nn'} d_{im\sigma}^{\dagger} d_{jm'\sigma'}^{\dagger} d_{kn'\sigma'} d_{ln\sigma}. \quad (3.1)$$

where $t_{ij}^{mm'}$ is the hopping integral and $V_{ijkl}^{mm'nn'}$ the interaction parameters. In order to treat the interaction term, we limit our focus to a subset of bands near the Fermi energy.

That is because the ones coming from deep shells are completely filled and the ones of high energy above the Fermi one are completely empty, so none of them contribute to the interactions. A crucial step now is to consider only on-site interactions between the electrons. In the case of the FeSC there are five d-orbitals involved, and the relevant interactions are $V_{iiii}^{mmmm} = U$, $V_{iiii}^{mm'm'm} = U'$, $V_{iiii}^{mmm'm'} = J$ and $V_{iiii}^{mm'mm'} = J'$. Let us give some insight on the physical mechanisms related to each of those interactions.

- The on-site intra-orbital Coulomb repulsion U is present between two electrons on the same orbital, which as imposed by the Pauli exclusion principle must have opposite spin.
- Since we are looking at a multi-orbital system, electrons on different orbitals will also interact and repel each other and now those electrons can have either equal or opposite spin. This inter-orbital repulsion that we call U' must be smaller than U ($U' < U$) since the distance of the electrons has now increased compared to them "sitting" on the same orbital.
- We know from atomic physics that Hund's rule indicates that the spin alignment in different orbitals is favored in a multi-orbital system. That, together with the fact that electrons obey the anti-commutation relation and in principle can interchange orbital positions, give rise to the Hund's coupling parameter J, which lowers the energy of the system for electron spin alignment in different orbitals.
- There is a last possible process which is that two electrons on the same orbital as a pair hop to another orbital (pair-hopping) and they repel each other with an interaction parameter J'.

From now on we will take $J' = J$, which is a condition imposed by the orbital rotational symmetry of the system [50]. We arrive, then, at the final form of the multi-orbital Hubbard model:

$$\hat{H} = \sum_{ijmm'\sigma} t_{ij}^{mm'} d_{im\sigma}^{\dagger} d_{jm'\sigma} + U \sum_{m} n_{m\uparrow} n_{m\downarrow} + U' \sum_{m \neq m'} n_{m\uparrow} n_{m'\downarrow} +$$
$$+(U' - J) \sum_{m<m',\sigma} n_{m\sigma} n_{m'\sigma} - J \sum_{m \neq m'} d_{m\uparrow}^{\dagger} d_{m\downarrow} d_{m'\downarrow}^{\dagger} d_{m'\uparrow} + J \sum_{m \neq m'} d_{m\uparrow}^{\dagger} d_{m\downarrow}^{\dagger} d_{m'\downarrow} d_{m'\uparrow} \quad (3.2)$$

The orbital rotational symmetry existing in the materials we examine, additionally implies $U' = U - 2J$ [50].

We want to describe our strongly correlated system and the appearance of heavy quasiparticles, which renormalize the kinetic energy. In order to do so, we need to apply a suitable mean-field theory and we use, as mentioned above, the slave spin method. The main idea is that we place our problem into an enlarged Hilbert space, containing as many fermionic degrees of freedom as the original, plus for each one of them a spin-1/2 variable. We refer to these quasi-fermions with $f_{i\sigma}$ and to the slave spin with $S_{i\sigma}^{z}$. Note that both carry a spin index and the slave spin component should not be confused with the physical spin, as it is nothing more than an auxiliary variable. Therefore, the states that are contained in this new space are:

$$\begin{aligned} &| \, n_{i\sigma}^{f} = 1, S_{i\sigma}^{z} = +1/2 \rangle \\ &| \, n_{i\sigma}^{f} = 0, S_{i\sigma}^{z} = -1/2 \rangle \\ &| \, n_{i\sigma}^{f} = 0, S_{i\sigma}^{z} = +1/2 \rangle \\ &| \, n_{i\sigma}^{f} = 1, S_{i\sigma}^{z} = -1/2 \rangle \end{aligned} \quad (3.3)$$

We have defined the slave spin so that "up" is related to an occupied electronic state, while "down" to an empty one. This means that the last two states are unphysical since they do not correspond to a state in the original space, while the first two are equivalent to $\mid n^d_{i\sigma} = 1\rangle$ and $\mid n^d_{i\sigma} = 0\rangle$ respectively. In order to exclude the unphysical states we impose the following constraint:

$$f^\dagger_{i\sigma} f_{i\sigma} = S^z_{i\sigma} + \frac{1}{2}. \tag{3.4}$$

It is important here to notice that the electron number operator $n^d_{i\sigma}$ is equivalent to the auxiliary fermions number operator $n^f_{i\sigma}$, and so from the constraint we see that $n^d_{i\sigma}$ can be written in terms of the slave spin z-component as $n^d_{i\sigma} = S^z_{i\sigma} + \frac{1}{2}$. This is going to be very useful in the following sections when we will rewrite the Hamiltonian in the new space.

3.2 One orbital case

As explained in the previous chapters, the FeSC are of multi-orbital character since all the five 3-d iron orbitals should be included in any representation, in order to capture all the physical processes. However, it is a lot more instructive to start by introducing the Hamiltonian for the one orbital case, which simplifies a lot the problem because the orbital degrees of freedom are now absent. Let us take a look at and explore the single-band Hubbard model:

$$\hat{H} = \sum_{ij\sigma} t_{ij} d^\dagger_{i\sigma} d_{j\sigma} + U \sum_i n_{i\uparrow} n_{i\downarrow}, \tag{3.5}$$

where $n_{i\sigma} = d^\dagger_{i\sigma} d_{i\sigma}$. We can re-write the Hamiltonian in its particle-hole symmetric form (see Appendix A for the whole derivation of the following expression):

$$\hat{H}_{int} = \frac{U}{2} \sum_i \Big(\sum_\sigma (n^d_{i\sigma} - \frac{1}{2}) \Big)^2 = \frac{U}{2} \sum_i \Big(\sum_\sigma S^z_{i\sigma} \Big)^2, \tag{3.6}$$

where we took advantage of the expression $n^d_{i\sigma} = S^z_{i\sigma} + \frac{1}{2}$ we wrote in the end of the previous section.

We now need to rewrite the electronic operator of the original Hamiltonian into a composite one that will include a "fermionic" and a "spin" part, each related to the two different degrees of freedom we introduced. When we actually attempt to formulate it, we come across a complication related to the spin part of the operator because there is not a unique choice that would give the correct result upon acting on any of the system's states. To go past this issue we write $d_{i\sigma} \to f_{i\sigma} O_{i\sigma}$ and $=$ and we choose the most general expression for the spin part of the composite operator:

$$O_{i\sigma} = \begin{pmatrix} 0 & c_{i\sigma} \\ 1 & 0 \end{pmatrix} = S^-_{i\sigma} + c_{i\sigma} S^+_{i\sigma}, \tag{3.7}$$

with $c_{i\sigma}$ for now being an arbitrary complex number (for a detailed derivation see Appendix B).

We have now everything we need to write the final form of the Hamiltonian in this formalism and the enlarged Hilbert space:

$$\hat{H} - \mu \hat{N} = \sum_{<ij>\sigma} t_{ij} O^\dagger_{i\sigma} O_{j\sigma} f^\dagger_{i\sigma} f_{j\sigma} + \frac{U}{2} \sum_i \Big(\sum_\sigma S^z_{i\sigma} \Big)^2 - \mu \sum_{i\sigma} n^f_{i\sigma}. \tag{3.8}$$

3.2.1 Mean-field approximation

We have now formulated our model and it is quite obvious that not only we did not solve the problem, but it appears that we have complicated it even more by enlarging the Hilbert space and by creating a hopping term where both pseudo-fermions and spins appear. At this point we make the crucial step and declare that pseudo-fermions and spin degrees of freedom should be decoupled, thus we can perform a mean-field approximation by decoupling the auxiliary fermions and the slave-spin degrees of freedom in the following way:

$$\sum_{<ij>\sigma} t_{ij} O^{\dagger}_{i\sigma} O_{j\sigma} f^{\dagger}_{i\sigma} f_{j\sigma} \simeq \sum_{<ij>\sigma} t_{ij} \langle O^{\dagger}_{i\sigma} O_{j\sigma} \rangle f^{\dagger}_{i\sigma} f_{j\sigma} + \sum_{<ij>\sigma} t_{ij} O^{\dagger}_{i\sigma} O_{j\sigma} \langle f^{\dagger}_{i\sigma} f_{j\sigma} \rangle. \quad (3.9)$$

Now we can write the Hamiltonian as the sum of a "fermionic" and a "spin" one. The thing to notice is that each of those H_f and H_s contains as coefficients expectation values related to the other Hamiltonian, so in that sense they are coupled and depend on each other.

We will then need to treat the constraint on average by introducing a Lagrange multiplier λ that will not be dependent on the site or the spin index, since for now we are dealing with uniform phases. Hence, we include the constraint in the Hamiltonian by adding the equal-to-zero term:

$$\lambda \big(\sum_{i,\sigma} (S^z_{i\sigma} + \frac{1}{2}) - \sum_i n^f_i \big) = 0 \quad (3.10)$$

and it can now be written as the sum of a fermionic and a spin Hamiltonian $H = H_f + H_s$:

$$H_f = \sum_{<ij>,\sigma} t_{ij} (Q_{ij} f^{\dagger}_{i\sigma} f_{j\sigma} + h.c.) - (\mu + \lambda) \sum_i n^f_i,$$

$$H_s = \sum_{<ij>,\sigma} (J_{ij} O^{\dagger}_{i\sigma} O_{j\sigma} + h.c.) + \lambda \sum_{i,\sigma} \big(S^z_{i\sigma} + \frac{1}{2} \big) + \frac{U}{2} \sum_i \big(\sum_{\sigma} S^z_{i\sigma} \big)^2, \quad (3.11)$$

where the hopping renormalization factor is $Q_{ij} = \langle O^{\dagger}_{i\sigma} O_{j\sigma} \rangle_s$, the slave-spin exchange constant $J_{ij} = t_{ij} \langle f^{\dagger}_{i\sigma} f_{j\sigma} \rangle_f$ and from the constraint $\langle n^f_{i\sigma} \rangle_f = \langle S^z_{i\sigma} \rangle_s + \frac{1}{2}$, so those are three coupled self-consistent equations.

The pseudo-fermionic Hamiltonian has a simple form and can be easily treated, the spin one on the other hand is still complicated so it needs further manipulation. At this stage we will make the last approximation and assume that the spin Hamiltonian describes a single site, which "feels" an effective field arising from the average values of the operators on all the other sites. In other words, we need to perform a single-site mean field approximation and assuming translational invariance we decouple the spin operators as:

$$O^{\dagger}_{i\sigma} O_{j\sigma} \simeq \langle O^{\dagger}_{i\sigma} \rangle O_{j\sigma} + O^{\dagger}_{i\sigma} \langle O_{j\sigma} \rangle. \quad (3.12)$$

Now we can write the spin Hamiltonian in the following way:

$$H_s = \sum_i H^i_s = \sum_{i,\sigma} \big(h_{i\sigma} O^{\dagger}_{i\sigma} + h.c. \big) + \lambda \sum_{i,\sigma} \big(S^z_{i\sigma} + \frac{1}{2} \big) + \frac{U}{2} \sum_i \big(\sum_{\sigma} S^z_{i\sigma} \big)^2, \quad (3.13)$$

where

$$h_{i\sigma} = h_\sigma = \sum_j J_{ij} \langle O_{j\sigma} \rangle_s = \langle O_{i\sigma} \rangle_s \sum_j \langle f^\dagger_{i\sigma} f_{j\sigma} \rangle_f = \langle O_{i\sigma} \rangle_s \sum_k \epsilon_k \langle f^\dagger_{k\sigma} f_{k\sigma} \rangle_f = \langle O_{i\sigma} \rangle_s \bar{\epsilon}. \tag{3.14}$$

The kinetic energy per spin for the pseudo-fermions $\bar{\epsilon}$ can be calculated independently through the auxiliary fermion's Hamiltonian. We now relate the renormalization of the kinetic energy with the quasiparticle weight and remembering what we learned from the Fermi liquid theory in chapter 2 we get $Z = \langle O_{i\sigma} \rangle^2$.

A last point we should take a look at is that so far $c_{i\sigma}$ has been a general undefined complex number. In order to make it more specific we can use our knowledge for the quasiparticle weight in the non-interacting limit, which we know should be equal to one $Z(U = 0) = 1$. In the non-interacting limit the spin index is redundant since spin-up and spin-down are indistinguishable and also we can omit the site index. Then the spin Hamiltonian reduces to the simple expression:

$$\begin{gathered} \hat{H}_s = hO^\dagger + h^* O + \lambda S^z = \\ = h \begin{pmatrix} 0 & 1 \\ c^* & 0 \end{pmatrix} + h^* \begin{pmatrix} 0 & c \\ 1 & 0 \end{pmatrix} + \tfrac{\lambda}{2} \begin{pmatrix} 1 & 0 \\ 0 & -1 \end{pmatrix} = \begin{pmatrix} \frac{\lambda}{2} & \alpha \\ \alpha^* & -\frac{\lambda}{2} \end{pmatrix}, \end{gathered} \tag{3.15}$$

where $\alpha = h + ch^*$. If we now diagonalize the Hamiltonian we get that the ground state is given by:

$$\big|GS\big\rangle = \begin{pmatrix} \frac{\lambda/2 - \epsilon_0}{N} \\ -\frac{\alpha^*}{N} \end{pmatrix} \tag{3.16}$$

and the corresponding eigenvalue is: $\epsilon_0 = -\sqrt{\frac{\lambda^2}{4} + |\alpha^2|}$, with $N = \sqrt{-2\epsilon_0\big(\frac{\lambda}{2} - \epsilon_0\big)}$. We now calculate on the ground state the expectation values:

$$\begin{gathered} < S^z >= \tfrac{1}{2} \begin{pmatrix} \frac{\lambda/2 - \epsilon_0}{N} & -\frac{\alpha^*}{N} \end{pmatrix} \begin{pmatrix} 1 & 0 \\ 0 & -1 \end{pmatrix} \begin{pmatrix} \frac{\lambda/2 - \epsilon_0}{N} \\ -\frac{\alpha^*}{N} \end{pmatrix} \Rightarrow \\ < S^z >= -\tfrac{\lambda}{4\epsilon_0} \end{gathered} \tag{3.17}$$

and

$$Z =< O >^2 = \frac{|c\alpha^* + \alpha|^2}{4\epsilon_0^2} = 1. \tag{3.18}$$

Taking into consideration the constraint expression and denoting $n = \sum_\sigma n_\sigma$ the electron density, we get:

$$\begin{gathered} n_\sigma - \tfrac{1}{2} =< S^z >= -\tfrac{\lambda}{4\epsilon_0} \Rightarrow \big(n_\sigma - \tfrac{1}{2}\big)^2 = \tfrac{\lambda^2}{16\epsilon_0^2} \Rightarrow \\ n_\sigma^2 - n_\sigma = -\tfrac{|\alpha|^2}{|c\alpha^* + \alpha|^2} \Rightarrow \tfrac{1}{(c+1)^2} = n_\sigma(1 - n_\sigma), \end{gathered} \tag{3.19}$$

where we have assumed that c is a real number and we end up with the final expression:

$$c_\sigma = \frac{1}{\sqrt{n_\sigma(1 - n_\sigma)}} - 1. \tag{3.20}$$

If we substitute $n_\sigma = 1/2$ in the expression above we can easily see that for the half-filled case the coefficient is $c = 1$. We have dropped the i index, because the spin Hamiltonian can be written as a sum of the independent Hamiltonians for each site, and from now on we will also drop the σ index, since in the cases we are looking at the density n does not depend on it.

3.2.2 Procedure and quasiparticle weight calculation

In the last section we introduced the slave spin mean field approximation and we formulated our model. Coming now to the practical part, in order to obtain the quasiparticle weight for different parameters, that will offer us an insight into the system's behavior towards the Mott transition, the problem can be solved iteratively. This process includes several steps and below we give an explicit description of each of them.

- The first thing we need to do is calculate the **kinetic energy per spin for the pseudo-fermions** so we need to diagonalize the fermionic Hamiltonian.

That can be easily done in this case by Fourier transforming (FT) and assuming only nearest neighbor interactions (NNI):

$$H_f = \sum_{<ij>,\sigma} t_{ij}(Q_{ij} f^\dagger_{i\sigma} f_{j\sigma} + h.c.) - (\mu+\lambda)\sum_i n^f_i \overset{\text{FT}}{\Longrightarrow}$$

$$H_f = \sum_{<ij>,\sigma} t_{ij}\big(Q_{ij}\sum_k e^{ikr_i} f^\dagger_{k\sigma}\sum_{k'} e^{-ik'r_j} f_{k'\sigma} + h.c.\big) - (\mu+\lambda)\sum_i\sum_k e^{ikr_i} f^\dagger_{k\sigma}\sum_{k'} e^{-ik'r_i} f_{k'\sigma} \overset{\text{NNI}}{\Longrightarrow}$$

$$H_f = \sum_{k,\sigma}\big(Z\epsilon_k - (\mu+\lambda)\big) f^\dagger_{k\sigma} f_{k\sigma}, \tag{3.21}$$

where $\epsilon_k = -2t\big(\cos(k_x) + \cos(k_y)\big)$. Now we can easily calculate $\bar{\epsilon}$, considering that $\big\langle f^\dagger_{k\sigma} f_{k\sigma}\big\rangle_f = \epsilon_{fermi} = 1/\big(e^{(Z\epsilon_k - (\mu+\lambda))/kT} + 1\big)$ and so:

$$\bar{\epsilon} = \frac{1}{\mathcal{V}}\sum_k -\frac{2t\big(\cos(k_x)+\cos(k_y)\big)}{e^{(Z\epsilon_k-(\mu+\lambda))/kT}+1}, \tag{3.22}$$

with $\mathcal{V}$ being the normalization factor.

- The next step is to get into the self-consistency process. Following the usual path when dealing with such situations, the starting point is to **guess an initial value for** Z. From 3.14 we then obtain the parameter $h = \sqrt{Z}\bar{\epsilon}$, using the guessed value for Z.
- Our goal, however, is to actually calculate Z, so using the guessed value we will iteratively calculate all the parameters necessary to determine Z and adjust the guessed value to the calculated one, until we reach convergence. To do all that we must first **write the spin Hamiltonian in matrix form and diagonalize it**.

The basis we will use is:

$$\begin{pmatrix} \uparrow\uparrow \\ \uparrow\downarrow \\ \downarrow\uparrow \\ \downarrow\downarrow \end{pmatrix}, \tag{3.23}$$

where in every element the first arrow corresponds to the state with real spin up and the second to the one with spin down. The arrow is related to the slave spin, so to the existence of an electron in each state. For example the second element of the basis $|\uparrow\downarrow>$ reads "spin up occupied - spin down not occupied" and the third element $|\downarrow\uparrow>$ "spin up not occupied - spin down occupied". We need to write all the operators that appear in eq.3.13 in the enlarged space and we use the tensor product relation (we write it in the simple case of 2x2 matrices, but it is generalized to n-dimensions):

$$A = B \otimes C = \begin{pmatrix} B_{11}C & B_{12}C \\ B_{21}C & B_{22}C \end{pmatrix}. \tag{3.24}$$

Applying it to our operators we get:

$$S^z_\uparrow \otimes I_\downarrow = \frac{1}{2}\begin{pmatrix} 1 & 0 & 0 & 0 \\ 0 & 1 & 0 & 0 \\ 0 & 0 & -1 & 0 \\ 0 & 0 & 0 & -1 \end{pmatrix}, \quad I_\uparrow \otimes S^z_\downarrow = \frac{1}{2}\begin{pmatrix} 1 & 0 & 0 & 0 \\ 0 & -1 & 0 & 0 \\ 0 & 0 & 1 & 0 \\ 0 & 0 & 0 & -1 \end{pmatrix}, \tag{3.25}$$

$$O_\uparrow \otimes I_\downarrow = \begin{pmatrix} 0 & 0 & c & 0 \\ 0 & 0 & 0 & c \\ 1 & 0 & 0 & 0 \\ 0 & 1 & 0 & 0 \end{pmatrix}, \quad I_\uparrow \otimes O_\downarrow = \begin{pmatrix} 0 & c & 0 & 0 \\ 1 & 0 & 0 & 0 \\ 0 & 0 & 0 & c \\ 0 & 0 & 1 & 0 \end{pmatrix}, \tag{3.26}$$

$$O^\dagger_\uparrow \otimes I_\downarrow = \begin{pmatrix} 0 & 0 & 1 & 0 \\ 0 & 0 & 0 & 1 \\ c & 0 & 0 & 0 \\ 0 & c & 0 & 0 \end{pmatrix}, \quad I_\uparrow \otimes O^\dagger_\downarrow = \begin{pmatrix} 0 & 1 & 0 & 0 \\ c & 0 & 0 & 0 \\ 0 & 0 & 0 & 1 \\ 0 & 0 & c & 0 \end{pmatrix}, \tag{3.27}$$

$$\Big(\sum_\sigma S^z_{i\sigma}\Big)^2 = \begin{pmatrix} 1 & 0 & 0 & 0 \\ 0 & 0 & 0 & 0 \\ 0 & 0 & 0 & 0 \\ 0 & 0 & 0 & 1 \end{pmatrix}. \tag{3.28}$$

Combining all these we can write H_s as the following matrix:

$$H_s = \begin{pmatrix} \lambda + \frac{U}{2} & h(c+1) & h(c+1) & 0 \\ h(c+1) & 0 & 0 & h(c+1) \\ h(c+1) & 0 & 0 & h(c+1) \\ 0 & h(c+1) & h(c+1) & -\lambda + \frac{U}{2} \end{pmatrix}. \tag{3.29}$$

Now we can numerically diagonalize H_s.

- Next we calculate the expectation value of O_σ and from that $Z = \langle O_\sigma \rangle^2$, as well as the expectation value of S^z in order to fulfill the constraint on average in each circle of the process. We **repeat the procedure iteratively until** Z **converges**.

- A last point we should be careful with is that during the process of calculating Z we do not end up with the wrong electron density/chemical potential. When we examine the case of half-filling, so for $n = 1 \to n_\sigma = \frac{1}{2}$, according to the way

we wrote the Hamiltonian, the chemical potential is zero and from that in order to obtain particle-hole symmetry we also need to have zero Lagrange multipliers, so $\mu = \lambda = 0$. However, when we explore cases away from half-filling, if we are not careful we will end up with a converged quasiparticle weight Z that will be wrong, because the self-consistency circles of computation have moved the electron density away from the desired value. In order to deal with this problem **we need within every cycle of our iteration to adjust λ, as well as μ** in a way that the constraint of Eq.(3.4) is satisfied and the density is the one we want. Then we can recalculate c, n and Z accordingly until the correct converged value for the quasiparticle weight is obtained.

3.2.3 Results for the one orbital case

As we already mentioned in the previous section the energy dispersion in this one band case is $\epsilon_k = -2t\big(\cos(k_x)+\cos(k_y)\big)$ and for half-filling we get $\mu = 0$. The corresponding band-structure along a certain path and the Fermi surface are given in Fig.3.1 and we see that the bandwidth is $W = 8eV$.

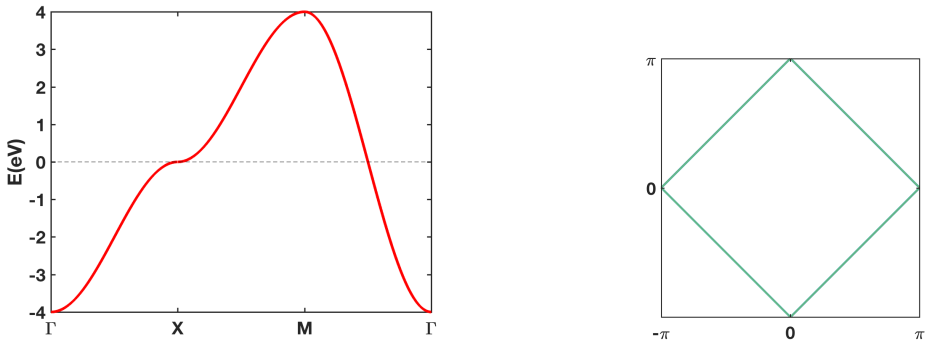

(a) (b)

Figure 3.1: (a) Band-structure of the single-band case along the path $\Gamma XM\Gamma$ with $\Gamma = (0,0), X = (\pi,0), M = (\pi,\pi)$. (b) Fermi surface of the single-band case, where the C4 symmetry of the system is evident.

From now on and throughout this chapter we will be using a momentum grid of size 100x100 and, until mentioned otherwise, the temperature will be $kT = 1meV$, which is a low enough energy scale. Following the procedure described in section 3.2.2 for the case of half-filling $n = 1 \rightarrow n_\sigma = \frac{1}{2}$, we get that the quasiparticle weight decreases with increasing interaction strength. That is what we expected since tuning up the Coulomb repulsion makes the electrons gradually "freeze" in their positions and localization gets favored over itineracy. That is related to the appearance of heavy quasi-particles with increased effective mass and correspondingly decreased weight. As we keep tuning up the interaction strength, the Z-factor eventually drops to zero for the critical value $U_c \simeq 13.2eV$, as shown in Fig. 3.2. That is then the critical interaction for the transition to the Mott insulator phase.

At this point, it is important to mention that this result is in very good agreement with dynamical mean-field theory (DMFT) [46], as well as slave-boson techniques and results using the Gutzwiller approximation [45]. Therefore, we are confident that the slave spin method is indeed an appropriate one for the case of strongly correlated FeSC, in order to follow their transition into a Mott insulating phase.

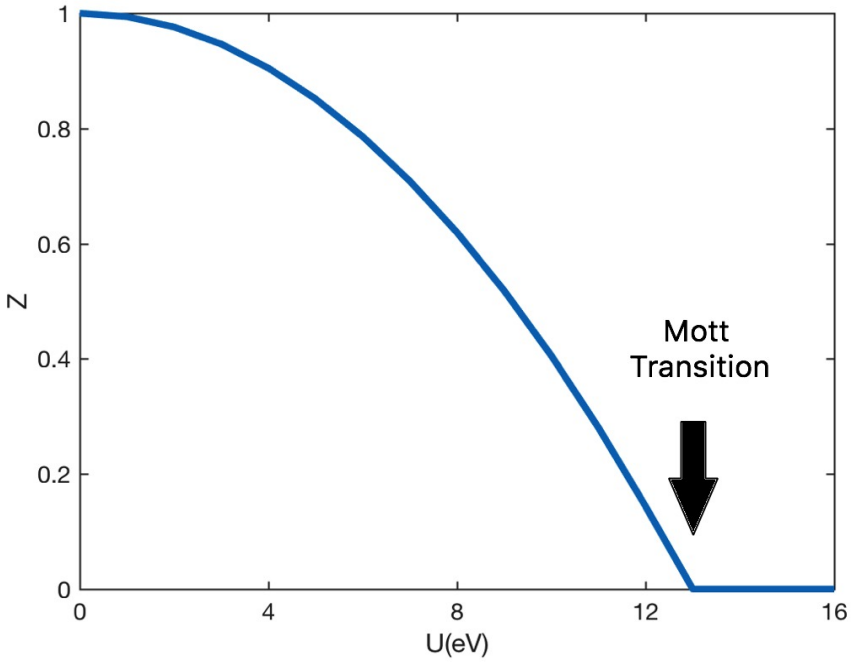

Figure 3.2: Single orbital case at half-filling. The quasiparticle weight drops with increasing interaction strength, until it reaches zero and enters the Mott insulating phase at $U_c \simeq 13.2eV$.

We are interested now in exploring the behavior of the system away from half-filling. If we move the chemical potential away from $\mu = 0$, we will subsequently also move the density away from $n = 1$, always keeping in mind that we should adjust accordingly the Lagrange multiplier λ (which will now be non-zero), in order to get the correct filling and keep the constraint fulfilled. By reducing slightly the filling, we see in Fig.3.3 that the quasiparticle weight still drops with increasing interaction strength, but Z does not vanish at any point. After a critical interaction it saturates at a small value, meaning that the system has large effective mass but not a divergent one, so there is not complete Mott localization. If we start moving even further from half-filling, we observe from Fig.3.3 a reduction in the Z factor suppression, which now drops until a point and then saturates at a mediocre value. Finally, if we take the density to very low values, we see that the quasiparticle weight is almost unaffected by the interactions and stays very close to the $Z = 1$ value of the non-interacting metallic electron gas. Concluding from all the above, we can understand that in order to get into the Mott insulating phase (so obtain $Z = 0$), an integer number of electrons per site is necessary and as we go further away from the half-filled case, the effect of localization becomes less and less evident.

Once again, a comparison with the results obtained through the slave boson technique [45] leads to very good agreement between the two methods. This is one more piece of evidence supporting the adequacy of the slave spin method in the description of strongly correlated systems.

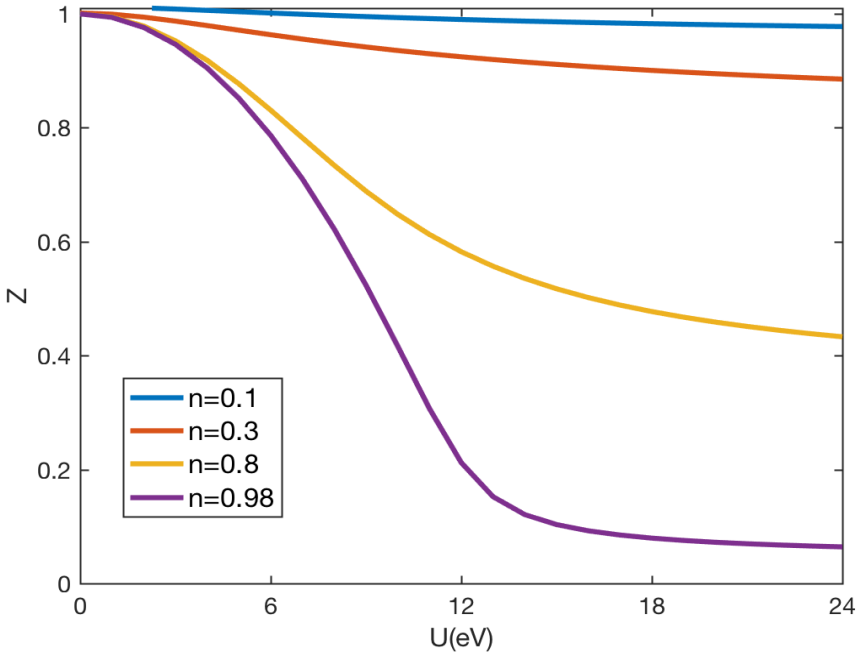

Figure 3.3: Single orbital case away from half-filling. The system never enters the Mott insulating phase and as we move further away from half-filling, the quasiparticle weight tends to saturate at higher values. This is in agreement with the statement we made in chapter 2, that Mott localization necessitates an integer number of electrons.

3.3 Multi-orbital case

In the previous section we derived the slave spin formalism for the simplified single orbital case. We know, however, that this is far from reality since the multi-orbital character of the FeSC not only is present, but there are many indications pointing out that it is the determining factor in any attempt to explain their unconventional behavior. In this section we will explore the model for the multi-orbital case and, on the practical front, use explicit band representations that are relevant for the FeSC. We will particularly try to understand and explain the role of Hund's coupling and how it dominates in these materials, giving rise to orbital selectivity. Therefore, we start by formulating the Hamiltonian in the slave spin context and then we move on to specific cases, leading finally to the five orbital model which we know is the appropriate one. At the end, we will approach the nematic state and explore its interesting features, motivated by the experiment on FeSe introduced in chapter 2.

3.3.1 Mean-field approximation

Let us (at least for now) ignore the two last terms of equation 3.2, the spin-flip and pair-hopping, and focus on the remaining multi-orbital Hamiltonian. This approximation has been shown to bring no qualitative changes in the results [46]. Thinking in the same way as in the single band case and keeping in mind that now all terms will carry

orbital indices (m, m'), we end up with the mean-field equations:

$$H_f = \sum_{i\neq j, mm'\sigma} t_{ij}^{mm'} \sqrt{Z_m Z_{m'}} f_{im\sigma}^\dagger f_{jm'\sigma} + \sum_{im\sigma} (\epsilon_m - \lambda_m - \mu) n_{im\sigma}^f, \tag{3.30}$$

$$H_s = \sum_{m,\sigma} \left[(h_m O_{m\sigma}^\dagger + h.c.) + \lambda_m (S_{m\sigma}^z + \frac{1}{2}) \right] + \hat{H}_{int}[S], \tag{3.31}$$

$$\hat{H}_{int}[S] = U \sum_m S_{m\uparrow}^z S_{m\downarrow}^z + U' \sum_{m\neq m'} S_{m\uparrow}^z S_{m'\downarrow}^z + (U' - J) \sum_{m<m',\sigma} S_{m\sigma}^z S_{m'\sigma}^z, \tag{3.32}$$

$$h_{m\sigma} = \sum_{m'} \left\langle O_{m'\sigma} \right\rangle_s \sum_{j(\neq i)} t_{ij}^{mm'} \left\langle f_{im\sigma}^\dagger f_{jm'\sigma} \right\rangle_f, \tag{3.33}$$

$$Z_m = |\left\langle O_{m\sigma} \right\rangle|^2. \tag{3.34}$$

Note that in the expression for the fermionic Hamiltonian, we have explicitly written down the on-site energy term (related to the crystal field splitting). The reason is that the Z-factor renormalization should apply on the kinetic energy only, hence this term should be separated. The constraint as well as the gauge number will both now be orbitally dependent:

$$\begin{aligned} \left\langle n_{im\sigma}^f \right\rangle_f &= \left\langle S_{im\sigma}^z \right\rangle_s + \tfrac{1}{2} \\ c_{im\sigma} = c_m &= \frac{1}{\sqrt{\left\langle n_{im\sigma}^f \right\rangle (1 - \left\langle n_{im\sigma}^f \right\rangle)}} - 1 \end{aligned} \tag{3.35}$$

It is obvious that at the specific case of a two band model, the indices can take two values $m, m' = 1, 2$ and they correspond to the xz and yz orbitals, that as we know from the bibliography, are the most relevant ones. So now we will have to calculate two quasiparticle weight factors, Z_1 and Z_2. Similarly if we include five orbitals in our analysis, the indices will take five values $m, m' = 1, 2, 3, 4, 5$ corresponding to the $xz, yz, x^2 - y^2, xy, z^2$ orbitals, and naturally there will be five quasiparticle weight factors Z_1, Z_2, Z_3, Z_4 and Z_5 to be calculated.

3.3.2 Two orbital case - Procedure and quasiparticle weight calculation

We start the exploration of the multi-orbital model by the simplest case, the two orbitals, which is still a simplification, but is more realistic than the single orbital one. Again we are thinking in a way analogous to the one band case, but now we have to be careful because performing a Fourier transform, assuming only nearest neighbor interactions, is not enough to diagonalize the fermionic Hamiltonian H_f. We arrive at:

$$\begin{aligned} H_f = \textstyle\sum_{k\sigma} \big(& Z_1 \epsilon_1(k) n_{k1\sigma}^f + Z_2 \epsilon_2(k) n_{k2\sigma}^f + \sqrt{Z_1 Z_2} \epsilon_{12}(k) (f_{k1\sigma}^\dagger f_{k2\sigma} + f_{k2\sigma}^\dagger f_{k1\sigma}) + \\ & + (E_1 - \lambda_1 - \mu) n_{k1\sigma}^f + (E_2 - \lambda_2 - \mu) n_{k2\sigma}^f \big). \end{aligned} \tag{3.36}$$

We choose to use the dispersion relations as derived within the Raghu model [51], which includes nearest and next nearest neighbor hopping with the two orbitals being the xz and yz. The advantage of this model is that, even though it oversimplifies the

picture and ignores the effect of the other orbitals, it reproduces with good agreement the Fermi surfaces obtained from band-structure DFT calculations:

$$\epsilon_1(k) = -2t_1\cos(k_x) - 2t_2\cos(k_y) - 4t_3\cos(k_x)\cos(k_y), \tag{3.37}$$
$$\epsilon_2(k) = -2t_2\cos(k_x) - 2t_1\cos(k_y) - 4t_3\cos(k_x)\cos(k_y), \tag{3.38}$$
$$\epsilon_{12}(k) = -4t_4\sin(k_x)\sin(k_y), \tag{3.39}$$

where t_1 is the nearest neighbor hopping between orbitals lying on the same axis, t_2 the nearest neighbor hopping between orbitals lying on parallel axis, t_3 the next nearest neighbor hopping between similar orbitals and t_4 the next nearest neighbor hopping between different orbitals, with the values $t_1 = -1, t_2 = 1.3, t_3 = t_4 = -0.85$. The different hopping parameters are shown in a sketchy way in Fig.3.4(c), and the band-structure and Fermi surface of the model in Fig.3.4(a)-(b).

We know, from symmetry considerations, that there is no crystal field splitting between the xz and yz orbitals in the normal state and they are degenerate in energy, so the on-site energy term is a constant diagonal term in the Hamiltonian, that can be shifted according to our choice. From now on we will take the on-site energies $E_1, E_2 = 0$ for simplicity. We have to calculate the coefficients h and they will be given by:

$$h_{1\sigma} = \sqrt{Z_1}\xi_1 + \sqrt{Z_2}\xi_{12}, \tag{3.40}$$
$$h_{2\sigma} = \sqrt{Z_1}\xi_{21} + \sqrt{Z_2}\xi_2, \tag{3.41}$$

where

$$\xi_1 = \textstyle\sum_k \epsilon_1(k)\langle f^\dagger_{k1\sigma} f_{k1\sigma}\rangle_f, \xi_2 = \sum_k \epsilon_2(k)\langle f^\dagger_{k2\sigma} f_{k2\sigma}\rangle_f,$$
$$\xi_{12} = \textstyle\sum_k \epsilon_{12}(k)\langle f^\dagger_{k1\sigma} f_{k2\sigma}\rangle_f = \sum_k \epsilon_{12}(k)\langle f^\dagger_{k2\sigma} f_{k1\sigma}\rangle_f = \xi_{21} \tag{3.42}$$

and we can calculate them after diagonalizing H_f.

As we did for the one band case, we will solve the problem self-consistently, so we need to write down the spin Hamiltonian in matrix form and diagonalize it. Of course now the inclusion of two orbitals in the representation makes the Hilbert space significantly larger, but still it is easy to deal with it on an analytic level. The basis we will use is given in equation 3.43, where in every element the first pair is related to the first orbital xz and the second pair to the second orbital yz. Again, the first arrow of each pair corresponds to the state with real spin up and the second to the one with spin down. We give again an example to lift any doubts concerning the physical meaning of the representation, so let us focus, as an example, on the element $|\downarrow\uparrow, \uparrow\uparrow\rangle$. This reads "first orbital (xz): spin up not occupied - spin down occupied & second orbital (yz): spin up occupied - spin down occupied".

$$\begin{pmatrix} |\uparrow\uparrow,\uparrow\uparrow\rangle \\ |\uparrow\uparrow,\uparrow\downarrow\rangle \\ |\uparrow\uparrow,\downarrow\uparrow\rangle \\ |\uparrow\uparrow,\downarrow\downarrow\rangle \\ |\uparrow\downarrow,\uparrow\uparrow\rangle \\ |\uparrow\downarrow,\uparrow\downarrow\rangle \\ |\uparrow\downarrow,\downarrow\uparrow\rangle \\ |\uparrow\downarrow,\downarrow\downarrow\rangle \\ |\downarrow\uparrow,\uparrow\uparrow\rangle \\ |\downarrow\uparrow,\uparrow\downarrow\rangle \\ |\downarrow\uparrow,\downarrow\uparrow\rangle \\ |\downarrow\uparrow,\downarrow\downarrow\rangle \\ |\downarrow\downarrow,\uparrow\uparrow\rangle \\ |\downarrow\downarrow,\uparrow\downarrow\rangle \\ |\downarrow\downarrow,\downarrow\uparrow\rangle \\ |\downarrow\downarrow,\downarrow\downarrow\rangle \end{pmatrix} \tag{3.43}$$

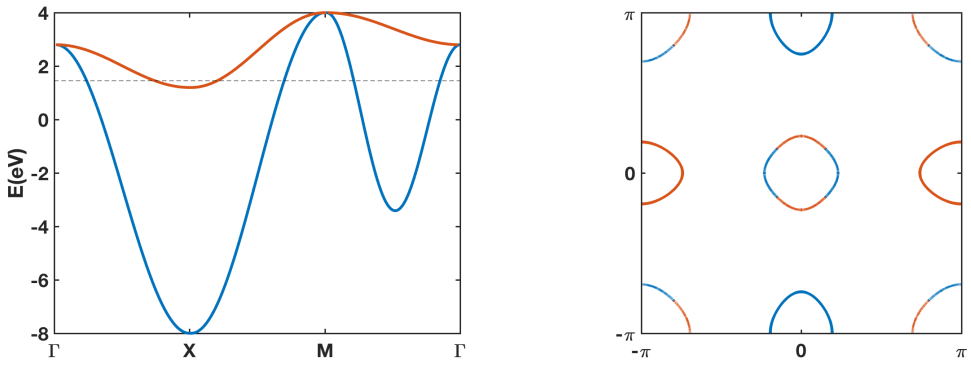

(a) (b)

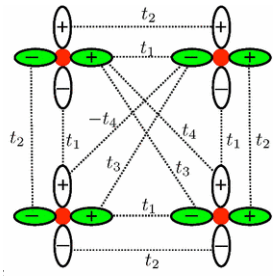

(c)

Figure 3.4: (a) Band-structure of the Raghu model, with the chemical potential $\mu = 1.45$ specified by the dashed line. We see that the bandwidth is $W = 12eV$. (b) Fermi surface at $\mu = 1.45$, where we can see the C4 symmetry of the system. Blue color corresponds to the d_{xz} and red to d_{yz}, so at each point the color indicates the relevant dominant orbital. (c) Sketch of the hopping parameters in the two orbital Raghu model including only d_{xz}, d_{yz}. With green color is denoted the projection of the xz orbital on the xy plane and with white the one of yz. All the hoppings contained in the model are illustrated with arrows on the plane. The plot in (c) is taken from [51].

Following the method we used in the one band case, we write all the operators that appear in H_s in the enlarged space of the two orbitals, so that they are all 16x16 matrices. We will indicatively write down one of the terms and the rest is calculated in the same way:

$$\sum_{m,\sigma} h_m O_{m\sigma} = (h_1 O_{1\uparrow} \otimes I_{1\downarrow}) \otimes I_2 + I_1 \otimes (h_2 O_{2\uparrow} \otimes I_{2\downarrow}) + (I_{1\uparrow} \otimes h_1 O_{1\downarrow}) \otimes I_2 + I_1 \otimes (I_{2\uparrow} \otimes h_2 O_{2\downarrow}) =$$

$$\begin{pmatrix}
0 & h_2c_2 & h_2c_2 & 0 & h_1c_1 & 0 & 0 & 0 & h_1c_1 & 0 & 0 & 0 & 0 & 0 & 0 & 0 \\
h_2 & 0 & 0 & h_2c_2 & 0 & h_1c_1 & 0 & 0 & 0 & h_1c_1 & 0 & 0 & 0 & 0 & 0 & 0 \\
h_2 & 0 & 0 & h_2c_2 & 0 & 0 & h_1c_1 & 0 & 0 & 0 & h_1c_1 & 0 & 0 & 0 & 0 & 0 \\
0 & h_2 & h_2 & 0 & 0 & 0 & 0 & h_1c_1 & 0 & 0 & 0 & h_1c_1 & 0 & 0 & 0 & 0 \\
h_1 & 0 & 0 & 0 & 0 & h_2c_2 & h_2c_2 & 0 & 0 & 0 & 0 & 0 & h_1c_1 & 0 & 0 & 0 \\
0 & h_1 & 0 & 0 & h_2 & 0 & 0 & h_2c_2 & 0 & 0 & 0 & 0 & 0 & h_1c_1 & 0 & 0 \\
0 & 0 & h_1 & 0 & h_2 & 0 & 0 & h_2c_2 & 0 & 0 & 0 & 0 & 0 & 0 & h_1c_1 & 0 \\
0 & 0 & 0 & h_1 & 0 & h_2 & h_2 & 0 & 0 & 0 & 0 & 0 & 0 & 0 & 0 & h_1c_1 \\
h_1 & 0 & 0 & 0 & 0 & 0 & 0 & 0 & 0 & h_2c_2 & h_2c_2 & 0 & h_1c_1 & 0 & 0 & 0 \\
0 & h_1 & 0 & 0 & 0 & 0 & 0 & 0 & h_2 & 0 & 0 & h_2c_2 & 0 & h_1c_1 & 0 & 0 \\
0 & 0 & h_1 & 0 & 0 & 0 & 0 & 0 & h_2 & 0 & 0 & h_2c_2 & 0 & 0 & h_1c_1 & 0 \\
0 & 0 & 0 & h_1 & 0 & 0 & 0 & 0 & 0 & h_2 & h_2 & 0 & 0 & 0 & 0 & h_1c_1 \\
0 & 0 & 0 & 0 & h_1 & 0 & 0 & 0 & h_1 & 0 & 0 & 0 & 0 & h_2c_2 & h_2c_2 & 0 \\
0 & 0 & 0 & 0 & 0 & h_1 & 0 & 0 & 0 & h_1 & 0 & 0 & h_2 & 0 & 0 & h_2c_2 \\
0 & 0 & 0 & 0 & 0 & 0 & h_1 & 0 & 0 & 0 & h_1 & 0 & h_2 & 0 & 0 & h_2c_2 \\
0 & 0 & 0 & 0 & 0 & 0 & 0 & h_1 & 0 & 0 & 0 & h_1 & 0 & h_2 & h_2 & 0
\end{pmatrix},$$

where the $I_{1,2\uparrow,\downarrow}$ are 2x2 identity matrices corresponding to the up or down-spin state of orbital 1 or 2. The $I_{1,2}$ are 4x4 identity matrices, corresponding to orbital 1 and 2 respectively. So looking at the example $(h_1 O_{1\uparrow} \otimes I_{1\downarrow}) \otimes I_2$, we see that the term in the parenthesis is acting on the first orbital and the other term on the second orbital. Inside the parenthesis, the first term acts on the up-spin and the second term on the down-spin. Similarly to the above, we can obtain all the operators appearing in H_s to finally end up with:

$$H_s = \begin{pmatrix}
D_1 & h_2(c_2+1) & h_2(c_2+1) & 0 & h_1(c_1+1) & 0 & 0 & 0 \\
h_2(c_2+1) & D_2 & 0 & h_2(c_2+1) & 0 & h_1(c_1+1) & 0 & 0 \\
h_2(c_2+1) & 0 & D_3 & h_2(c_2+1) & 0 & 0 & h_1(c_1+1) & 0 \\
0 & h_2(c_2+1) & h_2(c_2+1) & D_4 & 0 & 0 & 0 & h_1(c_1+1) \\
h_1(c_1+1) & 0 & 0 & 0 & D_5 & h_2(c_2+1) & h_2(c_2+1) & 0 \\
0 & h_1(c_1+1) & 0 & 0 & h_2(c_2+1) & D_6 & 0 & h_2(c_2+1) \\
0 & 0 & h_{1(c_1+1)} & 0 & h_2(c_2+1) & 0 & D_7 & h_2(c_2+1) \\
0 & 0 & 0 & h_1(c_1+1) & 0 & h_2(c_2+1) & h_2(c_2+1) & D_8 \\
h_1(c_1+1) & 0 & 0 & 0 & 0 & 0 & 0 & 0 \\
0 & h_1(c_1+1) & 0 & 0 & 0 & 0 & 0 & 0 \\
0 & 0 & h_1(c_1+1) & 0 & 0 & 0 & 0 & 0 \\
0 & 0 & 0 & h_1(c_1+1) & 0 & 0 & 0 & 0 \\
0 & 0 & 0 & 0 & h_1(c_1+1) & 0 & 0 & 0 \\
0 & 0 & 0 & 0 & 0 & h_1(c_1+1) & 0 & 0 \\
0 & 0 & 0 & 0 & 0 & 0 & h_1(c_1+1) & 0 \\
0 & 0 & 0 & 0 & 0 & 0 & 0 & h_1(c_1+1)
\end{pmatrix}$$

$$\begin{pmatrix}
h_1(c_1+1) & 0 & 0 & 0 & 0 & 0 & 0 & 0 \\
0 & h_1(c_1+1) & 0 & 0 & 0 & 0 & 0 & 0 \\
0 & 0 & h_1(c_1+1) & 0 & 0 & 0 & 0 & 0 \\
0 & 0 & 0 & h_1(c_1+1) & 0 & 0 & 0 & 0 \\
0 & 0 & 0 & 0 & h_1(c_1+1) & 0 & 0 & 0 \\
0 & 0 & 0 & 0 & 0 & h_1(c_1+1) & 0 & 0 \\
0 & 0 & 0 & 0 & 0 & 0 & h_1(c_1+1) & 0 \\
0 & 0 & 0 & 0 & 0 & 0 & 0 & h_1(c_1+1) \\
D_9 & h_2(c_2+1) & h_2(c_2+1) & 0 & h_1(c_1+1) & 0 & 0 & 0 \\
h_2(c_2+1) & D_{10} & 0 & h_2(c_2+1) & 0 & h_1(c_1+1) & 0 & 0 \\
h_2(c_2+1) & 0 & D_{11} & h_2(c_2+1) & 0 & 0 & h_1(c_1+1) & 0 \\
0 & h_2(c_2+1) & h_2(c_2+1) & D_{12} & 0 & 0 & 0 & h_1(c_1+1) \\
h_1(c_1+1) & 0 & 0 & 0 & D_{13} & h_2(c_2+1) & h_2(c_2+1) & 0 \\
0 & h_1(c_1+1) & 0 & 0 & h_2(c_2+1) & D_{14} & 0 & h_2(c_2+1) \\
0 & 0 & h_1(c_1+1) & 0 & h_2(c_2+1) & 0 & D_{15} & h_2(c_2+1) \\
0 & 0 & 0 & h_1(c_1+1) & 0 & h_2(c_2+1) & h_2(c_2+1) & D_{16}
\end{pmatrix},$$

where the first matrix corresponds to rows 1 to 8 and the second one to rows 9 to 16 of the total matrix H_s. The diagonal elements are:

$D_1 = (\lambda_1 + \lambda_2) + \frac{1}{2}[U + U' + (U' - J)]$, $\quad D_2 = \lambda_1$,
$D_3 = \lambda$, $\quad D_4 = (\lambda_1 - \lambda_2) + \frac{1}{2}[U - U' - (U' - J)]$,
$D_5 = \lambda_2$, $\quad D_6 = \frac{1}{2}[-U - U' + (U' - J)]$,
$D_7 = \frac{1}{2}[-U + U' - (U' - J)]$, $\quad D_8 = -\lambda_2$,
$D_9 = \lambda_2$, $\quad D_{10} = \frac{1}{2}[-U + U' - (U' - J)]$,
$D_{11} = \frac{1}{2}[-U - U' + (U' - J)]$, $\quad D_{12} = -\lambda_2$,
$D_{13} = (\lambda_2 - \lambda_1) + \frac{1}{2}[U - U' - (U' - J)]$, $\quad D_{14} = -\lambda_1$,
$D_{15} = -\lambda_1$, $\quad D_{16} = (-\lambda_1 - \lambda_2) + \frac{1}{2}[U + U' + (U' - J)]$.

3.3.3 Five orbital case - Procedure and quasiparticle weight calculation

We move on to the five band case, where the situation is similar to the one treated on the two orbital level, with the fermionic hamiltonian H_f being now a 5x5 matrix that needs to be diagonalized. We chose to use the Ikeda five-band model [52], which includes the $d_{xz}, d_{yz}, d_{x^2-y^2}, d_{xy}, d_{z^2}$ Fe-orbitals. The band-structure and Fermi surface calculated within this model are shown in Fig.3.5, where we can see that the bandwidth is $W \approx 4eV$.

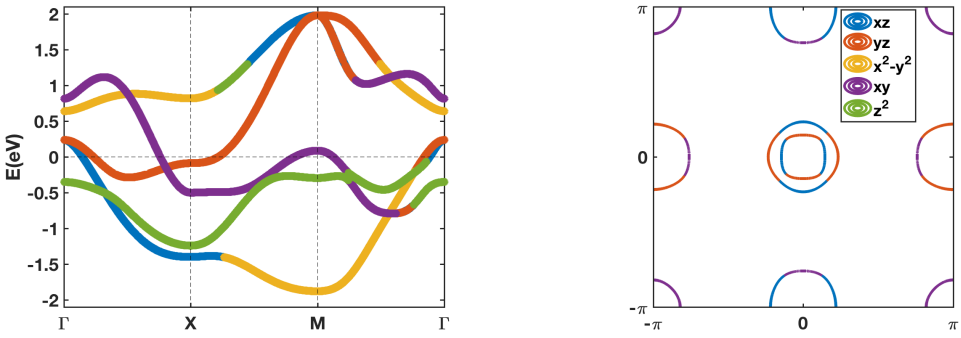

(a) (b)

Figure 3.5: (a) Band-structure of the five orbital Ikeda model along the path $\Gamma X M \Gamma$ with $\Gamma = (0,0), X = (\pi, 0), M = (\pi, \pi)$. (b) Fermi surface of the Ikeda model, where the C4 symmetry of the system is evident. The colors indicate which orbital is the low energy dominant one at each FS point.

Once again the final form of the Hamiltonian arrises after performing a Fourier transform and we get the expression:

$$\begin{aligned} H_f = \textstyle\sum_{k\sigma} \big[& (Z_1 - \lambda_1 - \mu)\epsilon_1(k) n^f_{k1\sigma} + (Z_2 - \lambda_2 - \mu)\epsilon_2(k) n^f_{k2\sigma} + \\ & + (Z_3 - \lambda_3 - \mu)\epsilon_3(k) n^f_{k3\sigma} + (Z_4 - \lambda_4 - \mu)\epsilon_4(k) n^f_{k4\sigma} + (Z_5 - \lambda_5 - \mu)\epsilon_5(k) n^f_{k5\sigma} + \\ & + \sqrt{Z_1 Z_2}\epsilon_{12}(k)(f^\dagger_{k1\sigma} f_{k2\sigma} + f^\dagger_{k2\sigma} f_{k1\sigma}) + \sqrt{Z_1 Z_3}\epsilon_{13}(k)(f^\dagger_{k1\sigma} f_{k3\sigma} + f^\dagger_{k3\sigma} f_{k1\sigma}) + \\ & + \sqrt{Z_1 Z_4}\epsilon_{14}(k)(f^\dagger_{k1\sigma} f_{k4\sigma} + f^\dagger_{k4\sigma} f_{k1\sigma}) + \sqrt{Z_1 Z_5}\epsilon_{15}(k)(f^\dagger_{k1\sigma} f_{k5\sigma} + f^\dagger_{k5\sigma} f_{k1\sigma}) + \\ & + \sqrt{Z_2 Z_3}\epsilon_{23}(k)(f^\dagger_{k2\sigma} f_{k3\sigma} + f^\dagger_{k3\sigma} f_{k2\sigma}) + \sqrt{Z_2 Z_4}\epsilon_{24}(k)(f^\dagger_{k2\sigma} f_{k4\sigma} + f^\dagger_{k4\sigma} f_{k2\sigma}) + \\ & + \sqrt{Z_2 Z_5}\epsilon_{25}(k)(f^\dagger_{k2\sigma} f_{k5\sigma} + f^\dagger_{k5\sigma} f_{k2\sigma}) + \sqrt{Z_3 Z_4}\epsilon_{34}(k)(f^\dagger_{k3\sigma} f_{k4\sigma} + f^\dagger_{k4\sigma} f_{k3\sigma}) + \\ & + \sqrt{Z_3 Z_5}\epsilon_{35}(k)(f^\dagger_{k3\sigma} f_{k5\sigma} + f^\dagger_{k5\sigma} f_{k3\sigma}) + \sqrt{Z_4 Z_5}\epsilon_{45}(k)(f^\dagger_{k4\sigma} f_{k5\sigma} + f^\dagger_{k5\sigma} f_{k4\sigma}) \big], \end{aligned} \tag{3.44}$$

where we have named the orbitals $xz \equiv 1, yz \equiv 2, x^2 - y^2 \equiv 3, xy \equiv 4$ and $z^2 \equiv 5$ and the dispersion relations in the Ikeda 5-band model are found in [52]. Now the coefficients h_m that we need to calculate will be:

$$h_{1\sigma} = \sqrt{Z_1}\sum_k \epsilon_1(k)\langle f^\dagger_{k1\sigma} f_{k1\sigma}\rangle_f + \sqrt{Z_2}\sum_k \epsilon_{12}(k)\langle f^\dagger_{k1\sigma} f_{k2\sigma}\rangle_f + \sqrt{Z_3}\sum_k \epsilon_{13}(k)\langle f^\dagger_{k1\sigma} f_{k3\sigma}\rangle_f + \\ + \sqrt{Z_4}\sum_k \epsilon_{14}(k)\langle f^\dagger_{k1\sigma} f_{k4\sigma}\rangle_f + \sqrt{Z_5}\sum_k \epsilon_{15}(k)\langle f^\dagger_{k1\sigma} f_{k5\sigma}\rangle_f = \sum_{m=1}^5 \sqrt{Z_m}\xi_{1m},$$
$$h_{2\sigma} = \sum_{m=1}^5 \sqrt{Z_m}\xi_{2m},$$
$$h_{3\sigma} = \sum_{m=1}^5 \sqrt{Z_m}\xi_{3m},$$
$$h_{4\sigma} = \sum_{m=1}^5 \sqrt{Z_m}\xi_{4m},$$
$$h_{5\sigma} = \sum_{m=1}^5 \sqrt{Z_m}\xi_{5m}, \tag{3.45}$$

with $\xi_{lm} = \sum_k \epsilon_{lm}(k)\langle f^\dagger_{kl\sigma} f_{km\sigma}\rangle_f$ and $\xi_{mm} \equiv \xi_m = \sum_k \epsilon_m(k)\langle f^\dagger_{km\sigma} f_{km\sigma}\rangle_f$. The basis we will use is a 4^5 vector, where each element includes the physical spin up - spin down pair for each of the five orbitals xz, yz, x^2-y^2, xy and z^2. We write down the first 16 elements and then the rest continue in the same pattern ending up with 1024 elements:

$$\begin{pmatrix} |\uparrow\uparrow,\uparrow\uparrow,\uparrow\uparrow,\uparrow\uparrow,\uparrow\uparrow\rangle \\ |\uparrow\uparrow,\uparrow\uparrow,\uparrow\uparrow,\uparrow\uparrow,\uparrow\downarrow\rangle \\ |\uparrow\uparrow,\uparrow\uparrow,\uparrow\uparrow,\uparrow\uparrow,\downarrow\uparrow\rangle \\ |\uparrow\uparrow,\uparrow\uparrow,\uparrow\uparrow,\uparrow\uparrow,\downarrow\downarrow\rangle \\ |\uparrow\uparrow,\uparrow\uparrow,\uparrow\uparrow,\uparrow\downarrow,\uparrow\uparrow\rangle \\ |\uparrow\uparrow,\uparrow\uparrow,\uparrow\uparrow,\uparrow\downarrow,\uparrow\downarrow\rangle \\ |\uparrow\uparrow,\uparrow\uparrow,\uparrow\uparrow,\uparrow\downarrow,\downarrow\uparrow\rangle \\ |\uparrow\uparrow,\uparrow\uparrow,\uparrow\uparrow,\uparrow\downarrow,\downarrow\downarrow\rangle \\ |\uparrow\uparrow,\uparrow\uparrow,\uparrow\uparrow,\downarrow\uparrow,\uparrow\uparrow\rangle \\ |\uparrow\uparrow,\uparrow\uparrow,\uparrow\uparrow,\downarrow\uparrow,\uparrow\downarrow\rangle \\ |\uparrow\uparrow,\uparrow\uparrow,\uparrow\uparrow,\downarrow\uparrow,\downarrow\uparrow\rangle \\ |\uparrow\uparrow,\uparrow\uparrow,\uparrow\uparrow,\downarrow\uparrow,\downarrow\downarrow\rangle \\ |\uparrow\uparrow,\uparrow\uparrow,\uparrow\uparrow,\downarrow\downarrow,\uparrow\uparrow\rangle \\ |\uparrow\uparrow,\uparrow\uparrow,\uparrow\uparrow,\downarrow\downarrow,\uparrow\downarrow\rangle \\ |\uparrow\uparrow,\uparrow\uparrow,\uparrow\uparrow,\downarrow\downarrow,\downarrow\uparrow\rangle \\ |\uparrow\uparrow,\uparrow\uparrow,\uparrow\uparrow,\downarrow\downarrow,\downarrow\downarrow\rangle \\ \vdots \\ \vdots \\ \vdots \end{pmatrix}. \tag{3.46}$$

Now, in order to get the hamiltonian H_s in matrix form we have to write down all the operators in the enlarged space of the five orbitals, with two slave spins for each of them, so as we mentioned above we have a 4^5x4^5 = 1024x1024 space. We will once again explicitly write down one of the terms and the rest is calculated in the same way:

$$\sum_{m,\sigma} h_m O_{m\sigma} = (h_1 O_{1\uparrow}\otimes I_{1\downarrow})\otimes I_2\otimes I_3\otimes I_4\otimes I_5 + (I_{1\uparrow}\otimes h_1 O_{1\downarrow})\otimes I_2\otimes I_3\otimes I_4\otimes I_5 + \\ I_1\otimes(h_2 O_{2\uparrow}\otimes I_{2\downarrow})\otimes I_3\otimes I_4\otimes I_5 + I_1\otimes(I_{2\uparrow}\otimes h_2 O_{2\downarrow})\otimes I_3\otimes I_4\otimes I_5 + \\ I_1\otimes I_2\otimes(h_3 O_{3\uparrow}\otimes I_{3\downarrow})\otimes I_4\otimes I_5 + I_1\otimes I_2\otimes(I_{3\uparrow}\otimes h_3 O_{3\downarrow})\otimes I_4\otimes I_5 + \\ I_1\otimes I_2\otimes I_3(h_4 O_{4\uparrow}\otimes I_{4\downarrow})\otimes I_5 + I_1\otimes I_2\otimes I_3(I_{4\uparrow}\otimes h_4 O_{4\downarrow})\otimes I_5 + \\ I_1\otimes I_2\otimes I_3\otimes I_4\otimes(h_5 O_{5\uparrow}\otimes I_{5\downarrow}) + I_1\otimes I_2\otimes I_3\otimes I_4\otimes(I_{5\uparrow}\otimes h_5 O_{5\downarrow}), \tag{3.47}$$

where the $I_{1,2,3,4,5\uparrow,\downarrow}$ are 2x2 identity matrices corresponding to the spin state of each orbital, while the $I_{1,2,3,4,5}$ are 4x4 identity matrices corresponding to the orbitals 1,2,3,4 and 5 respectively. This means that in a specific operation, for example the $I_1\otimes$

$(h_2 O_{2\uparrow} \otimes I_{2\downarrow}) \otimes I_3 \otimes I_4 \otimes I_5$, the orbitals 1,3,4 and 5 do not get affected. By writing all the operators in that form the H_s matrix is constructed.

3.3.4 Results for the multi-orbital case

We have formulated our model and we our now going to look into the results we get for the quasiparticle weights in various situations.

Degenerate bands with only intra-orbital hopping

Before we move on to the explicit models discussed in the previous section, we calculate as a first check the Z-factors for the simplest cases, where the two and five bands respectively are degenerate and there is no hopping between different orbitals (just simple hopping within each orbital of the form used in the single band case).

- **Only intra-orbital interactions**

We will start by looking at the case where there are no interactions between the orbitals ($U' = 0$ and $J = 0$), so there is only the intra-orbital Coulomb U. Following the procedure described in section 3.3.3, we find, as expected, that in both cases the quasiparticle weights are degenerate between the orbitals and the trend is identical to that of the one band case at half filling (so at $n = 2$ for the two bands and $n = 5$ for the five bands). That is because what we practically have now is two and five, respectively, copies of the single band model. In Fig.3.6a we see those plots on top of each other and it is obvious that they are identical.

- **Intra- and inter-orbital interactions**

The natural next step is to add interactions beyond the intra-orbital Coulomb repulsion U. For the degenerate two orbital model, with only intra-orbital hopping, we add inter-orbital interactions through U' and J (we remind the reader that $U' = U - 2J$, so it is not a free parameter) at half-filling and check how the quasiparticle weights change behavior compared to the previous case. We notice from Fig.3.6b that for $J = 0$, the effect of adding U' is to push the critical interaction strength for the Mott transition at much higher values. To explain this we look at the physical picture and notice that the ground state degeneracy has now increased, because it is proportional to the orbital number. This means that there is also an increase of the hopping channels with no energy cost, thus the "fight" for the energy gain between the particles' itineracy and the localization, now needs a much higher interaction strength to be won by the localization (leading to the Mott phase). By tuning the Hund's coupling J away from zero we observe in Fig.3.6b the opposite effect. The critical U value is now lowered and the reason is that Hund's rule favors the parallel alignment of the electron spins, so the degeneracy of the ground state is again reduced. More explicitly this can be seen in terms of the "Mott gap" and if we remind ourselves of the analysis we made in chapter 2, indeed at half-filling the criterion for transition into the Mott phase is $\Delta_{Mott} = U + (N-1)J - W = 0$, with N being the number of orbitals and W the bandwidth.

- **Dependence on number of orbitals**

Another interesting parameter to explore is the number of orbitals N. We take the case where the bands are degenerate with only intra-orbital hopping, including both intra-

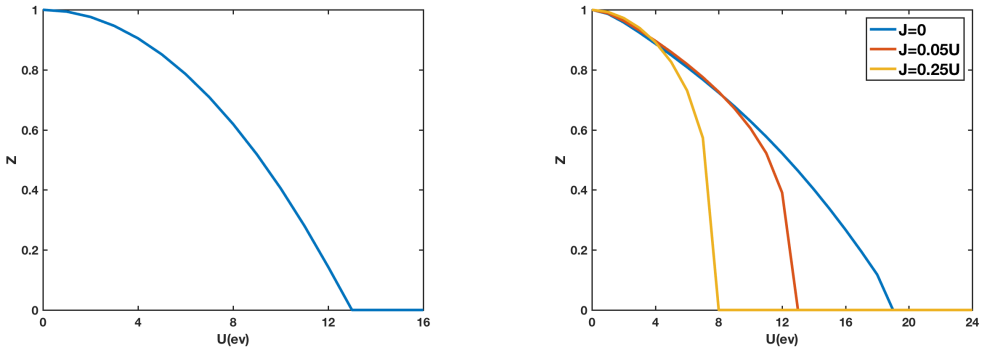

(a) (b)

Figure 3.6: (a) Quasiparticle weight of two and five degenerate bands, with only intra-orbital hopping and interactions. The plot lines are on top of each other and they are identical to the single orbital figure. (b) Quasiparticle weight of two degenerate bands, with only intra-orbital hopping but both intra- and inter-orbital interactions. Tuning up the value of Hund's coupling J pushes the critical interaction strength for transition to the Mott insulating phase towards lower values, so it favors localization. The temperature is $kT = 1meV$.

and inter-orbital interactions through U and U', but with Hund's coupling $J = 0$. We calculate the quasiparticle weights versus interaction strength for one, two, three and five orbitals. The combined plot 3.7 illustrates that, by increasing the number of orbitals, the critical interaction U_c for entering the Mott phase increases. This behavior can be understood again within the context of the ground state degeneracy, which becomes larger with increasing orbital number, thus creating more hopping channels and making the localization harder. Consequently, a stronger interaction parameter is needed to induce the Mott insulator transition.

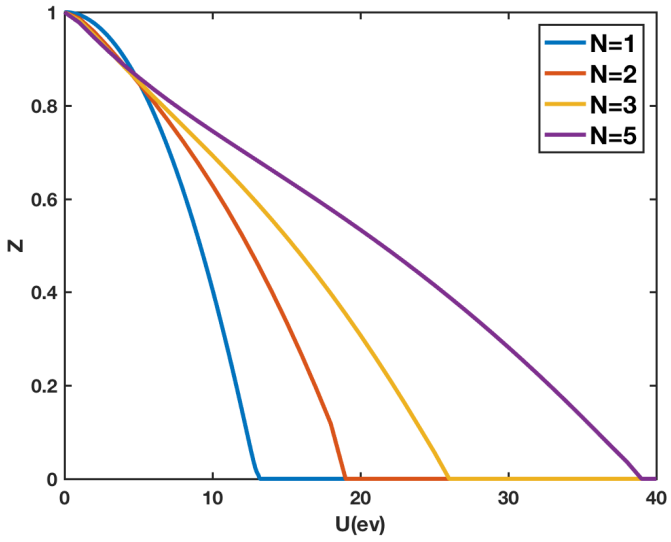

Figure 3.7: Critical interaction strength for different number of orbitals at half-filling. With increasing orbital number the critical U is increased as well.

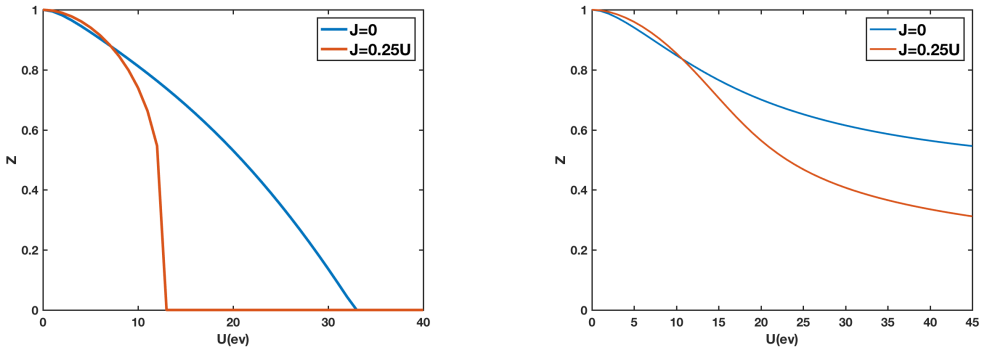

(a) (b)

Figure 3.8: (a) Quasiparticle weight in the Raghu model at half-filling $n = 2$ for Hund's coupling $J = 0$ and $J = 0.25U$. (b) Same calculation away from half-filling at $n = 1.5$. We see that at the second case there is no Mott localization, since the filling is not an integer number. Temperature $kT = 1meV$.

Raghu model for the two orbital case

Next we would like to move on to a more concrete, realistic band-structure, that includes off-diagonal hopping terms, and for that we use the Raghu model, introduced in section 3.3.2. At half-filling we first examine the $J = 0$ case and we see from Fig.3.8 that the system experiences a Mott transition at a large interaction strength, however we should keep in mind that the Raghu model also has a large bandwidth $W = 12eV$ and the ratio between those two parameters is actually what determines the degree of correlation. If we add a non-zero Hund's coupling $J = 0.25U$, the observed quasiparticle weight with respect to the interaction strength now drops faster and $U_c(J = 0.25U) \simeq 2.5U_c(J = 0)$. The explanation for this behavior is the one we gave also for the oversimplified band, related to the ground state degeneracy. Moving away from half-filling and repeating the same calculations for the case where $n = 1.5$, we arrive at a situation where the quasiparticle weight drops with increasing interaction, but never reaches zero as shown in Fig3.8. Rather it saturates at a mediocre value, in agreement with the statement that the Mott Insulator can appear only when there is an integer electron filling, otherwise the particles will never completely "freeze" in their positions. The system has strongly correlated electrons with large mass renormalization but not an infinite one.

Ikeda model for the five orbital case

Now we finally move on to a realistic model of a five orbital band structure and specifically we use the Ikeda model, already discussed in section 3.3.3. Now the orbitals are not degenerate (apart from the xz and yz), but they are rather split by a crystal field energy term. We use the filling $n = 6$, which is the one related to the parent compound, for this model. For the Hund's coupling parameter we chose $J = 0.25U$, according to other studies [46, 53], and we get that with increasing interaction strength, the system enters an *orbital selective Mott phase* (OSMP), where the quasiparticle weights for the five orbitals are split. We can interpret this behavior by thinking that at around $U \simeq 2.5eV$ there is a crossover from a weakly correlated system to a more strongly correlated one, where the five Z-factors saturate in different values, as shown in Fig.3.9. Therefore, we have now shown the emergence of this coexistence state,

already introduced in chapter 2 from relevant experiments, where some electrons are weakly correlated and other strongly. We observe that the xy orbital is the most strongly correlated one, in accordance with experimental findings. This orbital differentiation of the correlation strength has been proposed, also, from other methods, such as DMFT [54] and variational Montecarlo studies [55].

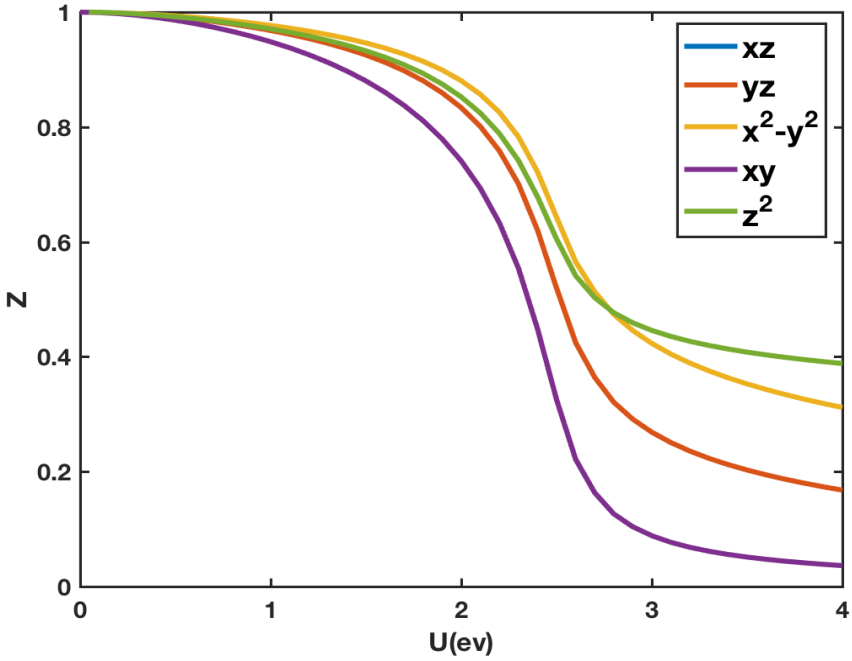

Figure 3.9: Ikeda model at n=6 filling with $J = 0.25U$ at $kT = 1meV$. Upon increasing interaction strength, the system undergoes a transition from a weakly correlated metal into an OSMP with strong correlations.

- **Behavior of individual orbital fillings**

An interesting thing to look at is how the densities of each orbital evolve with growing interaction strength. We can see in Fig.3.10 that the xy orbital has a density closest to half-filling ($n = 2n_\sigma = 1$, with n_σ we practically denote $n/2$, since we are looking at the paramagnetic phase), and so lives in proximity to the Mott insulating phase. This result is in agreement with the fact that d_{xy} is the most strongly correlated one. We also notice that at the crossover's critical interaction strength $U \simeq 2.5eV$ the xz/yz and the $x^2 - y^2$ orbitals switch order, following the behavior of the relevant quasiparticle weights. So when the system passes into the OSMP, the density of the xz/yz orbitals gets lowered, so closer to half-filling and accordingly the quasiparticle weights become smaller, thus there is stronger renormalization. The opposite happens to the $x^2 - y^2$ orbital.

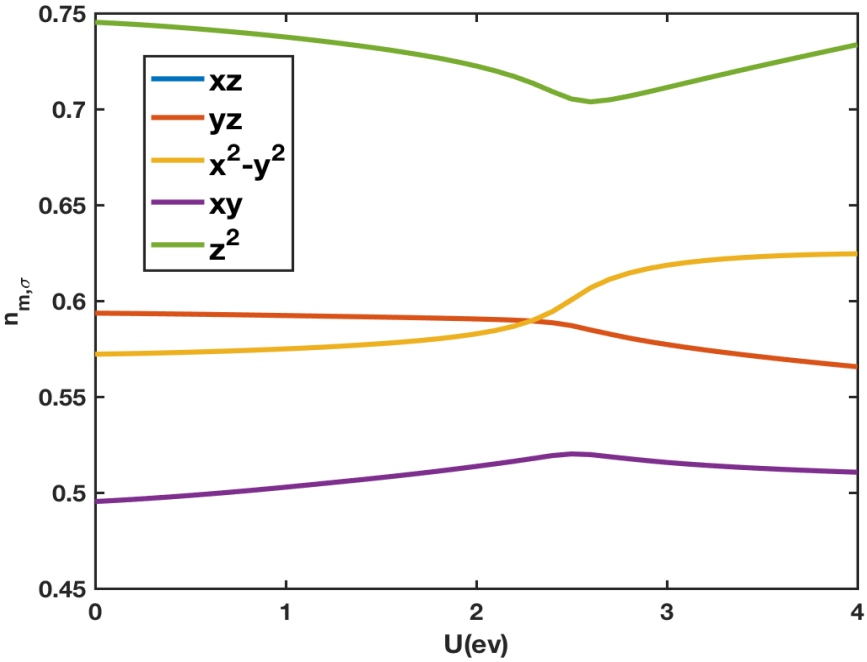

Figure 3.10: Individual orbital occupations at total filling n=6 and J=0.25U. We see that the most correlated xy orbital has its density close to half-filling, as expected.

- **Effect of electron filling**

We are now interested in exploring the effect of the electron filling in the quasiparticle weights. So far we have used $n = 6$ that is according to the bibliography the relevant one for the FeSC parent compounds [52], but what happens when we move away from this value? Below we plot the Z-factors versus interaction strength for $n = 5.81$ and $n = 6.13$. We note here that we chose this range because we know it's the one where the interesting features of the phase diagram appear [19]. What we observe from Fig.3.11, is that as we lower the electron density, so we hole dope the system towards half filling, the renormalization increases and correlations become stronger. Naturally, as we electron dope the system by increasing the filling, the opposite effect happens and the coupling is now weaker. However, it is clear that the discrepancy between those two different cases is not very large.

The tendency observed by varying the doping seems logical once we remind ourselves that as the system approaches half-filling, it is actually approaching the Mott insulator phase. In order to prove the above statement we make an additional calculation at half-filling $n = 5$. The result can be seen in Fig.3.11c and indeed at the critical interaction $U_c = 2$ the system experiences a transition into a Mott phase, with all the Z-factors becoming equal to zero.

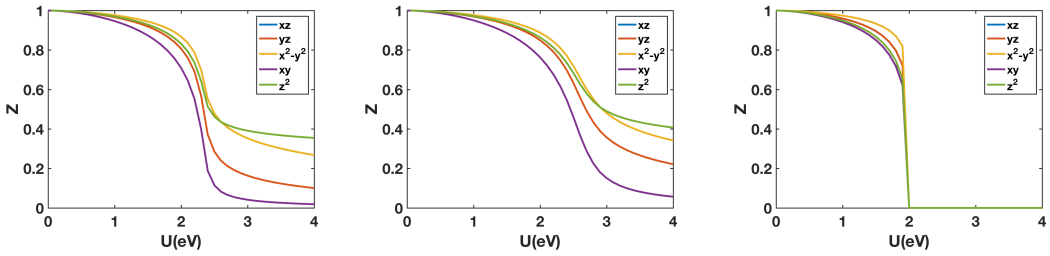

(a) (b) (c)

Figure 3.11: Quasiparticle weights for doping away from the parent compound's $n = 6$. (a) $n = 5.81$ (b) $n = 6.13$ (c) $n = 5$. We see that for the last case which is at half-filling the system enters a Mott insulating phase.

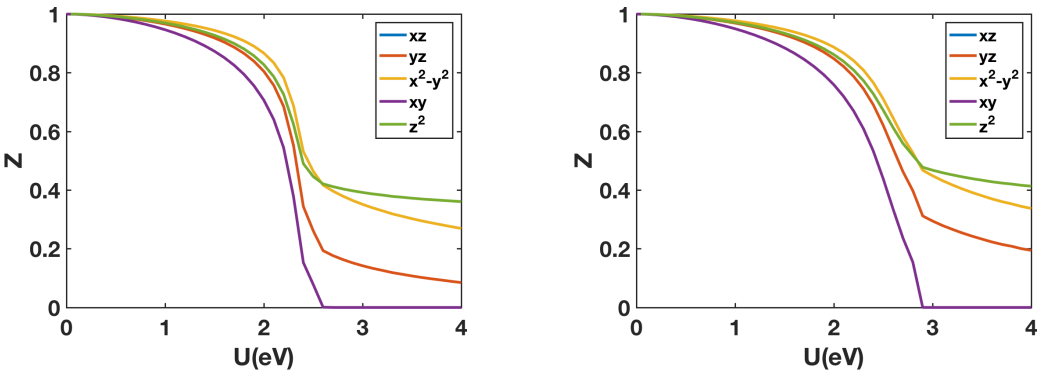

(a) (b)

Figure 3.12: (a) Quasiparticle weights for filling $n = 5.81$ at $kT = 50meV$. (b) Quasiparticle weights for filling $n = 6.13$ at $kT = 50meV$. We see that the temperature increase has a prominent effect especially in d_{xy} that gets completely localized, in both limits of doping.

- **Effect of temperature**

Thinking in a similar spirit as we did when varying the electron filling, we now check what result we get for moving on the temperature axis. Up until now we have been using $T \simeq 11.6K \rightarrow kT = 1meV$, that is a low enough value for the Fermi liquid theory to be valid. We know, though, that in the phase diagram of the FeSC the temperature parameter reaches values as high as $kT = 50meV$ [19]. For that reason, we calculate now the quasiparticle weights as a function of interaction strength at $kT = 50meV$, for fillings $n = 5.81$, $n = 6$ and $n = 6.13$. Upon plotting the results in Fig.3.12a,3.12b and 3.13a we come across a significant change, since for all the three fillings the weight of the "heaviest" quasiparticle d_{xy} gets now massively suppressed and becomes zero. This means that this orbital is now completely localized and has entered a Mott insulating phase, while the others are still mass-renormalized but not localized. To understand this we plot in Fig.3.13b, for the case of $n = 6$, the evolution of the individual orbital occupations and see that for the d_{xy} the filling after the critical value $U \simeq 2.6eV$ becomes $n_{yz} = 1$, thus this individual orbital indeed is at half-filling and that is why it obtains a zero quasiparticle weight.

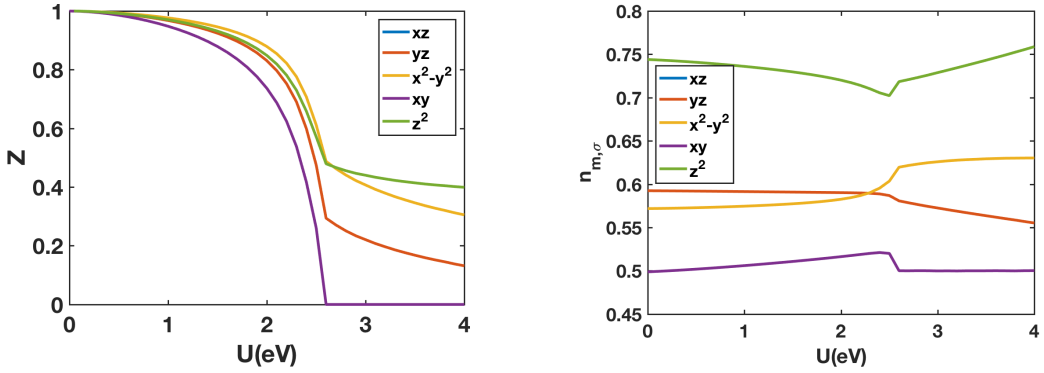

(a) (b)

Figure 3.13: (a) Quasiparticle weights for filling $n = 6$ at $kT = 50meV$. (b) Individual orbital fillings for the same case exhibiting that the complete suppression of the d_{xy} Z-factor goes side-to-side with its orbital occupation reaching the "half-filling" value $n_{xy,\sigma} = 0.5$.

- **Renormalized band-structure and Fermi surface**

In the slave spin formalism, the quasiparticle weights enter in the Hamiltonian as pre-factors, which renormalize the hopping terms. This means that in the interacting situations, where the Z-factors are less than unity, the hoppings will now be smaller than in the non-interacting limit, leading to a reshaping of the band-structure. Our understanding of the model tells us that the bands will now be squeezed and to see that, we plot the renormalized band-structure for different critical interaction strengths in Fig.3.14. Indeed there we observe the expected tendency of the bandwidth, decreasing as we increase U. If we remind ourselves of the experimental overview we gave in chapter 2, we will find that our results confirm the ones from various measurements. For example, with ARPES one actually performs measurements of energy dispersions, so our results are in agreement with the strong band renormalization and mass enhancement found there. The same applies for example for the specific heat measurements, where the Sommerfeld coefficient is proportional to the density of states. The exhibited band renormalization from such measurements also validates our results through the slave spin method. In complete accordance, the Fermi surface map follows the same tendency and the pockets (mainly the central ones) now get reshaped as we can see in Fig.3.15.

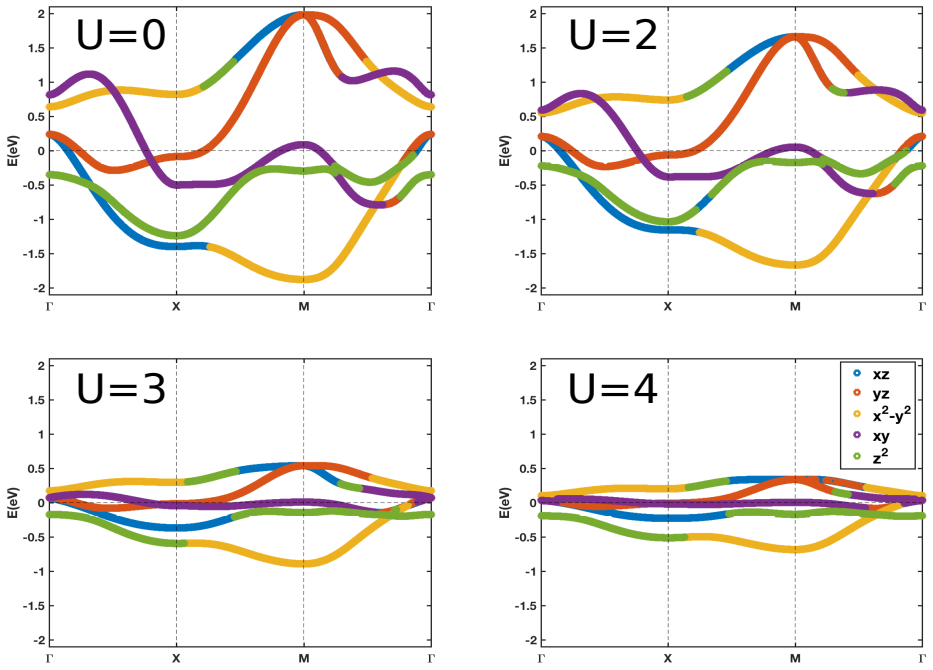

Figure 3.14: Band-structure renormalization. At $U = 0$ the bandwidth is $W \simeq 4eV$ and as we tune up the interactions to $U = 2, 3, 4eV$ we see a gradual "squeezing" of the total band-structure, meaning a decrease in the bandwidth, which at $U = 4eV$ becomes a bit larger than $W = 1eV$.

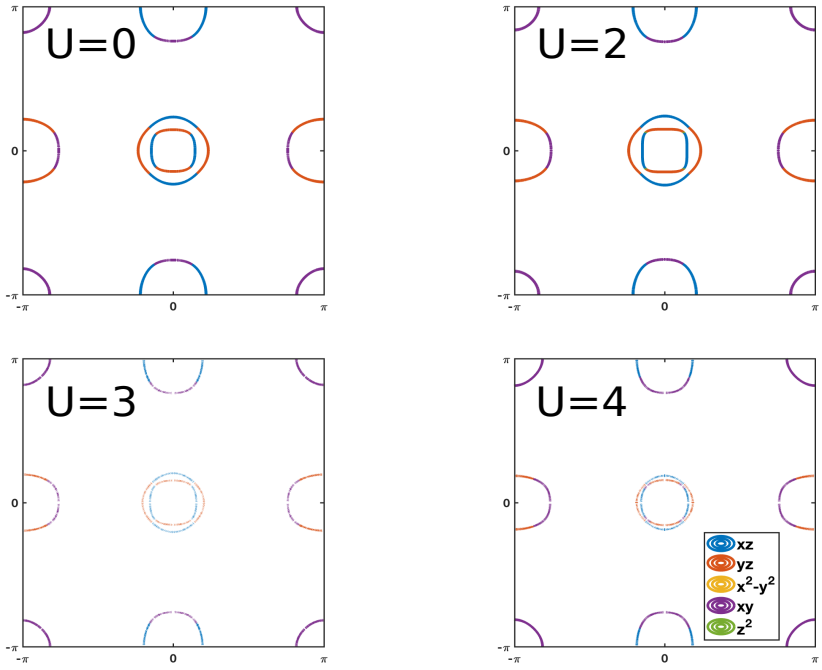

Figure 3.15: Fermi surface renormalization. The central pocket's width is notably suppressed, but small reshaping of the other pockets is observed.

3.4 Nematic state

As we have already pointed out in chapter 2, we are interested in the nematic state, where the system undergoes a structural transition generated by electronic interactions, making the x and y directions inequivalent. This is related to the lifting of the degeneracy between the xz and yz orbitals. Ideally, in order to explore this state we should reconstruct all of our band representation. However, as we analyzed earlier, the actual structural distortion is very small, while compared to that, the energetic splitting between d_{xz} and d_{yz} is relatively large. This makes us conclude that the main effect of nematicity can be captured simply by adding "by hand" a small splitting in the xz and yz energies. In this section, motivated by the experiment on FeSe and its relevant analysis in [39] discussed in chapter 2, we will attempt to look into the effect of such a small energy splitting on the quasiparticle weights. The reader should keep in mind that the band we are using is not the specific one for FeSe, but it is a generic band, representative of FeSC systems. Nevertheless, what we would like to explore is the possibility of a small energy splitting generating a large Z_{xz},Z_{yz} discrepancy, within the slave spin approach, and that should not depend highly on the details of the band-structure.

The first step is to figure out in which form we should add the splitting and what value we should ascribe to it. We return to the experimental data and the information we obtain indicate that at the $\Gamma = (0, 0)$ point of the Brillouin zone, the measured energy difference between d_{xz},d_{yz} is approximately $20meV$ [39]. This will be our guideline for the following calculations.

- **s-wave nematic order**

The simplest way to include nematicity in our system is through an s-wave type splitting by writing $H_o = \delta_o(n_{xz} - n_{yz})$. This is an on-site energy term, so it will not be renormalized by the quasiparticle weights. Motivated by the experimental result [39], we start by setting $\delta_o = 10meV$, so that the energy difference between the two orbitals is $\Delta_o = 2\delta_o = 20meV$. We see in Fig.3.16a that the calculated Z_{xz} and Z_{yz} exhibit a very small difference. However, there is an effect we did not take into consideration. Even though H_o does not get renormalized, the whole band-structure will be renormalized by the Z-factors, meaning that the value we ascribe to δ_o is related to the non-interacting case. In the experiments, though, the measured quantities obviously correspond to reality, which is far from the non-interacting limit. Consequently, at $U \neq 0$ the energy splitting of d_{xz} and d_{yz} will be smaller than Δ_o and we name it $\tilde{\Delta}_o$. In order to look into that we repeat the previous calculation with a larger $\delta_o = 50meV$. Fig.3.16b shows that the Z-factor difference has now increased ($Z_{xz}/Z_{yz} \approx 0.78$ at the OSMP), but it is still not as large as we would anticipate.

We plot the band-structure for the latest case with $\delta_o = 50meV$ in Fig.3.17a. Indeed at $U = 0$ the difference of the xz and yz energies at the Γ point is $\Delta_o = 2\delta_o = 100meV$. At the interacting situation with $U = 4$, though, we observe in Fig.3.17b that $\tilde{\Delta}_o \approx 50meV$, due to the feedback effects of the orbitally dependent quasiparticle weights. This means that in order to get the $20meV$ energy splitting, we should start with a $\delta_o > 10meV$ so that upon renormalization $\tilde{\Delta}_o = 20meV$. We can say, nonetheless, that with $10meV < \delta_o < 50meV$, the Z-factors will not exhibit the discrepancy we would like to observe for the xz and yz orbitals.

This motivates us to take a step back and reconsider the way we introduced the nematic order in the Hamiltonian. If we return to the experimental situation, we realize that there, they report a modulation of the energy difference between d_{xz} and

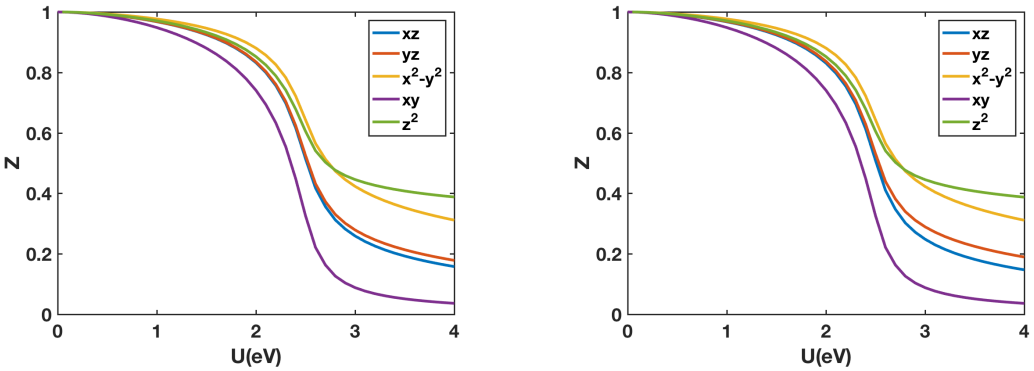

(a) (b)

Figure 3.16: Ikeda model at n=6 filling, with $J = 0.25U$ and xz/yz s-wave split for (a) $\delta_o = 15meV$, (b) $\delta_o = 50meV$. We see that for the case with larger δ, there is a larger splitting between Z_{xz} and Z_{yz}, but still it is not significantly large.

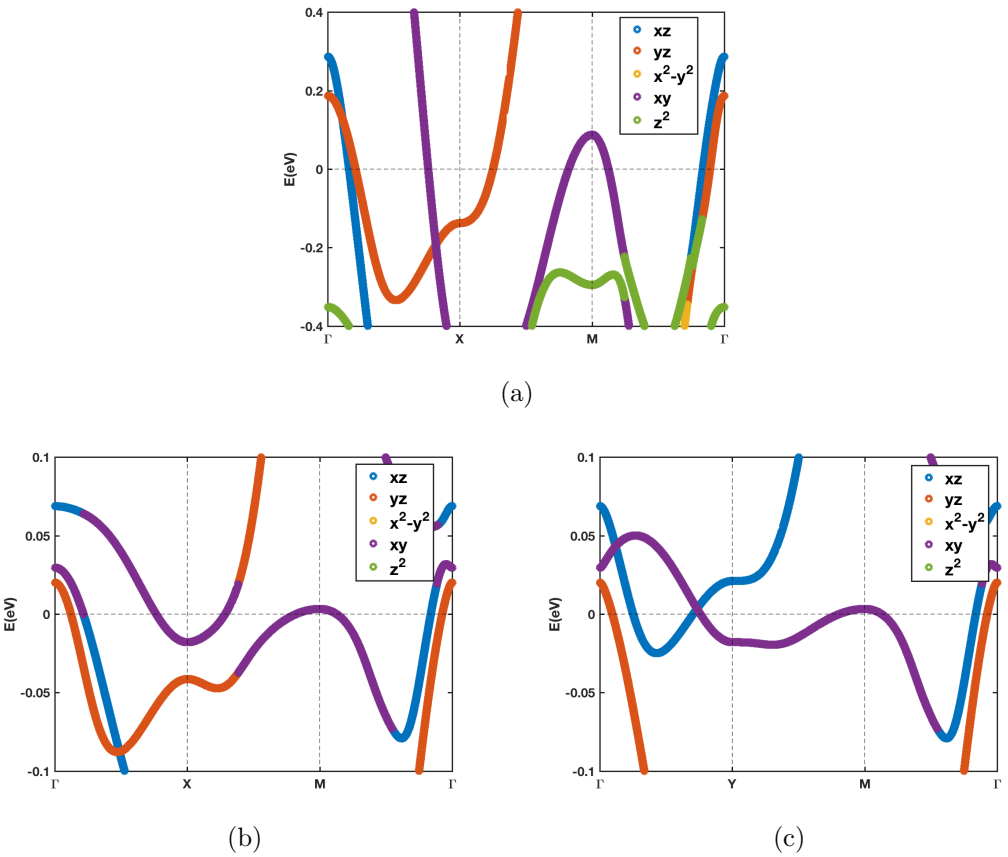

(a)

(b) (c)

Figure 3.17: Band-structure around the Fermi energy of the Ikeda model with an additional s-wave nematic order term, $\delta_o = 50meV$. (a) Non-interacting limit $U = 0$. (b) Interacting case with $U = 4eV$ at the $\Gamma XM\Gamma$ cut. (c) $U = 4eV$ at the $\Gamma YM\Gamma$ cut. We observe at the Γ point the renormalization of the E_{xz},E_{yz} difference $\Delta_o = 100meV$, which becomes $\tilde{\Delta}_o \approx 50meV$ (notice the different scale in the two plots). $\tilde{E}_{xz}(\Gamma) - \tilde{E}_{yz}(\Gamma) \approx 50meV$,$\tilde{E}_{yz}(X) - \tilde{E}_{xz}(Y) \approx 60meV$.

d_{yz} across the Brillouin zone, in agreement with other experimental findings [39,56,57]. In fact, they find that at the M point, the d_{xz} and d_{yz} bands are split by $\sim 20meV$, but the order is now reversed. At Γ the xz orbital's energy is higher than the yz, but at M it is the other way around. In Fig.3.18 we see the results of ARPES measurements from [57] around the M point. We can see that there is an electron pocket crossing the Fermi level around that point and a hole pocket at lower energies. After performing an analysis, the description of which is not relevant for this thesis, the writers of this paper identify the electron pocket being of yz orbital origin and the hole one of xz. Within this analysis, they report that the energy difference we see in Fig.3.18 is also related to the structural distortion, so only a fraction of the ΔE we see should be identified with the orbital order splitting. The appearance of this degeneracy lifting in the nematic phase is more clearly illustrated in Fig.3.19, where they also plot the measured energy dispersion as a function of temperature. There we see that below $T = 90K$, which is the critical temperature for the nematic transition, there is an observed lifting of the d_{xz}, d_{yz} energy degeneracy (we focus on the e'_l and e''_h bands). The same group performed one year later more ARPES measurements on FeSe [56] and managed to obtain the band-structure picture around the Γ point. In Fig.3.20 we see that at $T = 160K$, so above the nematic transition, the xz orbital (red color in the third panel) appears to have larger energy than the yz one (green color). Upon cooling, we can see that at $T = 30K$, d_{yz} moves upward, while d_{xz} moves downward, having eventually reversed order compared to the M point discussed before.

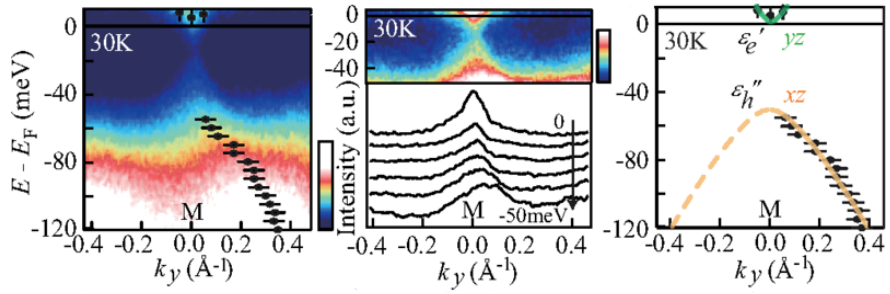

Figure 3.18: The two first plots are ARPES images demonstrating an electron pocket crossing the Fermi energy and a hole pocket in lower energies, around the M point. The second plot is a high-contrast figure. The third one is a schematic illustration of the band dispersions. We see that $E_{yz} > E_{xz}$. From [57].

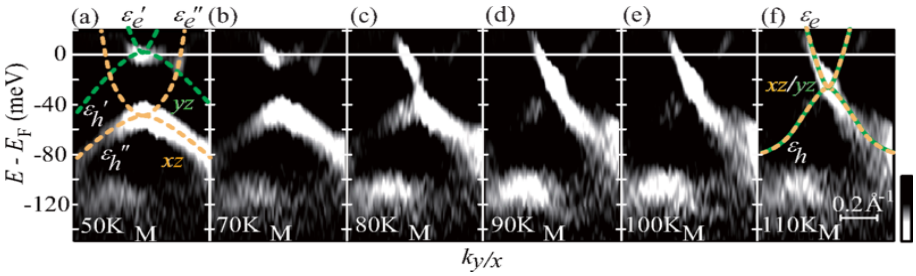

Figure 3.19: Lifting of the d_{xz}, d_{yz} degeneracy upon temperature lowering, below the nematic transition. From [57].

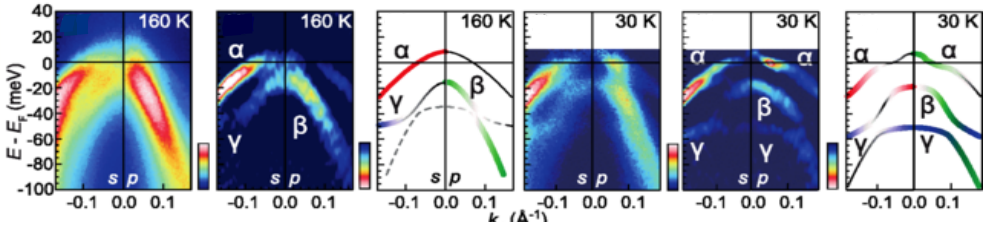

Figure 3.20: ARPES images and schematic band dispersions around the Γ point, for $T = 160K$ and $T = 30K$. We see that upon cooling below the nematic transition, the energy of d_{yz} moves upwards, while the one of d_{xz} moves downwards, leading to $E_{yz} > E_{xz}$ at the Γ point. From [56].

When comparing our results with the experimental data, though, we should be very careful. When they are naming the k-points they are looking at, they use the folded Brillouin zone, the correspondence of which with the unfolded one was introduced in chapter 1. The M point in this scheme is translated to our model as following: when they compare the d_{xz} with the d_{yz} energy at the M point, we should be comparing the d_{yz} energy at the $X = (\pi, 0)$ point with the d_{xz} one at the $Y = (0, \pi)$ point. These results are in agreement with the findings of [39], that we introduced in chapter 2. There, as we have explained earlier, they renormalize the band by including quasiparticle weights in the Hamiltonian, which they calculate by fitting to the experimental data. The band-structure they obtain is shown in Fig.3.21, where we can see the d_{xz}, d_{yz} band inversion between the Γ point and the combination of X and Y points, in the way we explained above.

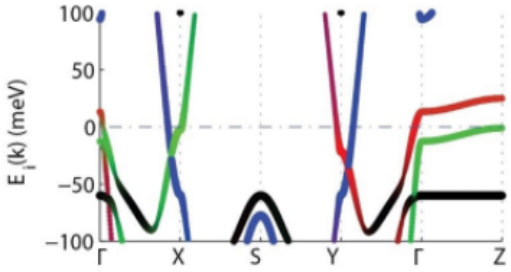

Figure 3.21: Renormalized band-structure including Z-factors fitted to the experimental data. Red corresponds to d_{xz} and green to d_{yz}. We observe the band inversion between the Γ point (where $E_{xz}(\Gamma) > E_{yz}(\Gamma)$) and the $X - Y$ points combination (with $E_{xz}(Y) < E_{yz}(X)$). From the Supplementary Material of [39].

Looking at d_{xz} in Fig.3.17c and d_{yz} in Fig.3.17b, we can see that $\tilde{E}_{xz} > \tilde{E}_{yz}$ and $\tilde{\Delta}_o \approx 60meV$. This means that the s-wave approach of the nematic order is insufficient, since it can not induce a change in the energy bands' order across the Brillouin zone.

- **d-wave nematic order**

Indeed, the on-site energies of the two orbitals will be non-degenerate and that is captured in the s-wave form of the nematic order we gave above. However, the experimentally calculated band-structure indicates, as we noted, that the splitting between the xz, yz orbitals is not the same along the Brillouin zone, but it changes as a function of momentum. This can be captured by adding in the Hamiltonian a d-wave term $H_b = \delta_b(\cos k_x - \cos k_y)(n_{xz} + n_{yz})$, where with δ_b we denote the "bond-order", which is actually a hopping term. This means that in our slave spin representation it should be included in the Hamiltonian together with the other hopping terms, and thus get renormalized by the Z-factors. It is obvious that $\tilde{\Delta}_b$ (the energy difference of d_{xz} and d_{yz} at $U \neq 0$) will be different than Δ_b (the energy difference of d_{xz} and d_{yz} at $U = 0$), so we choose to implement the above for $\delta_b = 50meV$. We arrive at the result of Fig. 3.22a, which shows that $Z_{xz}/Z_{yz} \approx 0.73$ at the OSMP.

We will once again look into the band-structure to gain some more information about the actual energy difference our choice has promoted. First, as a check we take the non-interacting case. We expect that at the Γ point, the d_{xz} and d_{yz} bands will be degenerate, because $E^b_{xz}(\Gamma) = E^b_{yz}(\Gamma) = \delta_b(1-1) = 0$ and so $\Delta_b(\Gamma) = 0$. On the other hand, E^b_{yz} at the X point must be different from E^b_{xz} at the Y point, since $E^b_{yz}(X) = \delta_b(-1-1) = 50 \cdot (-2) = -100meV$ and $E^b_{xz}(Y) = \delta_b(1+1) = 50 \cdot 2 = +100meV$, inducing a difference $\Delta_b(XY) = |E_{xz} - E_{yz}| = 200meV$. These can be verified from Fig.3.23a,3.23b, where we can see the degeneracy at Γ and the $200meV$ difference between the red line in Fig.3.23a and the blue one in Fig.3.23b at the X and Y points respectively.

Next we can look into the interacting case ($U = 4$) and let us start from the Γ point. We see in Fig.3.23c that the degeneracy is now lifted and $\tilde{\Delta}_b(\Gamma) \approx 20meV$. Even though $E^b_{xz}(\Gamma) = E^b_{yz}(\Gamma) = 0$, these objects are not equivalent to the $\tilde{E}_{xz}(\Gamma)$ and $\tilde{E}_{yz}(\Gamma)$ we see in the band-structure. That is the result of the feedback effects of the quasiparticle weights, which are now unequal for d_{xz} and d_{yz}. Hence, when they are included in the Hamiltonian they renormalize the two bands differently, giving rise to the degeneracy lifting at Γ, where we observe that $\tilde{E}_{yz} > \tilde{E}_{xz}$. Comparing now $\tilde{E}_{yz}$ at X with $\tilde{E}_{xz}$ at Y, we observe that $\tilde{\Delta}_b(XY) \approx 30meV$ and the order is now indeed reversed, with $\tilde{E}_{xz} > \tilde{E}_{yz}$. However, we obtain the wrong order, because according to the experiment $\tilde{E}_{xz} > \tilde{E}_{yz}$ at the Γ point and $\tilde{E}_{xz} < \tilde{E}_{yz}$ at the X-Y points.

It looks like the correct approach demands a negative δ_b and we plot in Fig.3.22b the quasiparticle weight as a function of interaction for $\delta_b = -50meV$. In this case $Z_{xz} > Z_{yz}$, which is in contrast to the experimental findings. However, as we expected the band-structure exhibits now the correct order. If we look at Fig.3.23g,3.23h, we can observe that we have obtained the exact same results as in the previous case (where $\delta_b = 50meV$), but now the blue and red bands are switched, so at the Γ point $\tilde{E}_{xz} > \tilde{E}_{yz}$ and from the comparison of the X and Y points $\tilde{E}_{xz} < \tilde{E}_{yz}$. We have arrived at a result where $\tilde{\Delta}_b(\Gamma) \approx 20meV$ and $\tilde{\Delta}_b(XY) \approx 30meV$, which is very close to the experiment. To the contrary, though, the Z-factors have the wrong order, so we conclude that a d-wave nematic order cannot account for the experimental data.

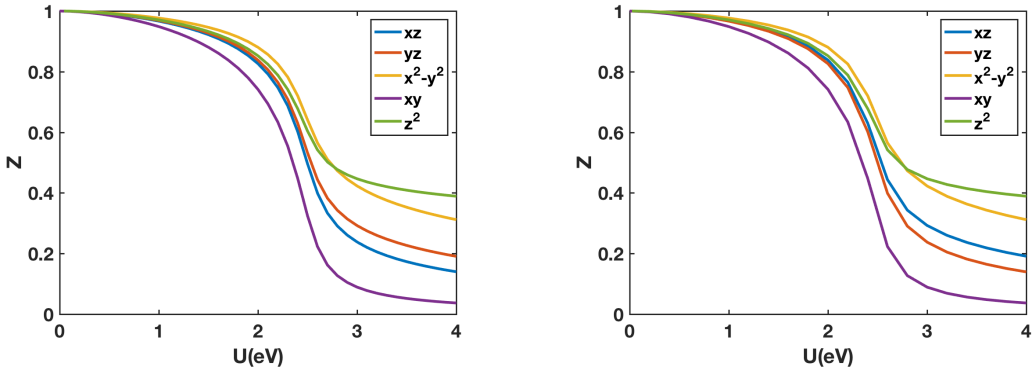

(a) (b)

Figure 3.22: Ikeda model at n=6 filling with $J = 0.25U$ and xz/yz d-wave splitting, for (a) $\delta_b = 50meV$, (b) $\delta_b = -50meV$. We observe that the two results are identical, but the Z_{xz} and Z_{yz} have been switched. The experimental results indicate that the correct order is $Z_{xz} < Z_{yz}$, so the one of $\delta_b > 0$. This choice, though, does not generate the correct band-structure.

- **s+d-wave nematic order**

At this point, motivated by the analysis made on the experimental results of [39] and the insufficiency of the s and d-wave splittings to produce a large $Z_{yz} - Z_{xz}$ difference, we implement a combination of an s and a d-wave type splitting. The relevant term in the Hamiltonian will now be $H_{ob} = \delta_o(n_{xz} + n_{yz}) + \delta_b(\cos k_x - \cos k_y)(n_{xz} - n_{yz})$. As before, the "bond-order" δ_b is a hopping term and therefore the relevant term must be renormalized by the Z-factors. On the other hand, δ_o is related to an on-site term, so it does not get renormalized. We remind the reader that the experimental findings suggest that both at the Γ and the M point (translated to combination of X and Y in our representation), there is an energy splitting of the order of $20meV$ between d_{xz} and d_{yz}, related to the orbital ordering. Moreover, there is a change in the order of the relevant bands, with the d_{xz} one being higher than the d_{yz} one at the Γ point and the opposite happening at the M point. Following the analysis made for the simple s- and d-wave types, we conclude that the appropriate form of the Hamiltonian includes a positive δ_o and a negative δ_b. Choosing the actual values for those objects becomes very complicated due to the feedback effects. We need a large δ_o so that upon renormalization it will lead to the correct energy splitting, but we also need a large negative δ_b to create the band reversion at the M point. After studying various combinations, we conclude that the one generating the experimental energy splittings consists of $\delta_o = 70meV$ and $\delta_b = -80meV$. In Fig.3.24 the band-structures along the $\Gamma XM\Gamma$ and $\Gamma YM\Gamma$ paths are illustrated, where we can indeed see that $\tilde{\Delta}_{ob}(\Gamma) \simeq 25meV$ and $\tilde{\Delta}_{ob}(XY) \simeq 20meV$. We plot in Fig.3.25 the quasiparticle weights as a function of interaction and we observe that at the OSMP, where the Z_{xz}, Z_{yz} difference is largest, their ratio is $Z_{xz}/Z_{yz} \simeq 0.78$. This value is not in agreement with the experimental situation, where this ratio was < 0.5. Therefore, even upon including an s+d-wave type nematic order which induced the correct form of the band-structure, we did not manage to verify the suggestion of [39] on the Z_{xz}, Z_{yz} ratio, within the slave spin method.

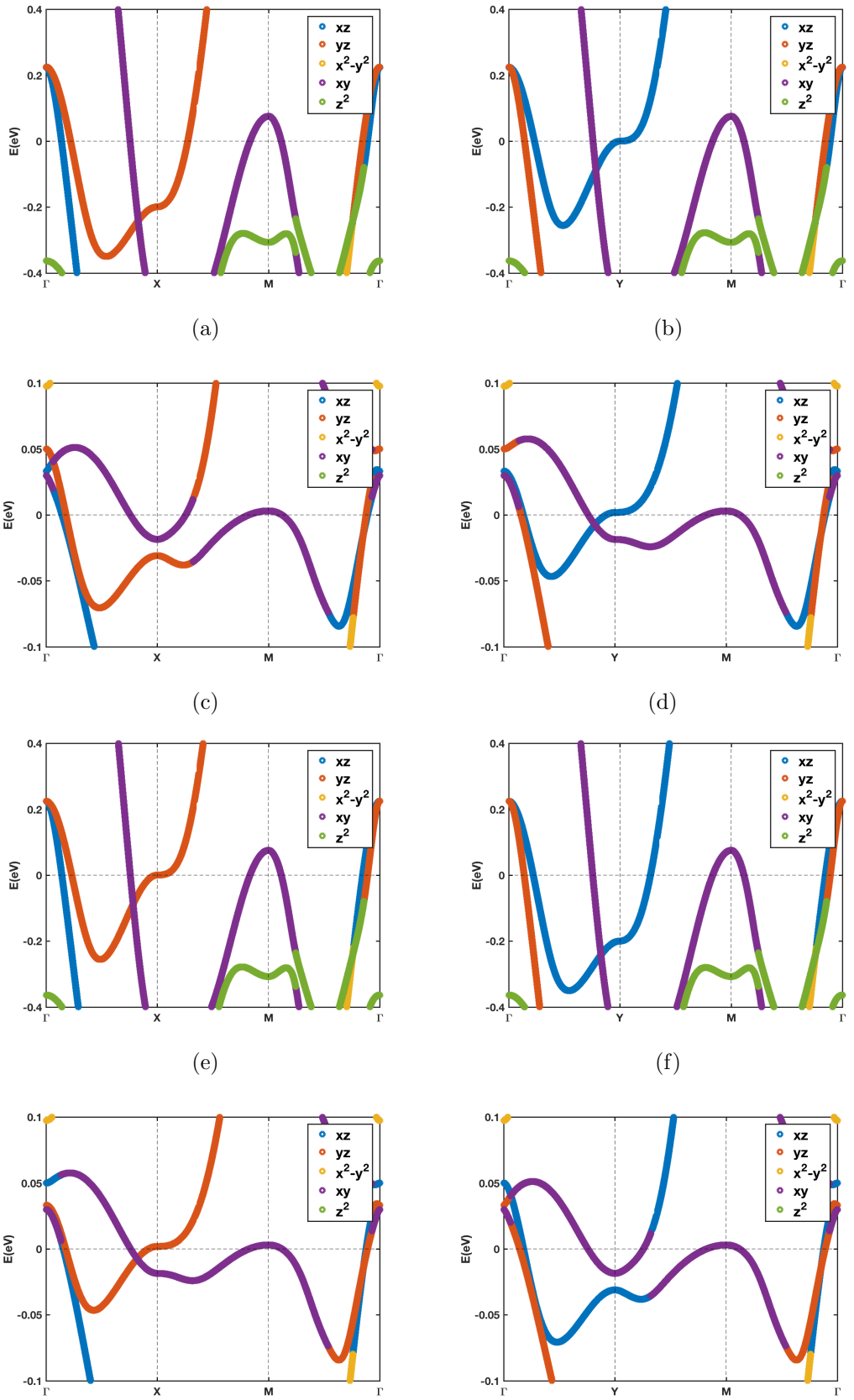

Figure 3.23: Band-structure around the Fermi energy of the Ikeda model with an additional d-wave nematic order term (a)-(d)$\delta_b = 50meV$, (e)-(h)$\delta_b = -50meV$. First and third line correspond to $U = 0$. Second and fourth line to $U = 4eV$.

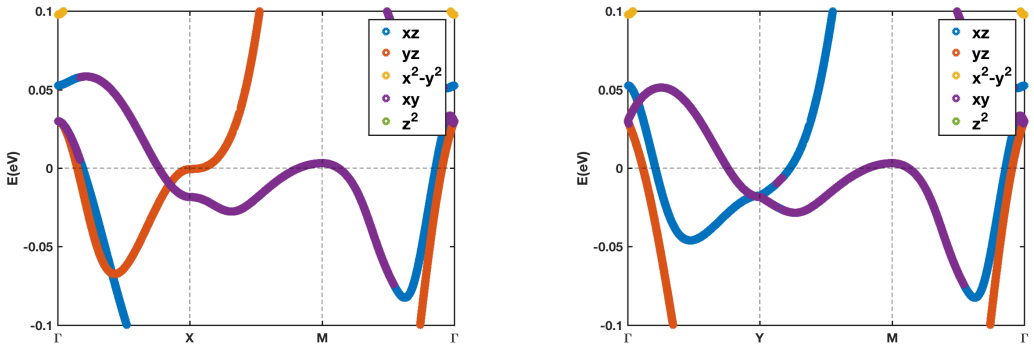

(a) (b)

Figure 3.24: Band-structure around the Fermi energy of the Ikeda model with an additional s+d-wave nematic order term, where $\delta_o = 70meV$ and $\delta_b = -80meV$. At the Γ point the energy difference of d_{xz} and d_{yz} is $\simeq 25meV$, and comparing the energy of d_{xz} at the Y point with d_{yz} at the X point, we see that their difference is $\simeq 20meV$. These values reproduce the experimental findings and the correct order is observed.

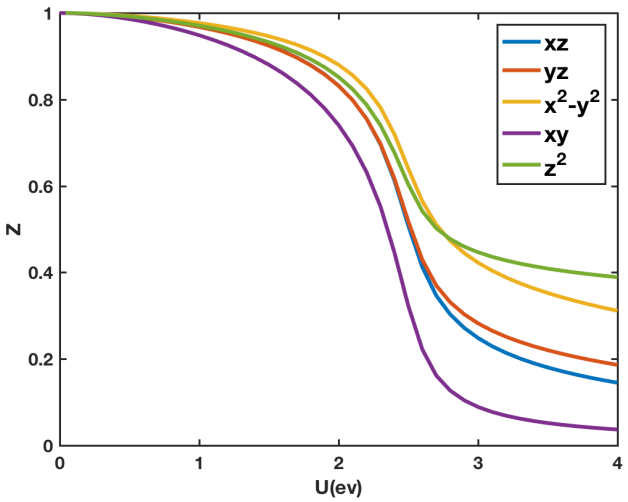

Figure 3.25: Ikeda model at n=6 filling with $J = 0.25U$ and xz/yz s+d-wave split, $\delta_o = 70meV$, $\delta_b = -80meV$, at $kT = 1meV$. We see that even at the OSMP the difference between Z_{xz} and Z_{yz} does not reach the large values observed in the experimental results, where $Z_{xz}/Z_{yz} < 0.50$.

3.5 Discussion

In this chapter we looked into the limit of strong electronic correlations in the FeSC. To this end, we implemented the slave spin method and showed the emergence of an OSMP in FeSC compounds. Upon increasing the strength of interactions there is a crossover from a weakly correlated metallic state to an OSMP, where there are stronger correlations accompanied by a significant differentiation among the orbitals' quasiparticle weights. This co-existence of strongly and weakly correlated electrons

can explain the results of various experiments, introduced in chapter 2, exhibiting such large discrepancies in their measurements.

In the last section of the chapter we studied the nematic phase. Motivated by experimental results on FeSe and a suggestion on their interpretation by [39], we considered whether a small energy splitting between the xz and yz orbitals could induce a large difference in their quasiparticle weights. We found out that incorporating the appropriate term in the Hamiltonian, gave rise to a notable discrepancy in Z_{xz} and Z_{yz}, but not as large as [39] suggested. This disagreement between experimental interpretation and theoretical results could be related to the method we used. Within the slave spin approach, the interactions are treated in a local level, thus we have been ignoring the momentum dependence of the self-energy. In the following chapter we will explore this limit, by implementing a different method.

Chapter 4

Momentum dependence of the self-energy

In the previous chapter, we introduced the slave spin technique in order to investigate the quasiparticle weights of FeSC compounds, by assuming strong correlations. Using this method we showed the emergence of an OSMP, which has appeared in a number of experiments [32–34]. However, we could not reproduce the suggested results from [39] on the nematic phase of FeSe. This could be related to the fact that the slave spin method captures the properties of the system arising from local interactions. It has been shown, though, that the nematic phase of FeSe is in close proximity to a magnetic one [35,58,59]. Under ambient pressure FeSe does not exhibit a magnetic transition, but upon applied pressure a magnetic dome appears. Antiferromagnetic spin fluctuations have been studied in the nematic phase with ambient pressure and it appears that they are existent and strong. There are competing magnetic states, leading to a final picture with no long range magnetic order, and with the nematic state present until low temperatures. Therefore, momentum dependence seems to be a parameter that we should not neglect when working on FeSe.

In this chapter we will explore this momentum dependence of the self-energy and assume that spin fluctuations play a major role in the system's physical processes. We will, once again, attempt to extract the quasiparticle weights in this context, and we will do it through the calculation of the self-energy. The two methods (slave spin and self-energy) tackle the same problem by encapsulating different physical processes, therefore a direct comparison of their results is inconsistent. It is interesting, however, to study both of them, for the normal as well as the nematic state that we have focused on throughout this thesis.

We will apply a two orbital model, as the five orbital problem is computationally very demanding. This allows us to obtain qualitative results concerning the effects of nematicity on the quasiparticle weights.

4.1 Susceptibility calculation

Before we are ready to explore the self-energy of the system, we have to define and calculate certain quantities. We are going to look into the susceptibility, which describes the response of the system under an applied field. To do so we need to introduce the following correlators, the density-density ("charge") and the spin-spin ("spin") correlation functions, defined as:

$$[\chi^{dd}](q,\tau) = \left\langle T_\tau \mathcal{N}(q;\tau)\mathcal{N}(-q,0)\right\rangle, \tag{4.1}$$

$$[\chi^{ij}](q,\tau) = \big\langle T_\tau S^i(q;\tau) S^j(-q,\tau)\big\rangle, \tag{4.2}$$

where the multi-orbital density and spin operators are:

$$\hat{\mathcal{N}}_{\mu\sigma}(q) = \frac{1}{\mathcal{V}}\sum_k c^\dagger_{k-q,\mu\sigma}(\tau) c_{k,\mu\sigma}(\tau), \tag{4.3}$$

$$\hat{S}^i_{\mu_1\mu_2}(q) = \frac{1}{2\mathcal{V}}\sum_k \big(c^\dagger_{k-q,\mu_1\uparrow}(\tau) c^\dagger_{k-q,\mu_1\downarrow}(\tau)\big)\underline{\underline{\sigma_i}}\begin{pmatrix} c_{k,\mu_2\uparrow}(\tau) \\ c_{k,\mu_2\downarrow}(\tau)\end{pmatrix}. \tag{4.4}$$

In the above expressions, $\mathcal{V}$ is a normalization constant, the index i corresponds to the direction of an external magnetic field and σ_i are the Pauli matrices. Here and throughout the whole chapter, the greek letters (μ,ν) denote orbital indices, while σ is the particle's spin and k its momentum. At this point it is useful to introduce a generalized correlation function as the following:

$$[\chi]^{\mu_1\sigma_1;\mu_2\sigma_2}_{\mu_3\sigma_3;\mu_4\sigma_4}(q,i\omega_n) = \frac{1}{\mathcal{V}}\bigg(\sum_k \big\langle T_\tau c^\dagger_{k-q,\mu_1\sigma_1}(\tau) c_{k,\mu_2\sigma_2}(\tau) c^\dagger_{k,\mu_3\sigma_3}(0) c_{k-q,\mu_4\sigma_4}(0)\big\rangle\bigg). \tag{4.5}$$

For the charge susceptibility there are four contributions arising from the different spin configurations:

$$\chi_c = \frac{1}{2}\bigg([\chi]^{\mu_1\uparrow;\mu_2\uparrow}_{\mu_3\uparrow;\mu_4\uparrow} + [\chi]^{\mu_1\uparrow;\mu_2\uparrow}_{\mu_3\downarrow;\mu_4\downarrow} + [\chi]^{\mu_1\downarrow;\mu_2\downarrow}_{\mu_3\uparrow;\mu_4\uparrow} + [\chi]^{\mu_1\downarrow;\mu_2\downarrow}_{\mu_3\downarrow;\mu_4\downarrow}\bigg). \tag{4.6}$$

The $\frac{1}{2}$ in the above expression is a convention and it appears in order for χ_c to reduce to its known form in the presence of SU(2) (rotational) symmetry. The system we want to study is two dimensional, since it can be described by a 2D iron plane, as explained in chapter 1. The electrons will, then, all be on that plane, with their spin pointing anywhere in three dimensions. We can described the spin direction simply by two orthogonal directions and we chose the longitudinal and the transverse one. We are interested in the normal paramagnetic state, so we expect all the spin-spin correlation functions to give the same result, due to symmetry. A factor of $\frac{1}{2}$ will appear for the same reason as for χ_c. For the longitudinal susceptibility we get:

$$[\chi^{zz}]^{\mu_1;\mu_2}_{\mu_3;\mu_4}(q;\tau) = \big\langle T_\tau S^z_{\mu_1;\mu_2}(q;\tau) S^z_{\mu_3;\mu_4}(-q;0)\big\rangle =$$

$$= \frac{1}{4\mathcal{V}}\sum_{kk'}\big\langle T_\tau\big(c^\dagger_{k-q,\mu_1\uparrow}(\tau)c_{k,\mu_2\uparrow}(\tau) - c^\dagger_{k-q,\mu_1\downarrow}(\tau)c_{k,\mu_2\downarrow}(\tau)\big)\cdot\big(c^\dagger_{k'+q,\mu_3\uparrow}c_{k',\mu_4\uparrow} - c^\dagger_{k'+q,\mu_3\downarrow}c_{k',\mu_4\downarrow}\big) =$$

$$= \frac{1}{2}\bigg([\chi]^{\mu_1\uparrow;\mu_2\uparrow}_{\mu_3\uparrow;\mu_4\uparrow} + [\chi]^{\mu_1\uparrow;\mu_2\uparrow}_{\mu_3\downarrow;\mu_4\downarrow} - [\chi]^{\mu_1\downarrow;\mu_2\downarrow}_{\mu_3\uparrow;\mu_4\uparrow} - [\chi]^{\mu_1\downarrow;\mu_2\downarrow}_{\mu_3\downarrow;\mu_4\downarrow}\bigg). \tag{4.7}$$

We also give the expression for the transverse susceptibility:

$$[\chi^{+-}]^{\mu_1;\mu_2}_{\mu_3;\mu_4}(q;\tau) = \big\langle T_\tau S^+_{\mu_1;\mu_2}(q;\tau) S^-_{\mu_3;\mu_4}(-q;0)\big\rangle =$$

$$= \big\langle T_\tau \frac{1}{\sqrt{2}}\big(S^x_{\mu_1;\mu_2} + iS^y_{\mu_3;\mu_4}\big)(q;\tau)\frac{1}{\sqrt{2}}\big(S^x_{\mu_1;\mu_2} - S^y_{\mu_3;\mu_4}(-q;0)\big)\big\rangle =$$

$$= \frac{1}{4}\bigg(\frac{1}{2\mathcal{V}}\sum_{kk'}\big\langle T_\tau c^\dagger_{k+q,\mu_1\uparrow}(\tau)c_{k,\mu_2\downarrow}(\tau)c^\dagger_{k'-q,\mu_3\downarrow}c_{k',\mu_4\uparrow}\big\rangle\bigg). \tag{4.8}$$

4.1.1 Bare susceptibility

We will first calculate the bare susceptibility, which means that we are going to neglect the interactions and assume a free electron gas. We start from the following formula:

$$\left[\chi^0\right]^{\mu_1;\mu_2}_{\mu_3;\mu_4}(q,\tau) = \frac{1}{\mathcal{V}} \sum_{\substack{k,k' \\ \sigma_1,\sigma_2,\sigma_3,\sigma_4}} \sum_{\substack{\mu_1,\mu_2, \\ \mu_3,\mu_4}} \left\langle T_\tau \left(c^\dagger_{k-q,\mu_1\sigma_1}(\tau) c_{k,\mu_2\sigma_2}(\tau) c^\dagger_{k'+q,\mu_3\sigma_3}(0) c_{k',\mu_4\sigma_4}(0) \right) \right\rangle_0. \tag{4.9}$$

In order to deal with such expressions we use Wick's theorem, according to which a higher-order Green's function, involving more than one particle, can be factorized into products of single-particle Green's functions [44]. The Matsubara Green's function is defined as:

$$\left[\mathcal{G}^0_{k\sigma}\right]_{\mu_1\mu_2}(\tau-\tau') = -\left\langle T_\tau c_{k,\mu_2\sigma}(\tau) c^\dagger_{k,\mu_1\sigma}(\tau') \right\rangle. \tag{4.10}$$

If we now make use of the theorem, take all possible pairings of products of single-particle Green's functions and carefully carry along the signs, arising from the operator commutations we end up with:

$$\left[\chi^0\right]^{\mu_1;\mu_2}_{\mu_3;\mu_4}(q,\tau) = -\frac{1}{\mathcal{V}} \sum_{k,\sigma_1,\sigma_2} \left[\mathcal{G}^0_{k,\sigma_2}\right]_{\mu_2;\mu_3}(\tau) \left[\mathcal{G}^0_{k-q,\sigma_1}\right]_{\mu_1;\mu_4}(-\tau), \tag{4.11}$$

where we already took into account spin-rotational symmetry and set $\sigma_1 = \sigma_4$, $\sigma_2 = \sigma_3$. The next step is to perform a Fourier transform and move to Matsubara frequency space, where the above expression takes the following form:

$$\left[\chi^0\right]^{\mu_1;\mu_2}_{\mu_3;\mu_4}(q,iq_n) = -\frac{1}{\beta\mathcal{V}} \sum_{ik_n,k,\sigma_1\sigma_2} \left[\mathcal{G}^0_{k,\sigma_2}\right]_{\mu_2;\mu_3}(ik_n) \left[\mathcal{G}^0_{k-q,\sigma_1}\right]_{\mu_1;\mu_4}(ik_n+iq_n). \tag{4.12}$$

The parameter $\beta = 1/kT$, with k being Boltzmann's constant and T the temperature, while ik_n is a fermionic frequency and iq_n a bosonic one. Performing now the Matsubara sum over the fermionic frequency ik_n and using $\left[\mathcal{G}^0_{k,\sigma}\right]_{\mu\mu'}(ik_n) = 1/\left(ik_n - E^{\mu\mu'}(k)\right)$, we obtain the final expression for the bare susceptibility:

$$[\chi_0]^{\mu_1;\mu_2}_{\mu_3;\mu_4}(q,\omega) = -\frac{1}{\mathcal{V}} \sum_{k,s,p} \alpha^{\mu_2}_s(k) \alpha^{\mu_3 *}_s(k) \alpha^{\mu_4}_p(k-q) \alpha^{\mu_1 *}_p(k-q) \frac{n_f(E_p(k-q)) - n_f(E_s(k))}{\omega + i\eta^+ + E_p(k-q) - E_s(k)}. \tag{4.13}$$

Here we have already performed the analytic continuation and gone from the imaginary bosonic Matsubara frequencies to the real ones by $iq_n \to \omega + i\eta^+$. With $n_f(E)$ we denote the Fermi distribution function $n_f(E) = 1/(e^{E/kT}+1)$ and $\mathcal{V}$ is the system size, while the α factors arise from the diagonalization of the Hamiltonian and are related to its eigenvectors. The relevant bare susceptibility diagram is illustrated in Fig.4.1.

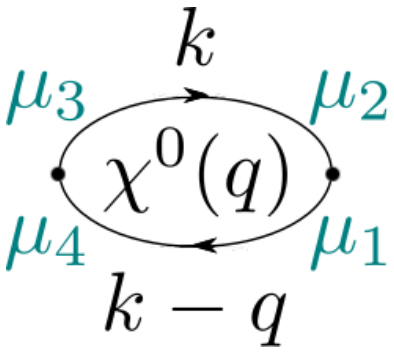

Figure 4.1: Bare susceptibility bubble

Thinking in the same spirit and using again Wick's theorem we can rewrite, for example, also the transverse susceptibility of Eq.(4.8), in order to use it in the following sections.

$$
\begin{aligned}
4[\chi_0^{+-}]^{\mu_1;\mu_2}_{\mu_3;\mu_4}(q;\tau) &= -\frac{1}{2\mathcal{V}}\sum_{kk'}\left\langle T_\tau c_{k',\mu_4\uparrow}c^\dagger_{k-q,\mu_1\uparrow}(\tau)c_{k,\mu_2\downarrow}(\tau)c^\dagger_{k'+q,\mu_3\downarrow}\right\rangle = \\
&= -\frac{1}{2\mathcal{V}}\sum_{kk'}\left\langle T_\tau c_{k',\mu_4\uparrow}c^\dagger_{k-q,\mu_1\uparrow}(\tau)\right\rangle\left\langle T_\tau c_{k,\mu_2\downarrow}(\tau)c^\dagger_{k'+q,\mu_3\downarrow}\right\rangle = \\
&= -\frac{1}{2\mathcal{V}}\sum_{k}\left\langle T_\tau c_{k-q,\mu_4\uparrow}(-\tau)c^\dagger_{k-q,\mu_1\uparrow}\right\rangle\left\langle T_\tau c_{k,\mu_2\downarrow}(\tau)c^\dagger_{k,\mu_3\downarrow}\right\rangle = \\
&= -\frac{1}{2\mathcal{V}}\sum_{k}\left[\mathcal{G}^0_{k-q\uparrow}\right]_{\mu_1;\mu_4}(-\tau)\left[\mathcal{G}^0_{k\downarrow}\right]_{\mu_3;\mu_2}(\tau)
\end{aligned}
\tag{4.14}
$$

As we mentioned in the beginning of the chapter, we will focus on the two band case and we remind ourselves of the Raghu model, already introduced in chapter 3. The Hamiltonian is:

$$
H = \sum_{k\sigma}\begin{pmatrix} d^\dagger_{x\sigma}(k) & d^\dagger_{y\sigma}(k)\end{pmatrix}\begin{pmatrix}\epsilon_x(k)-\mu & \epsilon_{xy}(k)\\ \epsilon_{xy}(k) & \epsilon_y(k)-\mu\end{pmatrix}\begin{pmatrix} d_{x\sigma}(k)\\ d_{y\sigma}(k)\end{pmatrix}, \tag{4.15}
$$

where:

$$
\begin{aligned}
\epsilon_x(k) &= -2t_1\cos k_x - 2t_2\cos k_y - 4t_3\cos k_x\cos k_y, \\
\epsilon_y(k) &= -2t_2\cos k_x - 2t_1\cos k_y - 4t_3\cos k_x\cos k_y, \\
\epsilon_{xy}(k) &= -4t_4\sin k_x\sin k_y,
\end{aligned}
\tag{4.16}
$$

with $t_1 = -1$, $t_2 = 1.3$ and $t_3 = t_4 = -0.85$.

In Fig.4.2a we plot the bare susceptibility at zero frequency on the whole Brillouin zone, and we see that the system is C4 symmetric and that there is a modulation of χ_0 across the zone. The highest values are located around the $X = (\pi, 0)$ and $Y = (0, \pi)$ points and naturally on their symmetric ones. In Fig.4.2b we plot χ_0 along the $\Gamma X M \Gamma$ path. We observe that at $X = (\pi, 0)$ there is indeed a susceptibility peak, already making obvious that ΓX is an important vector, reminding us of the nesting vectors analysis we made in chapter 1.

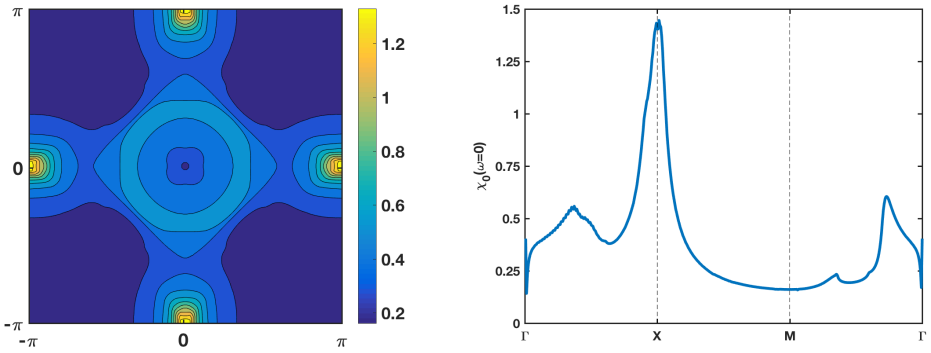

(a) (b)

Figure 4.2: Bare susceptibility for the Raghu model with $U = 2.5eV$ (a) on the whole Brillouin zone, (b) along the $\Gamma XM\Gamma$ path. We observe the distinct peak of the susceptibility on the X point. The same peak appears on the Y point, in agreement with the C4 symmetry of the system.

4.1.2 RPA susceptibility

In the previous section we calculated the bare susceptibility, by completely ignoring the electron-electron interactions. However, if we want to include those in our description the situation becomes very complicated, and we are unable to solve the problem. A way to tackle this issue is to use the random phase approximation (RPA) and instead of summing over infinite diagrams, keep only the bubble and ladder type ones. Using the equation of motion technique (for a derivation see Appendix C), we get the expression for the generalized RPA susceptibility:

$$[\chi^{RPA}]^{\mu_1\sigma_1;\mu_2\sigma_2}_{\mu_3\sigma_3;\mu_4\sigma_4}(q, i\omega_n) = [\chi^0]^{\mu_1\sigma_1;\mu_2\sigma_2}_{\mu_3\sigma_3;\mu_4\sigma_4}(q, i\omega_n) +$$

$$+[\chi^0]^{\mu_1\sigma_1;\mu_2\sigma_2}_{\nu_1\sigma_1;\nu_2\sigma_2}(q, i\omega_n)[\mathcal{V}]^{\mu_1\sigma_1;\mu_2\sigma_2}_{\nu_3\sigma_3;\nu_4\sigma_4}[\chi^{RPA}]^{\nu_3\sigma_3;\nu_4\sigma_4}_{\mu_3\sigma_3;\mu_4\sigma_4}(q, i\omega_n) \tag{4.17}$$

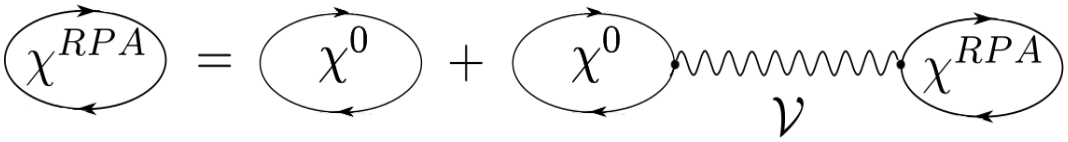

Figure 4.3: RPA susceptibility equation

The first step in order to solve this equation is to write down in a diagrammatic form all the different interaction lines that appear in our problem. We need to keep in mind the multi-orbital character of the system and make sure that, at the interaction vertices, momentum is conserved as well as spin, since the interactions do not include processes that can flip the spin projections of the electrons. The possible interaction lines connect either electrons with same spin projections or with opposite ones, and the various orbital combinations give rise to different lines, as it is more clearly shown in a diagrammatic form in Fig.4.4.

We now introduce an intuitive way of understanding the possible interaction lines that come in play. We can first split the general interaction vertex into three contributions, according to the spin structure, as $\mathcal{V} = \mathcal{V}_1 + \mathcal{V}_2 + \mathcal{V}_3$. So, as shown in Fig.4.4, $\mathcal{V}_1$ corresponds to scattering of equal spin, longitudinal spin fluctuations, $\mathcal{V}_2$ corresponds to scattering of opposite spin, longitudinal spin fluctuations and $\mathcal{V}_3$ corresponds to transverse spin fluctuations.

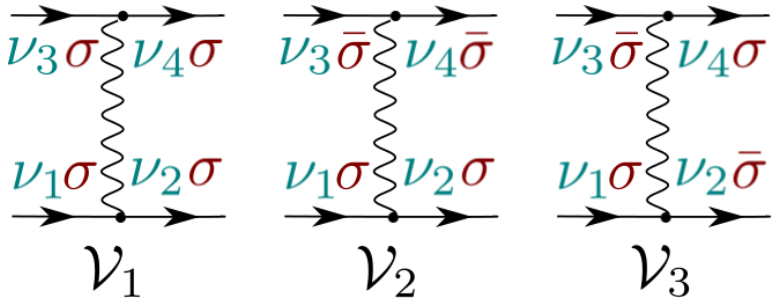

Figure 4.4: The three interaction channels related to the spin structure. The total interaction vertex is $\mathcal{V} = \mathcal{V}_1 + \mathcal{V}_2 + \mathcal{V}_3$.

The next step is to split each one of these three channels into the different contributions related to orbital structure. In order to do that, we first remind ourselves of the interaction Hamiltonian in the Hubbard model we have been using throughout this thesis.

$$\hat{H}_{int} = U \sum_m n_{m\uparrow} n_{m\downarrow} + U' \sum_{m \neq m'} n_{m\uparrow} n_{m'\downarrow} + (U' - J) \sum_{m<m',\sigma} n_{m\sigma} n_{m'\sigma} -$$
$$-J \sum_{m \neq m'} d^\dagger_{m\uparrow} d_{m\downarrow} d^\dagger_{m'\downarrow} d_{m'\uparrow} + J \sum_{m \neq m'} d^\dagger_{m\uparrow} d^\dagger_{m\downarrow} d_{m'\downarrow} d_{m'\uparrow} \tag{4.18}$$

Looking very carefully at the form of the interaction Hamiltonian, we make a splitting for the three interaction channels defined above, according to the orbital configurations. By looking at those diagrams, illustrated in Fig.4.5, and comparing with the interaction Hamiltonian, we get the expressions for all the terms appearing in each of the three interaction channels:

$$\left[\mathcal{V}_1\right]^{\mu\mu}_{\mu\mu} = 0, \quad \left[\mathcal{V}_1\right]^{\nu\nu}_{\mu\mu} = U' - J, \quad \left[\mathcal{V}_1\right]^{\mu\nu}_{\mu\nu} = 0, \quad \left[\mathcal{V}_1\right]^{\nu\mu}_{\mu\nu} = J - U'$$

$$\left[\mathcal{V}_2\right]^{\mu\mu}_{\mu\mu} = U, \quad \left[\mathcal{V}_2\right]^{\nu\nu}_{\mu\mu} = U', \quad \left[\mathcal{V}_2\right]^{\mu\nu}_{\mu\nu} = J', \quad \left[\mathcal{V}_2\right]^{\nu\mu}_{\mu\nu} = J$$

$$\left[\mathcal{V}_3\right]^{\mu\mu}_{\mu\mu} = -U, \quad \left[\mathcal{V}_3\right]^{\nu\nu}_{\mu\mu} = -J, \quad \left[\mathcal{V}_3\right]^{\mu\nu}_{\mu\nu} = -J', \quad \left[\mathcal{V}_3\right]^{\nu\mu}_{\mu\nu} = -U' \tag{4.19}$$

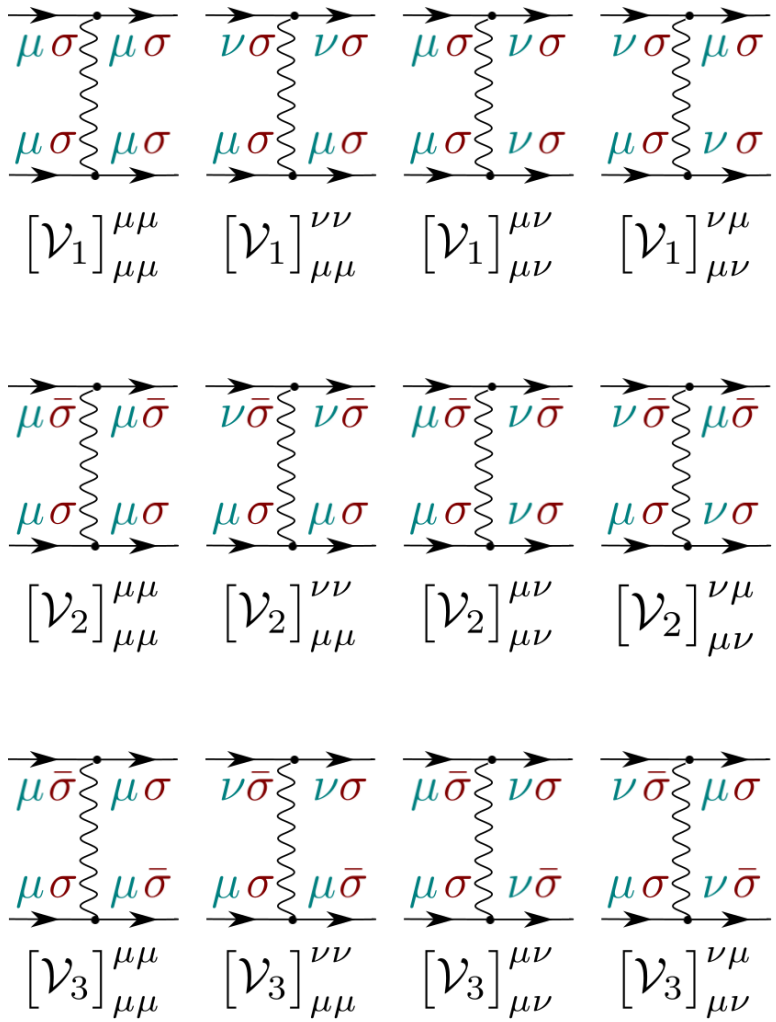

Figure 4.5: Each line corresponds to the orbital structure of the $1^{st}, 2^{nd}$ and 3^{rd} interaction channel respectively.

At this point and before we calculate the charge and spin susceptibilities, we can exploit the spin rotational symmetry the system exhibits in the paramagnetic state. It it easy to conclude that the only components of the bare susceptibility which are going to be non-zero, are the ones satisfying $\sigma_1 = \sigma_4$, $\sigma_2 = \sigma_3$. We will now show in detail how one can compute the charge susceptibility, and then the spin one can be derived following the same method. Replacing in the generalized RPA equation the interaction lines present in our model, as they were defined above, and picking only the terms which contribute to the charge susceptibility we arrive at:

$$\chi^c = \frac{1}{2}\left([\chi]^{\mu\uparrow;\mu\uparrow}_{\nu\uparrow;\nu\uparrow} + [\chi]^{\mu\uparrow;\mu\uparrow}_{\nu\downarrow;\nu\downarrow} + [\chi]^{\mu\downarrow;\mu\downarrow}_{\nu\uparrow;\nu\uparrow} + [\chi]^{\mu\downarrow;\mu\downarrow}_{\nu\downarrow;\nu\downarrow}\right) \tag{4.20}$$

$$\begin{aligned}
[\chi]^{\mu\uparrow;\mu\uparrow}_{\nu\uparrow;\nu\uparrow} = {} & [\chi^0]^{\mu\uparrow;\mu\uparrow}_{\nu\uparrow;\nu\uparrow} + [\chi^0]^{\mu\uparrow;\mu\uparrow}_{\nu\uparrow;\nu\uparrow}\left(- U[\chi]^{\nu\downarrow;\nu\downarrow}_{\nu\uparrow;\nu\uparrow} - U'[\chi]^{\mu\downarrow;\mu\downarrow}_{\nu\uparrow;\nu\uparrow} - (U'-J)[\chi]^{\mu\uparrow;\mu\uparrow}_{\nu\uparrow;\nu\uparrow}\right) + \\
& + [\chi^0]^{\mu\uparrow;\mu\uparrow}_{\mu\uparrow;\mu\uparrow}\left(- U[\chi]^{\mu\downarrow;\mu\downarrow}_{\nu\uparrow;\nu\uparrow} - U'[\chi]^{\nu\downarrow;\nu\downarrow}_{\nu\uparrow;\nu\uparrow} - (U'-J)[\chi]^{\nu\uparrow;\nu\uparrow}_{\nu\uparrow;\nu\uparrow}\right) + \\
& + [\chi^0]^{\mu\uparrow;\mu\uparrow}_{\mu\uparrow;\nu\uparrow}\left(- J[\chi]^{\nu\downarrow;\mu\downarrow}_{\nu\uparrow;\nu\uparrow} - J'[\chi]^{\mu\downarrow;\nu\downarrow}_{\nu\uparrow;\nu\uparrow} + (U'-J)[\chi]^{\nu\uparrow;\mu\uparrow}_{\nu\uparrow;\nu\uparrow}\right) + \\
& + [\chi^0]^{\mu\uparrow;\mu\uparrow}_{\nu\uparrow;\mu\uparrow}\left(- J[\chi]^{\mu\downarrow;\nu\downarrow}_{\nu\uparrow;\nu\uparrow} - J'[\chi]^{\nu\downarrow;\mu\downarrow}_{\nu\uparrow;\nu\uparrow} + (U'-J)[\chi]^{\mu\uparrow;\mu\uparrow}_{\nu\uparrow;\nu\uparrow}\right)
\end{aligned} \tag{4.21}$$

$$
\begin{aligned}
[\chi]^{\mu\uparrow;\mu\uparrow}_{\nu\downarrow;\nu\downarrow} = [\chi^0]^{\mu\uparrow;\mu\uparrow}_{\nu\downarrow;\nu\downarrow}\big(- U[\chi]^{\nu\downarrow;\nu\downarrow}_{\nu\downarrow;\nu\downarrow} - U'[\chi]^{\mu\downarrow;\mu\downarrow}_{\nu\downarrow;\nu\downarrow} - (U'-J)[\chi]^{\mu\uparrow;\mu\uparrow}_{\nu\downarrow;\nu\downarrow}\big) + \\
+[\chi^0]^{\mu\uparrow;\mu\uparrow}_{\mu\uparrow;\mu\uparrow}\big(- U[\chi]^{\mu\downarrow;\mu\downarrow}_{\nu\downarrow;\nu\downarrow} - U'[\chi]^{\nu\downarrow;\nu\downarrow}_{\nu\downarrow;\nu\downarrow} - (U'-J)[\chi]^{\nu\uparrow;\nu\uparrow}_{\nu\downarrow;\nu\downarrow}\big) + \\
+[\chi^0]^{\mu\uparrow;\mu\uparrow}_{\mu\uparrow;\nu\uparrow}\big(- J[\chi]^{\nu\downarrow;\mu\downarrow}_{\nu\downarrow;\nu\downarrow} - J'[\chi]^{\mu\downarrow;\nu\downarrow}_{\nu\downarrow;\nu\downarrow} + (U'-J)[\chi]^{\nu\uparrow;\mu\uparrow}_{\nu\downarrow;\nu\downarrow}\big) + \\
+[\chi^0]^{\mu\uparrow;\mu\uparrow}_{\nu\uparrow;\mu\uparrow}\big(- J[\chi]^{\mu\downarrow;\nu\downarrow}_{\nu\downarrow;\nu\downarrow} - J'[\chi]^{\nu\downarrow;\mu\downarrow}_{\nu\downarrow;\nu\downarrow} + (U'-J)[\chi]^{\mu\uparrow;\mu\uparrow}_{\nu\downarrow;\nu\downarrow}\big)
\end{aligned}
\tag{4.22}
$$

$$
\begin{aligned}
[\chi]^{\mu\downarrow;\mu\downarrow}_{\nu\uparrow;\nu\uparrow} = [\chi^0]^{\mu\downarrow;\mu\downarrow}_{\nu\downarrow;\nu\downarrow}\big(- U[\chi]^{\nu\uparrow;\nu\uparrow}_{\nu\uparrow;\nu\uparrow} - U'[\chi]^{\mu\uparrow;\mu\uparrow}_{\nu\uparrow;\nu\uparrow} - (U'-J)[\chi]^{\mu\downarrow;\mu\downarrow}_{\nu\uparrow;\nu\uparrow}\big) + \\
+[\chi^0]^{\mu\downarrow;\mu\downarrow}_{\mu\downarrow;\mu\downarrow}\big(- U[\chi]^{\mu\uparrow;\mu\uparrow}_{\nu\uparrow;\nu\uparrow} - U'[\chi]^{\nu\uparrow;\nu\uparrow}_{\nu\uparrow;\nu\uparrow} - (U'-J)[\chi]^{\nu\downarrow;\nu\downarrow}_{\nu\uparrow;\nu\uparrow}\big) + \\
+[\chi^0]^{\mu\downarrow;\mu\downarrow}_{\mu\downarrow;\nu\downarrow}\big(- J[\chi]^{\nu\uparrow;\mu\uparrow}_{\nu\uparrow;\nu\uparrow} - J'[\chi]^{\mu\uparrow;\nu\uparrow}_{\nu\uparrow;\nu\uparrow} + (U'-J)[\chi]^{\nu\downarrow;\mu\downarrow}_{\nu\uparrow;\nu\uparrow}\big) + \\
+[\chi^0]^{\mu\downarrow;\mu\downarrow}_{\nu\downarrow;\mu\downarrow}\big(- J[\chi]^{\mu\uparrow;\nu\uparrow}_{\nu\uparrow;\nu\uparrow} - J'[\chi]^{\nu\uparrow;\mu\uparrow}_{\nu\uparrow;\nu\uparrow} + (U'-J)[\chi]^{\mu\downarrow;\mu\downarrow}_{\nu\uparrow;\nu\uparrow}\big)
\end{aligned}
\tag{4.23}
$$

$$
\begin{aligned}
[\chi]^{\mu\downarrow;\mu\downarrow}_{\nu\downarrow;\nu\downarrow} = [\chi^0]^{\mu\downarrow;\mu\downarrow}_{\nu\downarrow;\nu\downarrow} + [\chi^0]^{\mu\downarrow;\mu\downarrow}_{\nu\downarrow;\nu\downarrow}\big(- U[\chi]^{\nu\uparrow;\nu\uparrow}_{\nu\uparrow;\nu\uparrow} - U'[\chi]^{\mu\uparrow;\mu\uparrow}_{\nu\uparrow;\nu\uparrow} - (U'-J)[\chi]^{\mu\downarrow;\mu\downarrow}_{\nu\uparrow;\nu\uparrow}\big) + \\
+[\chi^0]^{\mu\downarrow;\mu\downarrow}_{\mu\downarrow;\mu\downarrow}\big(- U[\chi]^{\mu\uparrow;\mu\uparrow}_{\nu\downarrow;\nu\downarrow} - U'[\chi]^{\nu\uparrow;\nu\uparrow}_{\nu\downarrow;\nu\downarrow} - (U'-J)[\chi]^{\nu\downarrow;\nu\downarrow}_{\nu\downarrow;\nu\downarrow}\big) + \\
+[\chi^0]^{\mu\downarrow;\mu\downarrow}_{\mu\downarrow;\nu\downarrow}\big(- J[\chi]^{\nu\uparrow;\mu\uparrow}_{\nu\downarrow;\nu\downarrow} - J'[\chi]^{\mu\uparrow;\nu\uparrow}_{\nu\downarrow;\nu\downarrow} + (U'-J)[\chi]^{\nu\downarrow;\mu\downarrow}_{\nu\downarrow;\nu\downarrow}\big) + \\
+[\chi^0]^{\mu\downarrow;\mu\downarrow}_{\nu\downarrow;\mu\downarrow}\big(- J[\chi]^{\mu\uparrow;\nu\uparrow}_{\nu\downarrow;\nu\downarrow} - J'[\chi]^{\nu\uparrow;\mu\uparrow}_{\nu\downarrow;\nu\downarrow} + (U'-J)[\chi]^{\mu\downarrow;\mu\downarrow}_{\nu\downarrow;\nu\downarrow}\big)
\end{aligned}
\tag{4.24}
$$

Now we can make use of the fact that the bare susceptibility bubble does not depend on the spin configuration, as is obvious from the expression 4.13. Thus, we can sum the previous expressions and group them to get:

$$
\begin{aligned}
\chi^c = \chi^0 + [\chi^0]^{\mu\mu}_{\nu\nu}\Big[- U\big([\chi]^{\nu\downarrow;\nu\downarrow}_{\nu\uparrow;\nu\uparrow} + [\chi]^{\nu\uparrow;\nu\uparrow}_{\nu\uparrow;\nu\uparrow} + [\chi]^{\nu\downarrow;\nu\downarrow}_{\nu\downarrow;\nu\downarrow} + [\chi]^{\nu\uparrow;\nu\uparrow}_{\nu\downarrow;\nu\downarrow}\big) - \\
-U'\big([\chi]^{\mu\downarrow;\mu\downarrow}_{\nu\uparrow;\nu\uparrow} + [\chi]^{\mu\uparrow;\mu\uparrow}_{\nu\uparrow;\nu\uparrow} + [\chi]^{\mu\downarrow;\mu\downarrow}_{\nu\downarrow;\nu\downarrow} + [\chi]^{\mu\uparrow;\mu\uparrow}_{\nu\downarrow;\nu\downarrow}\big) - (U'-J)\big([\chi]^{\mu\downarrow;\mu\downarrow}_{\nu\uparrow;\nu\uparrow} + [\chi]^{\mu\uparrow;\mu\uparrow}_{\nu\uparrow;\nu\uparrow} + [\chi]^{\mu\downarrow;\mu\downarrow}_{\nu\downarrow;\nu\downarrow} + [\chi]^{\mu\uparrow;\mu\uparrow}_{\nu\downarrow;\nu\downarrow}\big)\Big] + \\
+[\chi^0]^{\mu\mu}_{\mu\mu}\Big[- U\big([\chi]^{\mu\downarrow;\mu\downarrow}_{\nu\uparrow;\nu\uparrow} + [\chi]^{\mu\uparrow;\mu\uparrow}_{\nu\uparrow;\nu\uparrow} + [\chi]^{\mu\downarrow;\mu\downarrow}_{\nu\downarrow;\nu\downarrow} + [\chi]^{\mu\uparrow;\mu\uparrow}_{\nu\downarrow;\nu\downarrow}\big) - \\
-U'\big([\chi]^{\nu\downarrow;\nu\downarrow}_{\nu\uparrow;\nu\uparrow} + [\chi]^{\nu\uparrow;\nu\uparrow}_{\nu\uparrow;\nu\uparrow} + [\chi]^{\nu\downarrow;\nu\downarrow}_{\nu\downarrow;\nu\downarrow} + [\chi]^{\nu\uparrow;\nu\uparrow}_{\nu\downarrow;\nu\downarrow}\big) - (U'-J)\big([\chi]^{\nu\downarrow;\nu\downarrow}_{\nu\uparrow;\nu\uparrow} + [\chi]^{\nu\uparrow;\nu\uparrow}_{\nu\uparrow;\nu\uparrow} + [\chi]^{\nu\downarrow;\nu\downarrow}_{\nu\downarrow;\nu\downarrow} + [\chi]^{\nu\uparrow;\nu\uparrow}_{\nu\downarrow;\nu\downarrow}\big)\Big] + \\
+[\chi^0]^{\mu\mu}_{\mu\nu}\Big[- J\big([\chi]^{\nu\downarrow;\mu\downarrow}_{\nu\uparrow;\nu\uparrow} + [\chi]^{\nu\uparrow;\mu\uparrow}_{\nu\uparrow;\nu\uparrow} + [\chi]^{\nu\downarrow;\mu\downarrow}_{\nu\downarrow;\nu\downarrow} + [\chi]^{\nu\uparrow;\mu\uparrow}_{\nu\downarrow;\nu\downarrow}\big) - \\
-J'\big([\chi]^{\mu\downarrow;\nu\downarrow}_{\nu\uparrow;\nu\uparrow} + [\chi]^{\mu\uparrow;\nu\uparrow}_{\nu\uparrow;\nu\uparrow} + [\chi]^{\mu\downarrow;\nu\downarrow}_{\nu\downarrow;\nu\downarrow} + [\chi]^{\mu\uparrow;\nu\uparrow}_{\nu\downarrow;\nu\downarrow}\big) + (U'-J)\big([\chi]^{\nu\downarrow;\mu\downarrow}_{\nu\uparrow;\nu\uparrow} + [\chi]^{\nu\uparrow;\mu\uparrow}_{\nu\uparrow;\nu\uparrow} + [\chi]^{\nu\downarrow;\mu\downarrow}_{\nu\downarrow;\nu\downarrow} + [\chi]^{\nu\uparrow;\mu\uparrow}_{\nu\downarrow;\nu\downarrow}\big)\Big] + \\
+[\chi^0]^{\mu\mu}_{\nu\mu}\Big[- J\big([\chi]^{\mu\downarrow;\nu\downarrow}_{\nu\uparrow;\nu\uparrow} + [\chi]^{\mu\uparrow;\nu\uparrow}_{\nu\uparrow;\nu\uparrow} + [\chi]^{\mu\downarrow;\nu\downarrow}_{\nu\downarrow;\nu\downarrow} + [\chi]^{\mu\uparrow;\nu\uparrow}_{\nu\downarrow;\nu\downarrow}\big) - \\
-J'\big([\chi]^{\nu\downarrow;\mu\downarrow}_{\nu\uparrow;\nu\uparrow} + [\chi]^{\nu\uparrow;\mu\uparrow}_{\nu\uparrow;\nu\uparrow} + [\chi]^{\nu\downarrow;\mu\downarrow}_{\nu\downarrow;\nu\downarrow} + [\chi]^{\nu\uparrow;\mu\uparrow}_{\nu\downarrow;\nu\downarrow}\big) + (U'-J)\big([\chi]^{\mu\downarrow;\nu\downarrow}_{\nu\uparrow;\nu\uparrow} + [\chi]^{\mu\uparrow;\nu\uparrow}_{\nu\uparrow;\nu\uparrow} + [\chi]^{\mu\downarrow;\nu\downarrow}_{\nu\downarrow;\nu\downarrow} + [\chi]^{\mu\uparrow;\nu\uparrow}_{\nu\downarrow;\nu\downarrow}\big)\Big]
\end{aligned}
\tag{4.25}
$$

From this equation we can now identify the elements of the charge vertex as:

$$
[\mathcal{V}]^{\nu\nu}_{\nu\nu} = -U, \quad [\mathcal{V}]^{\nu\nu}_{\mu\mu} = -2U' + J, \quad [\mathcal{V}]^{\mu\nu}_{\nu\mu} = -2J + U', \quad [\mathcal{V}]^{\mu\nu}_{\mu\nu} = -J', \tag{4.26}
$$

and in matrix form we write:

$$\mathcal{V}^C = -\begin{pmatrix} U & 0 & 0 & 2U'-J \\ 0 & J' & 2J-U' & 0 \\ 0 & 2J-U' & J' & 0 \\ 2U'-J & 0 & 0 & U \end{pmatrix}. \tag{4.27}$$

In complete analogy, and keeping in mind that in the normal paramagnetic state all spin-spin correlation functions are equal ($\langle S^z S^z \rangle = \langle S^x S^x \rangle = \langle S^y S^y \rangle$), we get for the spin vertex:

$$\mathcal{V}^S = \begin{pmatrix} U & 0 & 0 & J \\ 0 & J' & U' & 0 \\ 0 & U' & J' & 0 \\ J & 0 & 0 & U \end{pmatrix}. \tag{4.28}$$

We remind ourselves that the system exhibits spin rotational invariance, and if we make use of the relation $\underline{\underline{\sigma_x^2}} = \underline{\underline{\sigma_y^2}} = \underline{\underline{\sigma_z^2}}$ we will end up with the condition $\chi^{zz} = 2\chi^{+-}$. As we already mentioned in chapter 3, the so-called orbital rotational symmetry imposes the conditions $J' = J$ and $U = U' + 2J$ [50]. Hence, we have now reduced the interaction parameters from four to two (U, J).

Moving on to the practical part, we would like to compute the susceptibility and it becomes a lot less costly to do so, if we write χ_{RPA} (we now take a general case) in matrix form:

$$\underline{\underline{\chi_{RPA}}} = \underline{\underline{\chi_0}} + \underline{\underline{\chi_0}} \cdot \underline{\underline{\mathcal{V}}} \cdot \underline{\underline{\chi_{RPA}}}, \tag{4.29}$$

where, for example, in the case of a two orbital model:

$$\chi_0 = \begin{pmatrix} [\chi_0]_{11}^{11} & [\chi_0]_{12}^{11} & [\chi_0]_{21}^{11} & [\chi_0]_{22}^{11} \\ [\chi_0]_{11}^{12} & [\chi_0]_{12}^{12} & [\chi_0]_{21}^{12} & [\chi_0]_{22}^{12} \\ [\chi_0]_{11}^{21} & [\chi_0]_{12}^{21} & [\chi_0]_{21}^{21} & [\chi_0]_{22}^{21} \\ [\chi_0]_{11}^{22} & [\chi_0]_{12}^{22} & [\chi_0]_{21}^{22} & [\chi_0]_{22}^{22} \end{pmatrix}. \tag{4.30}$$

The bare bubble as mentioned earlier is given by:

$$[\chi_0]_{\mu_3;\mu_4}^{\mu_1;\mu_2}(q,\omega) = -\frac{1}{\mathcal{V}} \sum_{k,s,p} \alpha_s^{\mu_2}(k)\alpha_s^{\mu_3 *}(k)\alpha_p^{\mu_4}(k-q)\alpha_p^{\mu_1 *}(k-q) \frac{n_f(E_p(k-q)) - n_f(E_s(k))}{\omega + i\eta^+ + E_p(k-q) - E_s(k)}. \tag{4.31}$$

Now we can solve the RPA equation, simply by using matrix inversion, a computationally easy process.

$$(\underline{\underline{1}} - \underline{\underline{\chi_0}} \cdot \underline{\underline{\mathcal{V}}}) \cdot \underline{\underline{\chi_{RPA}}} = \underline{\underline{\chi_0}} \Rightarrow \underline{\underline{\chi_{RPA}}} = \underline{\underline{\chi_0}} \cdot (\underline{\underline{1}} - \underline{\underline{\chi_0}} \cdot \underline{\underline{\mathcal{V}}})^{-1} \tag{4.32}$$

4.1.3 Magnetic transition

We would like to find out what is the critical interaction strength for entering the magnetic phase in the Raghu model. This information will then guide us towards the appropriate choice for the interaction strength according to the state we want to study. Both for the normal and the nematic state, we should use values lower than U_c, but for the nematic case the chosen U should be very close to U_c, according to the analysis we made earlier on the proximity of the nematic phase to the magnetic one. The transition happens when spin susceptibility diverges at a particular point in momentum space. From the bare susceptibility analysis, we saw that at $X = (\pi, 0)$ there was a distinct peak and this motivates us to look for the divergence at that point. We would like, first, to explore the effect of Hund's coupling on the critical interaction, as a test for the validity of our results. We expect that U_c for the magnetic transition will be smaller in the presence of a non-zero Hund's coupling, because J favors the spin alignment, according to Hund's rule. Thus, the magnetic ordering should appear at a lower Coulomb interaction strength.

We plot in Fig.4.6a the RPA spin susceptibility at $X = (\pi, 0)$ as a function of interaction U, for Hund's coupling $J = 0$. We find that the critical value for the magnetic transition is $U_c \simeq 3.69eV$. In Fig.4.6b, $\chi_s^{RPA}(\omega = 0)$ is illustrated along the $\Gamma X M \Gamma$ path of the Brillouin zone, for $U = 3.69eV$. We observe that the divergence at the X point is present. Next, we add a non-zero Hund's coupling and we chose the value we have been using in chapter 3 as well, $J = U/4$. To confirm our expectation for the result, we plot in Fig.4.7a the RPA spin susceptibility at X versus the interaction U. The critical value is indeed smaller than in the $J = 0$ case, $U_c \simeq 3.005eV$. In addition, to give the complete picture we plot in Fig.4.7b the spin susceptibility on the $\Gamma X M \Gamma$ path and identify the divergence at the X point.

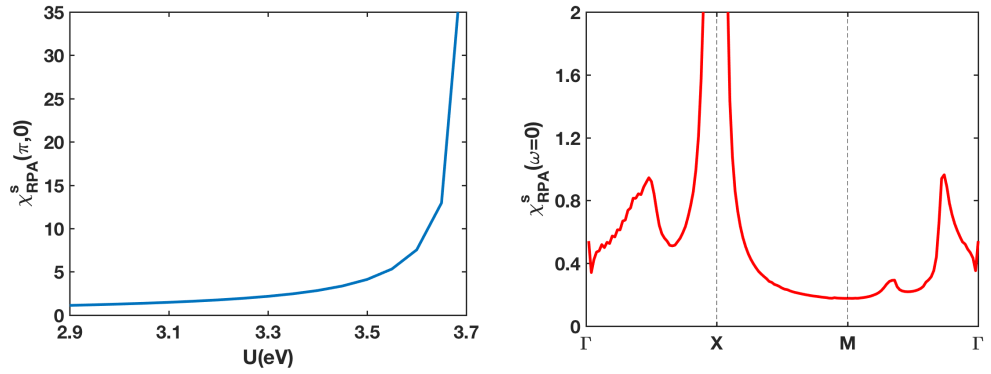

(a) (b)

Figure 4.6: RPA spin susceptibility for $J = 0$ (a) at the X point as a function of U and (b) along the $\Gamma X M \Gamma$ path for $U = 3.69eV \simeq U_c$, where we identify the divergence at the X point.

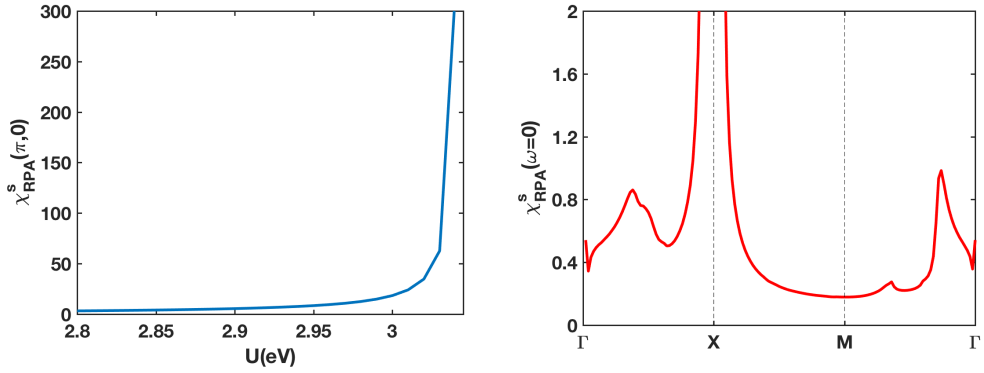

(a) (b)

Figure 4.7: RPA spin susceptibility for $J = U/4$ (a) at the X point as a function of U and (b) along the $\Gamma XM\Gamma$ path for $U = 3.005eV \simeq U_c$, where again we can see the divergence at the X point.

4.2 Self energy calculation

In the short Fermi liquid theory introduction we gave in chapter 2, we showed that in order to calculate the quasiparticle weights of a system, the calculation of the self-energy is necessary. The self-energy is related to the correction of a particle's energy due to its interactions with the system it belongs to. The relevant diagram is drawn in Fig.4.8 and the formula in orbital space will then be the one of equation 4.33.

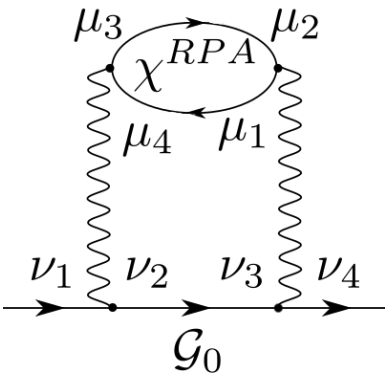

Figure 4.8: Self energy diagram

$$\Sigma_{\nu_1\nu_4}(k, i\omega_n) = \sum_{\nu_2\nu_3} \sum_{\mu_1\mu_2\mu_3\mu_4} \sum_{q, iq_n} [\mathcal{V}]^{\nu_1\nu_2}_{\mu_4\mu_3} [\chi_{RPA}]^{\mu_1\mu_2}_{\mu_3\mu_4}(q, iq_n) [\mathcal{V}]^{\mu_2\mu_1}_{\nu_3\nu_4} \mathcal{G}^0_{\nu_2\nu_3}(k+q, i\omega_n - iq_n) \tag{4.33}$$

The crucial point now is to explore this diagram and explicitly write down all the possible orbital and spin configurations that exist. We make use of the three interaction vertices we defined above as $\mathcal{V}_1, \mathcal{V}_2, \mathcal{V}_3$, and we keep in mind that the incoming and outgoing spin of the whole diagram should remain unchanged. Moreover, due to spin rotational symmetry, the lowest propagator $\mathcal{G}^0$ will carry only one spin index. We see that between the various combinations which come out, only four of them are non-zero as illustrated in the following graph.

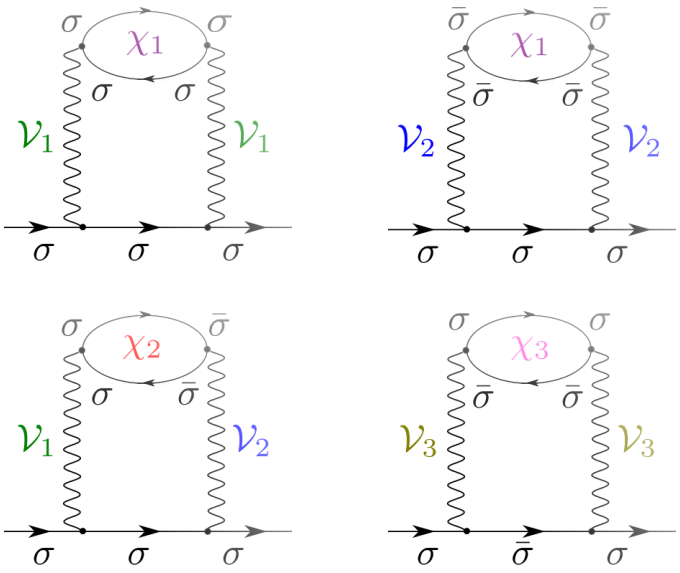

Figure 4.9: Interaction vertex

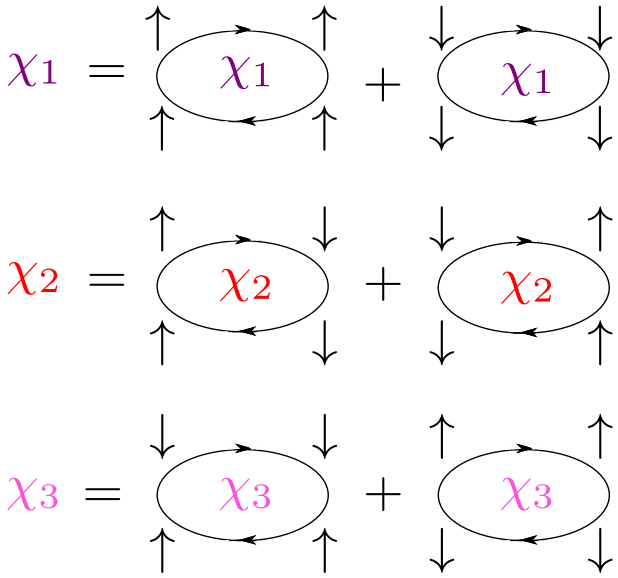

Figure 4.10: The 3 types of susceptibility

Next we would like to give a proper definition for the susceptibilities χ_1, χ_2, χ_3 which came out of our derivation, and we look at their diagrams in Fig.4.10. We notice that they are related to the charge and spin susceptibilities, which we calculated above, through linear combinations:

$$\begin{aligned} \chi_1 &= \chi^C + \tfrac{1}{3}\chi^S, \\ \chi_2 &= \chi^C - \tfrac{1}{3}\chi^S, \\ \chi_3 &= \tfrac{2}{3}\chi^S, \end{aligned} \tag{4.34}$$

where the charge and spin susceptibility diagrams are:

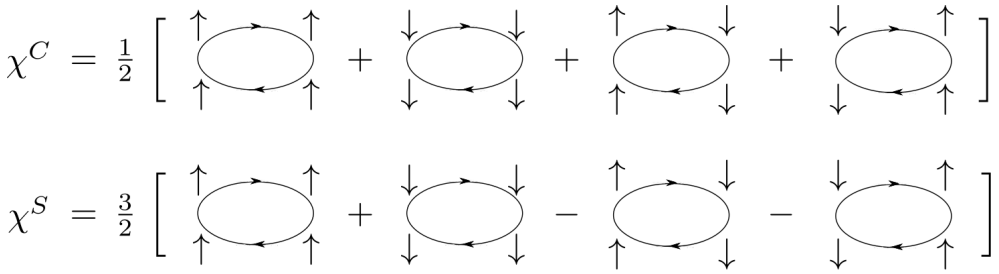

Figure 4.11: Charge and spin susceptibility

We have made use of the spin rotational symmetry and we wrote down χ^S as three times the χ^{zz} component. The expression for χ_3, though, comes out instead using the transverse spin susceptibility, in the form it was defined in Eq.(4.14). As we explained earlier, the transverse and longitudinal susceptibilities are related through $\chi^{zz} = 2\chi^{+-}$, so $\chi^S = 3\chi^{zz} = 6\chi^{+-}$. From Eq.(4.14) we see that $\chi_3 = 4\chi^{+-} = \frac{4}{6}\chi_S = \frac{2}{3}\chi_S$.

What we want to eventually calculate using this method is the quasiparticle weights. In chapter 2 we gave a short analysis on Fermi liquid theory and we showed that the quasiparticle weight formula is:

$$Z^{-1}_{\nu_1\nu_4} = 1 - \frac{\partial}{\partial\omega} Re\Sigma_{\nu_1\nu_4}(k_F,\omega)\big|_{\omega=0}. \tag{4.35}$$

For now and in order to speed up the process it is more useful to calculate directly the derivative rather than the self-energy itself:

$$\left(\frac{\partial\Sigma_{\nu_1\nu_4}(k_F,i\omega_n)}{\partial(i\omega_n)}\right)_{\omega_n=0} =$$

$$\sum_{\nu_2\nu_3}\sum_{\mu_1\mu_2\mu_3\mu_4}\sum_{q,iq_n}[\mathcal{V}]^{\nu_1\nu_2}_{\mu_4\mu_3}[\chi_{RPA}]^{\mu_1\mu_2}_{\mu_3\mu_4}(q,iq_n)[\mathcal{V}]^{\mu_2\mu_1}_{\nu_3\nu_4}\frac{\partial}{\partial(i\omega_n)}\big(\mathcal{G}^0_{\nu_2\nu_3}(k_F+q,i\omega_n+iq_n)\big)\big|_{\omega_n=0}. \tag{4.36}$$

The Green's function is given by:

$$\mathcal{G}^0_{\nu_2\nu_3}(k_f+q,i\omega_n+iq_n) = \sum_s \frac{\alpha_s^{\nu_2*}(k_f+q)\alpha_s^{\nu_3}(k_f+q)}{i\omega_n+iq_n-E^s(k_f+q)}. \tag{4.37}$$

Finally, the quantity we want to calculate will be:

$$\left(\frac{\partial\Sigma_{\nu_1\nu_4}(k_F,i\omega_n)}{\partial(i\omega_n)}\right)_{\omega_n=0} =$$
$$\sum_{\nu_2\nu_3}\sum_{\mu_1\mu_2\mu_3\mu_4}\sum_{q,iq_n}[\mathcal{V}]^{\nu_1\nu_2}_{\mu_4\mu_3}[\chi_{RPA}]^{\mu_1\mu_2}_{\mu_3\mu_4}(q,iq_n)[\mathcal{V}]^{\mu_2\mu_1}_{\nu_3\nu_4}\sum_s\frac{\alpha_s^{\nu_2*}(k_f+q)\alpha_s^{\nu_3}(k_f+q)}{(iq_n-E^s(k_f+q))^2} \tag{4.38}$$

Each point of the Fermi surface is related to a band crossing the Fermi level in the band-structure, and this band is unique for each point. Since the self-energy is an object which carries one momentum index, we understand that for a momentum $k = k_F$ it will be diagonal in band space (and consequently its derivative as well). Thus, we transform from orbital to band space, through the expression:

$$\left(\frac{\partial\Sigma_m(k_F, i\omega_n)}{\partial(i\omega_n)}\right)_{\omega_n=0} = \sum_{\nu_1\nu_4} \alpha_m^{\nu_1}(k_F)\left(\frac{\partial\Sigma_{\nu_1\nu_4}(k_F, i\omega_n)}{\partial(i\omega_n)}\right)_{\omega_n=0} \alpha_m^{\nu_4}(k_F) \tag{4.39}$$

4.3 Quasiparticle weights

We are now ready to implement all the above and calculate the quasiparticle weights for the Raghu model. We must be very careful, though, when identifying those numbers. After evaluating numerically the derivative of the self-energy, we obtain two Z-factors for each momentum point. However, we have explicitly stated that this method is only valid for energies close to the Fermi level, hence only one of those Z-factors is relevant. It is the one related to the band which is crossing the Fermi energy. It is obvious that the calculation of the quasiparticle weights is physically valid only on the Fermi surface (FS) momentum points.

When we attempt to implement numerically the expression 4.38 we come across a complication. Performing the summation over the bosonic frequency iq_n appearing in the denominator of the Green's function derivative, we obtain unphysical results. That is because for certain combinations of frequencies and energies the denominator becomes zero (or very close to zero). We overcome this issue by adding to the frequencies a small positive parameter η, which ensures that the system does not come across a divergence. In order to estimate the value we should ascribe to to η, we make the following check. We plot in Fig.4.12 the quasiparticle weight at a Fermi surface point as a function of η, for different system sizes N and we find that, after a point, Z converges. We also show the temperature we are using, to keep track of the relevant energy scales. The saturated values of Z for a varying N seem to be very close to each other, with a discrepancy of the order of 10^{-3}. Therefore, in order to speed up the process and lower the computational cost, we choose to use a 60x60 grid, with $\eta = 0.06eV$, which is larger than the temperature, but still of the same order. In the following calculations of this chapter we will be using those parameters and we will be summing over 51 Matsubara frequencies, which we found to be enough to give a converged result.

In chapter 3, we plotted in Fig.3.4 the band-structure of the Raghu model and we saw that the system around the Γ and M points exhibits hole pockets on the FS, while around the X and Y points, electron pockets. We will start by looking at the central hole pocket, located around the Γ point. In the left part of Fig.4.13a we illustrate eight points around this FS sheet and in Fig.4.13b we show the relevant calculated quasiparticle weights for each of those points and for different values of the interaction strength. The main trend is that with increasing U the system becomes gradually more and more correlated. We remind ourselves that the magnetic transition takes place at $U_c \simeq 3.005eV$, so the results for $U = 4eV$ are not meaningful, and we observe that indeed for that value at some points the Z-factors get very suppressed.

Moving on, we take nine points on the other FS pockets, the ones around X, M and Y. We show which are those points in the right part of Fig.4.13a and next in Fig.4.13c the relevant quasiparticle weights are illustrated. We observe, again, the

gradual suppression of the Z-factors upon tuning up the interactions. Moreover, we can see more clearly now the unphysical results ($Z > 1$) obtained for $U = 4eV$, where the system has undergone the magnetic phase transition.

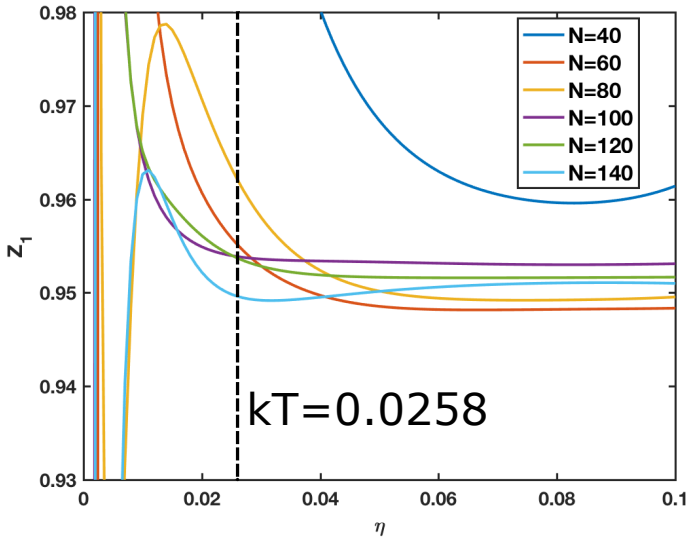

Figure 4.12: Quasiparticle weight on a FS point with varying the small parameter η as well as the grid size NxN. We see the saturation of Z after a critical η and we choose for our calculations to use $N = 60$ and $\eta = 0.06eV$. The relevant time scale is also illustrated.

Apart from the suppression of the quasiparticle weights with increasing interaction strength, a very important piece of information to extract from those graphs, is the confirmation of the C4 symmetry. Indeed, the Z-factors for the k-points on the FS connected through a C4 (so 90^o) rotation, are equal. On top of that, we see from Fig.4.13c that there is reflection symmetry as well. Upon reflection with respect to the x and y axis, the results then should be the same and we can see that from the comparison of Z_{k1} and Z_{k3}, as well as Z_{k7} and Z_{k9}. We are not going to comment on the exact numbers obtained, because as we mentioned in the beginning of this chapter, we are making a qualitative study, using the simplified two orbital model. The important things to keep from those results are (1) the evident suppression of Z with increasing U, approaching the magnetic transition and (2) the satisfaction of the system's symmetries.

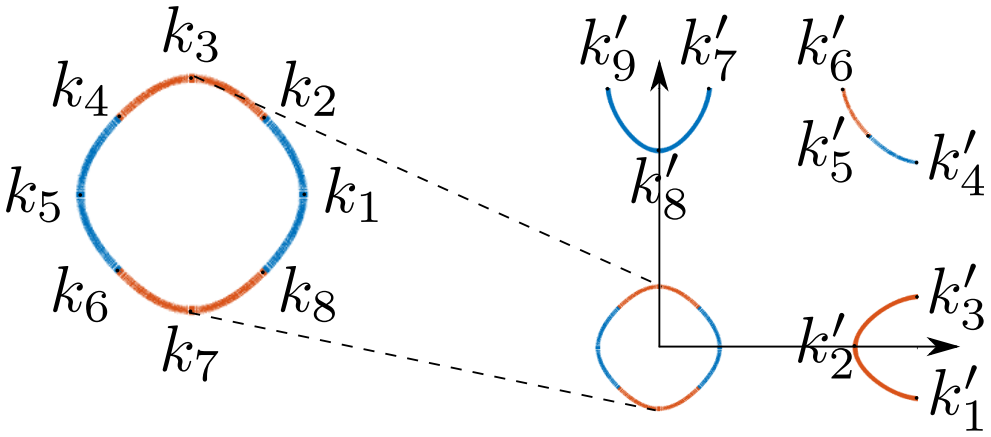

(a)

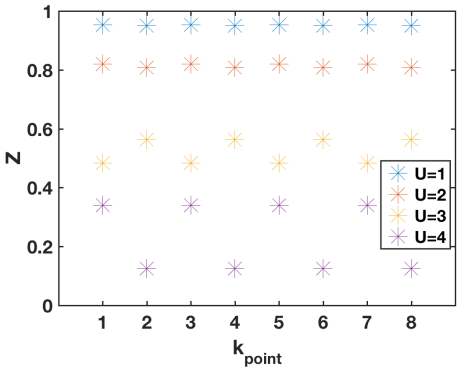

(b)

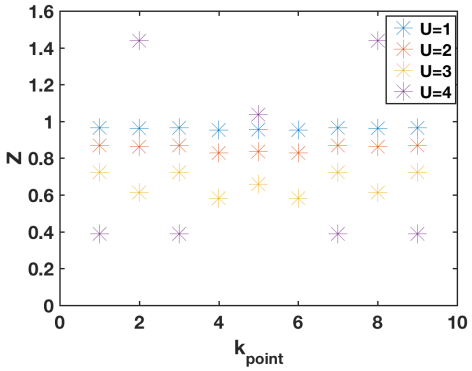

(c)

Figure 4.13: (a) Left part: eight points on the central pocket of the FS, around the $\Gamma = (0,0)$ point. Right part: nine points on the pockets of the FS, located around the $X = (\pi, 0), M = (\pi, \pi), Y = (0, \pi)$ points. (b) The quasiparticle weights on each of the eight points of (a)-left part, for interaction strength $U = 1, 2, 3, 4eV$. (c) Same as (b) for the nine points of (a)-right part. There is suppression of the Z-factors with increasing U and for $U = 4eV$, which is larger than the magnetic transition critical value, unphysical values are obtained (In (c) some of the unphysical data points for $U = 4eV$ do not appear in the plot, because they are larger than the axis limit). The system's $C4$ and reflection symmetries are also evident.

4.4 Nematic state

Already from chapter 2 we stated that we are interested in the nematic phase and specifically, we are motivated by experiments carried out in FeSe. In chapter 3, while studying the slave spin method, we devoted a section on nematicity. Our goal was to investigate whether, by adding a small splitting in the d_{xz}, d_{yz} energies, we can obtain a large difference in their calculated quasiparticle weights. However, we were unable to reproduce this tendency, we found that the Z-factor discrepancy was indeed present, but significantly smaller than the anticipated one. We will now address this problem within the self-energy calculation technique. We keep in mind that here we are using a two orbital model, which is not the appropriate one for the FeSC description. Nevertheless, if we manage to reproduce the tendency proposed in [39], we will be confident to proceed to the complicated five band model calculation and hopefully achieve to reproduce those findings quantitatively as well.

Since we are using this simplified model, we will include nematicity in our Hamiltonian through the simplest s-wave form, introduced in chapter 3. We are aiming to a qualitative result, so incorporating the complications of a more appropriate s+d-wave, would be at this point unnecessary. We remind the reader that the new term in the Hamiltonian will be $H_o = \delta_o(n_{xz} - n_{yz})$. The bandwidth of the Raghu model is $W \simeq 12eV$ and we know that the relevant energy scale is $\propto \delta_o/W$, thus we choose a seemingly large $\delta_o = 100meV$ compared to what we were using for the Ikeda model, which has $W \simeq 4eV$ at the non-interacting limit. Apart from the bandwidth argument, another parameter determining this choice of δ_o is, again, the fact that we are making a qualitative study, so actual numbers are not so important at this point.

The addition of the nematic term in the Hamiltonian leads to a modification of the Fermi surface, as shown in Fig.4.14a. As it is expected, the electron pocket around X becomes larger, since the yz orbital, which is the dominant in that pocket, has lowered its energy. The opposite happens for the pocket around Y, which is related to the xz orbital. As a consequence of the FS reshaping, there is no guarantee that the susceptibility divergence will appear at the same points as it did in the normal state ($X = (\pi, 0), Y = (0, \pi)$). We know that now the system does not exhibit C4 symmetry, therefore it will pick a "preferred" direction, where the susceptibility peak will be larger. Already from the new FS form we expect that the peak will be on the x-axis, because in that direction there is better nesting, as shown schematically with the horizontal arrows in Fig.4.14a. Thus, the first step is to identify the new divergence point and we plot in Fig.4.14b the RPA spin susceptibility in the whole Brillouin zone. We see that indeed the largest value appears on the x-axis, however, it seems to emerge at a point prior to the X one. We plot in Fig.4.14c χ^s_{RPA} along the $\Gamma X M \Gamma$ path and we see that the divergence point is $(3.013, 0)$. Moving on, after identifying the susceptibility peak, we calculate the critical interaction for the magnetic instability. The result is shown in Fig.4.14d, from where we extract the critical value being $U_c = 3.0214eV$.

Now we are ready to proceed to the quasiparticle weight calculation and we do it for the central hole pocket located around the Γ point, where we take again eight points around the pocket as shown in the left part of Fig.4.13a. However, now C4 symmetry is broken, but there is C2 as well as reflection symmetry, thus those points are now related according to that. We see in Fig.4.15a that there are three sets of results, each of them containing information for more than one FS point. For example, the green data points corresponding to k_5, are also the results for k_1, since those points are related through a 180^o rotation. From the FS plot we know that the pocket around Γ is dominated by d_{xz} along the "right" and "left" areas, and by d_{yz} along the "up" and

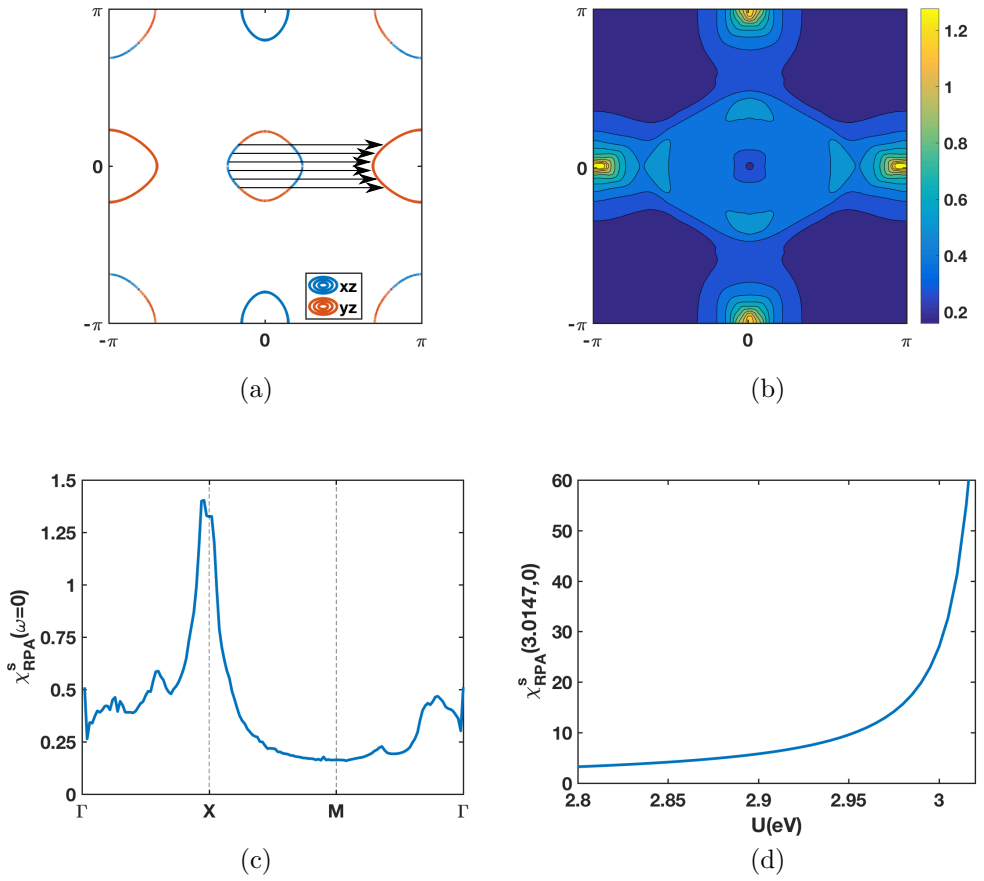

Figure 4.14: Nematic state with $\delta = 100meV$. (a) Reshaped Fermi surface, the electron pocket around X dominated by the yz orbital has become larger and the opposite happens for the one around Y dominated by xz. (b) Spin susceptibility on the Brillouin zone, where we identify the largest peak lying on the x-axis. (c) Spin susceptibility along the $\Gamma XM\Gamma$ path, with the peak appearing at (3.0147,0). The interaction used for (b) and (c) was $U = 2.5eV$. (d) Spin susceptibility as a function of interaction. The divergence related to the magnetic instability appears at $U_c = 3.0214eV$.

"down" areas. Therefore, the most straightforward way to compare the Z-factors of the two orbitals is to look at a FS point lying on the x-axis and one lying on the y-axis. We observe that the closer the system gets to the critical interaction for the magnetic transition, the largest the Z-factor difference among the various k-points becomes. We plot in Fig.4.15b the ratio between the quasiparticle weight on the k_1 point located on the x-axis and the k_3 one located on the inequivalent y-axis. Their ratio remains almost equal to 1 up until $U/U_c \approx 0.80$ and after that it drops rapidly becoming, for values very close to U_c, $Z_{k3}/Z_{k1} \approx 0.30$. Therefore, we understand that this effect is very sensitive to the distance from U_c and when this distance becomes significantly small the Z-factor discrepancy grows vastly.

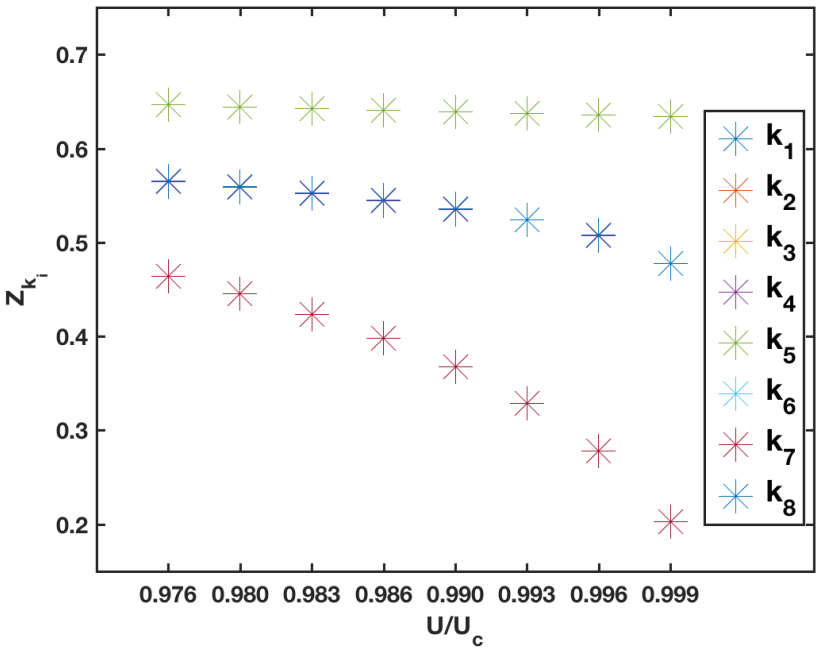

(a)

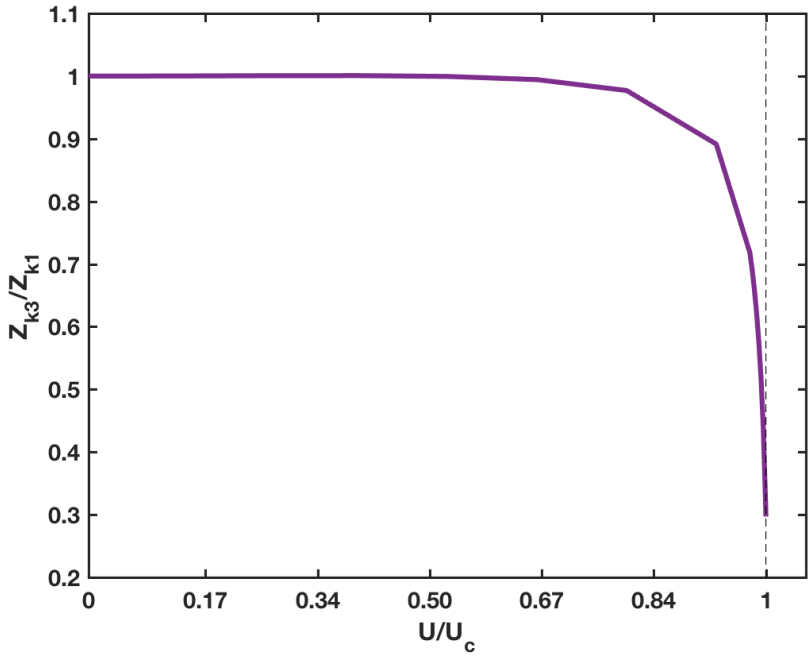

(b)

Figure 4.15: Nematic state with $\delta = 100meV$. (a) Quasiparticle weights as a function of U on eight k-points around the central FS pocket of Fig.4.14a, as illustrated in the left part of Fig.4.13a. We observe the increase in the Z-factor discrepancy between the k_5 and k_7 (equivalent to k_1 and k_3 points respectively) as the system approaches the magnetic transition. (b) Ratio of Z_{k3} and Z_{k1} versus interaction strength. At low U values the ratio is very close to 1, but by tuning up the interactions there is a sudden drop reaching $Z_{k3}/Z_{k1} \approx 0.30$ for U very close to U_c.

4.5 Discussion

In this chapter we explored the momentum dependence of the self-energy and extracted the quasiparticle weights accordingly, which in this case become k-dependent as well. Assuming that spin fluctuations are dominant, we used the RPA approximation to calculate the spin susceptibility and from that the self-energy. We showed that within this approach by increasing the interaction strength, the system becomes more and more correlated. This picture is in agreement with the results of the local mean-field slave spin technique and also with various experiments introduced in chapter 2. Next, we addressed the nematic state having in mind the analysis of the authors of [39] on FeSe, which suggested that a small difference in the energies of d_{xz} and d_{yz} is related to a large discrepancy in their quasiparticle weights. Following studies proposing that FeSe's nematic state is in proximity to a magnetic instability [35], we showed qualitatively that if the system's interactions are indeed very close to the critical U_c of the magnetic transition, then there is a rapid growth observed in the difference between the relevant Z-factors.

Chapter 5

Conclusion and outlook

In this thesis we discussed the role of electronic correlations in the iron-based superconductors. We introduced the existing theories related to the strength of those correlations and we presented relevant experiments, illustrating prominent effects of the FeSC.

More specifically we focused on three topics: (1) the strong mass renormalization and (2) orbital selectivity in the FeSC, as well as (3) the nematic phase of FeSe and its interesting properties. This material, in contrast to the usual FeSC, does not exhibit a magnetic ordering, but rather its nematic phase is present until low temperatures. In [39] that motivated our study on FeSe's nematicity, the authors suggest that the small energy splitting of the xz and yz orbitals in the nematic state, appears to induce a large difference in the two relevant quasiparticle weights. We tried to look into this peculiar result and find a way to interpret it by some physical mechanism. In order to address those three topics we needed to figure out the correct representation.

In the first project of the thesis, we implemented the slave spin technique in order to look into the strong electronic correlations. This is an approximate method including mean-field approaches. Using this technique, we showed that upon tuning up the interaction strength, the system becomes increasingly more correlated. Furthermore, including the orbital degree of freedom and looking at a realistic five band model, we proved the emergence of an orbital selective Mott phase, favored by Hund's coupling. There the FeSC system saturates in a state where the orbitals exhibit different renormalization and that is interpreted as a signal for co-existence of weakly and strongly correlated electrons. These results are in agreement with experimental findings. Moving on, we looked into the nematic state, in relation to the FeSe measurements. We achieved to reproduce the band-structure effects generated from the experimental data [39, 56, 57], but we were unable to show that they are related to a large discrepancy in Z_{xz} and Z_{yz}. Therefore, we considered some experimental and theoretical studies which suggest that FeSe's nematic phase is in proximity to a magnetic one [35], meaning that there are strong antiferromagnetic spin fluctuations and k-dependance becomes important. Thus, maybe the local slave spin approach is not the adequate one for the nematic phase of that material.

In order to account for spin fluctuations, we looked into the momentum dependence of the self-energy and accordingly extracted the quasiparticle weights. In this project, we applied a simplified two orbital model, thus we made a qualitative analysis. We proved that there is mass renormalization upon tuning up the interactions in the normal state, in agreement with the slave spin results. Following, we focused on the nematic state and we showed that indeed, if we use an interaction which is very close to the one inducing the magnetic instability, the Z-factors of d_{xz} and d_{yz} become

significantly different with their ratio being < 0.5, supporting the suggestion of [39].

Thinking into future perspectives, the obvious next step is to perform the self-energy calculation for a realistic five band model and try to obtain quantitative results. Another interesting path would be to estimate the self-energy in a self-consistent way. In our method we calculated Σ in a first order approach, however a more complete picture will be given with the self-energy entering the Green's function and then being calculated self-consistently. In this spirit, we could then utilize the Z-factor renormalized band-structure to study the spin density wave state and also the superconducting one. Furthermore, thinking in the slave spin technique, it would be very interesting to obtain results by including more sites. Incorporating a large grid would be numerically impossible, but using a small cluster with for example four sites could be feasible. That way we would break the locality of the slave spin approach (to some degree) and we would still make use of its advantage in reproducing orbital selectivity.

Appendices

Appendix A

Particle-hole symmetry

In the single band Hubbard model, with hopping only between nearest neighbors, we will show that the interaction Hamiltonian:

$$\hat{H}_{int} = U \sum_i n_{i\uparrow} n_{i\downarrow} \tag{A.1}$$

can be written in the equivalent form:

$$\hat{H}_{int} = \frac{U}{2} \sum_i \left(\sum_\sigma (n^d_{i\sigma} - \frac{1}{2}) \right)^2, \tag{A.2}$$

by rescaling the chemical potential, according to its value related to half-filling. We start with the full Hamiltonian:

$$\hat{H} = \sum_{ij\sigma} t_{ij} d^\dagger_{i\sigma} d_{j\sigma} + U \sum_i n_{i\uparrow} n_{i\downarrow} = \sum_{ij\sigma} t_{ij} d^\dagger_{i\sigma} d_{j\sigma} + U \sum_i d^\dagger_{i\uparrow} d_{i\uparrow} d^\dagger_{i\downarrow} d_{i\downarrow} \tag{A.3}$$

and we apply the particle-hole transformation:

$$\begin{aligned} d^\dagger_{i\sigma} &\to d_{i\bar{\sigma}} \\ d_{i\sigma} &\to d^\dagger_{i\bar{\sigma}}. \end{aligned} \tag{A.4}$$

The Hamiltonian transforms as follows:

$$\begin{aligned} \hat{H} - \mu \hat{N} &= \sum_{ij\bar{\sigma}} t_{ij} d_{i\bar{\sigma}} d^\dagger_{j\bar{\sigma}} + U \sum_i d_{i\downarrow} d^\dagger_{i\downarrow} d_{i\uparrow} d^\dagger_{i\uparrow} - \mu \sum_{i\bar{\sigma}} d_{i\bar{\sigma}} d^\dagger_{i\bar{\sigma}} = \\ &= -\sum_{ij\sigma} t_{ij\sigma} d^\dagger_{i\sigma} d_{j\sigma} + U \sum_i (1 - d^\dagger_{i\downarrow} d_{i\downarrow})(1 - d^\dagger_{i\uparrow} d_{i\uparrow}) - \mu \sum_{i\sigma} (1 - d^\dagger_{i\sigma} d_{i\sigma}) = \\ &= -\sum_{ij\sigma} t_{ij\sigma} d^\dagger_{i\sigma} d_{j\sigma} + U \sum_i (1 - d^\dagger_{i\uparrow} d_{i\uparrow} - d^\dagger_{i\downarrow} d_{i\downarrow} + d^\dagger_{i\downarrow} d_{i\downarrow} d^\dagger_{i\uparrow} d_{i\uparrow}) - \mu \sum_{i\sigma} (1 - d^\dagger_{i\sigma} d_{i\sigma}) = \\ &= -\sum_{ij\sigma} t_{ij} d^\dagger_{i\sigma} d_{j\sigma} + U - U \sum_{i\sigma} n_{i\sigma} + U \sum_i n_{i\uparrow} n_{i\downarrow} - 2\mu + \mu \sum_{i\sigma} n_{i\sigma} = \\ &= -\sum_{ij\sigma} t_{ij} d^\dagger_{i\sigma} d_{j\sigma} + U \sum_i n_{i\uparrow} n_{i\downarrow} + (\mu - U) \sum_{i\sigma} n_{i\sigma} + U - 2\mu. \end{aligned} \tag{A.5}$$

From this expression we can we see that for $\mu = U/2$ we obtain the initial Hamiltonian, which means that this is the value related to particle-hole symmetry. So, if we rescale

the chemical potential according to this value, we can end up with the equivalent expression for the interaction Hamiltonian:

$$\hat{H}_{int} = \frac{U}{2}\sum_i \left(\sum_\sigma (n^d_{i\sigma} - \frac{1}{2})\right)^2 = \frac{U}{2}\sum_i (n^d_{i\uparrow} + n^d_{i\downarrow} - 1)^2 =$$

$$= \frac{U}{2}\sum_i (n_{i\uparrow} + n_{i\downarrow} + 2n_{ni\uparrow}n_{i\downarrow} + 1 - 2n_{i\uparrow} - 2n_{i\downarrow}) =$$

$$U\sum_i n_{i\uparrow}n_{i\downarrow} - \frac{U}{2}\sum_i n_{i\uparrow} - \frac{U}{2}\sum_i n_{i\downarrow} + \frac{U}{2}, \tag{A.6}$$

where the last term $U/2$ is just a constant shift, not changing any physical properties of the Hamiltonian. This expression now implies that the chemical potential value related to half-filling will be $\mu = 0$. Note that in the above calculations we used the fermionic properties:

$$\{d^\dagger_{i\sigma}, d_{j\sigma'}\} = \delta_{ij}\delta_{\sigma\sigma'}$$
$$n^2_{i\sigma} = n_{i\sigma} \tag{A.7}$$

Appendix B

Spin-part of the composite SS operator

In the main text we define the composite operator of the slave spin representation as $d_{i\sigma} \to f_{i\sigma}O_{i\sigma}$ and accordingly $d^\dagger_{i\sigma} \to d^\dagger_{i\sigma}O^\dagger_{i\sigma}$, with $d_{i\sigma}$ being the annihilation operator of the original Hamiltonian. The operator $O_{i\sigma}$ is the spin-part of the composite one and in the main text we wrote it as:

$$O_{i\sigma} = \begin{pmatrix} 0 & c_{i\sigma} \\ 1 & 0 \end{pmatrix} = S^-_{i\sigma} + c_{i\sigma}S^+_{i\sigma}, \tag{B.1}$$

calling $O_{i\sigma}$ a generic spin-1/2 operator and letting $c_{i\sigma}$ being an arbitrary complex number. The reason behind this generic choice is that there is a number of possible operators that would act on the states in the correct way. We are going to show that indeed $O_{i\sigma}$, in the form we wrote it, is a valid choice. We know that the d-operator acting on the states of the original Hamiltonian gives:

$$d_{i\sigma}\big|n^d_{i\sigma}=0\big\rangle = 0, \quad d_{i\sigma}\big|n^d_{i\sigma}=1\big\rangle = \big|n^d_{i\sigma}=0\big\rangle, \tag{B.2}$$

$$d^\dagger_{i\sigma}\big|n^d_{i\sigma}=1\big\rangle = 0, \quad d^\dagger_{i\sigma}\big|n^d_{i\sigma}=0\big\rangle = \big|n^d_{i\sigma}=1\big\rangle. \tag{B.3}$$

Now if we apply the composite operator on the corresponding states in the enlarged space (as defined in the main text) we must get:

$$\begin{aligned}
&f_{i\sigma}O_{i\sigma}\big|n^f_{i\sigma}=0, S^z_{i\sigma}=-1/2\big\rangle = 0,\\
&f_{i\sigma}O_{i\sigma}\big|n^f_{i\sigma}=1, S^z_{i\sigma}=1/2\big\rangle = \big|n^f_{i\sigma}=0, S^z_{i\sigma}=-1/2\big\rangle \equiv \big|n^d_{i\sigma}=0\big\rangle,\\
&f^\dagger_{i\sigma}O^\dagger_{i\sigma}\big|n^f_{i\sigma}=1, S^z_{i\sigma}=1/2\big\rangle = 0,\\
&f^\dagger_{i\sigma}O^\dagger_{i\sigma}\big|n^f_{i\sigma}=0, S^z_{i\sigma}=-1/2\big\rangle = \big|n^f_{i\sigma}=1, S^z_{i\sigma}=1/2\big\rangle \equiv \big|n^d_{i\sigma}=1\big\rangle.
\end{aligned} \tag{B.4}$$

We will look at each of those equations one by one. The f-operator is a quasi-fermionic operator, so it satisfies all the above equations. In order for them to be correct, the spin operator needs to obey:

$$\begin{aligned}
O_{i\sigma}\big|S^z_{i\sigma}=1/2\big\rangle = \big|S^z_{i\sigma}=-1/2\big\rangle = \begin{pmatrix} O_{11} & O_{12} \\ O_{21} & O_{22} \end{pmatrix}\cdot\begin{pmatrix} 1 \\ 0 \end{pmatrix} = \begin{pmatrix} 0 \\ 1 \end{pmatrix}\\
\Rightarrow O_{11}\cdot 1 + O_{12}\cdot 0 = 0 \Rightarrow O_{11} = 0\\
O_{21}\cdot 1 + O_{22}\cdot 0 = 1 \Rightarrow O^*_{21} = 1
\end{aligned} \tag{B.5}$$

and:

$$O_{i\sigma}^{\dagger}\left|S_{i\sigma}^{z}=-1/2\right\rangle=\left|S_{i\sigma}^{z}=1/2\right\rangle=\begin{pmatrix} O_{11}^{*} & O_{21}^{*} \\ O_{12}^{*} & O_{22}^{*} \end{pmatrix}\cdot\begin{pmatrix} 0 \\ 1 \end{pmatrix}=\begin{pmatrix} 1 \\ 0 \end{pmatrix}$$
$$\Rightarrow O_{11}^{*}\cdot 0+O_{21}^{*}\cdot 1=0\Rightarrow O_{21}^{*}=1$$
$$O_{12}^{*}\cdot 0+O_{22}^{*}\cdot 1=0\Rightarrow O_{22}^{*}=0 \tag{B.6}$$

The other two equations are satisfied directly by the f-operator, leaving then O_{12} to be a free parameter. For that reason we end up with the general expression:

$$O_{i\sigma}=\begin{pmatrix} 0 & c_{i\sigma} \\ 1 & 0 \end{pmatrix}, \tag{B.7}$$

with $c_{i\sigma}$ an undefined complex number.

Appendix C

RPA susceptibility expression

We will derive the random phase approximation (RPA) susceptibility expression, given in the main text, using the equation of motion technique, following the derivation of [44]. We will derive the expression for the charge susceptibility and the spin one follows in the same way. We start by a generic Hamiltonian describing an electron gas:

$$H = H_0 + H_{int} = \sum_k \epsilon_k c_k^\dagger c_k + \frac{1}{2} \sum_{kk',q\neq 0} V_q c_{k+q}^\dagger c_{k'-q}^\dagger c_{k'} c_k, \tag{C.1}$$

where we have excluded the $q = 0$ term because it is cancelled by the positive background. Now we define the charge-charge correlation function:

$$\chi(q, t-t') = -i\theta(t-t') \sum_{kk'} \left\langle [(c_k^\dagger c_{k+q})(t), (c_{k'}^\dagger c_{k'-q})(t')] \right\rangle \tag{C.2}$$

Looking at the term $\chi_k(q, t-t')$ we calculate the equation of motion:

$$\begin{gathered} i\partial_t \chi_k(q, t-t') = \\ = \delta(t-t') \textstyle\sum_{k'} \left\langle [(c_k^\dagger c_{k+q})(t), (c_{k'}^\dagger c_{k'-q})(t')] \right\rangle - i\theta(t-t') \sum_{k'} \left\langle [-[H, c_k^\dagger c_{k+q}](t), (c_{k'}^\dagger c_{k'-q})(t')] \right\rangle. \end{gathered} \tag{C.3}$$

In order to proceed we will make use of the commutation relations:

$$[c_k^\dagger c_{k+q}, \rho(-q)] = c_k^\dagger c_k - c_{k+q}^\dagger c_{k+q},$$

$$[H_0, c_k^\dagger c_{k+q}] = (\epsilon_k - \epsilon_{k+q}) c_k^\dagger c_{k+q},$$

$$\begin{aligned} [H_{int}, c_k^\dagger c_{k+q}] = -\tfrac{1}{2} \textstyle\sum_{k',q'\neq 0} V_{q'} \{ & c_{k+q'}^\dagger c_{k'-q'}^\dagger c_{k'} c_{k+q} + c_{k'+q'}^\dagger c_{k-q'}^\dagger c_{k+q} c_{k'} - \\ & - c_{k'+q'}^\dagger c_k^\dagger c_{k+q+q'} c_{k'} - c_k^\dagger c_{k'-q'}^\dagger c_{k'} c_{k+q-q'} \}. \end{aligned} \tag{C.4}$$

In order to treat the last term we will now apply the random phase approximation (RPA), which is a mean field approximation, so:

$$c_\nu^\dagger c_\mu^\dagger c_{\mu'} c_{\nu'} \simeq c_\nu^\dagger c_{\nu'} \langle c_\mu^\dagger c_{\mu'} \rangle_{MF} + \langle c_\nu^\dagger c_{\nu'} \rangle_{MF} c_\mu^\dagger c_{\mu'} + const, \tag{C.5}$$

where we have neglected the exchange terms, which are related to a quantum correction. Now using RPA and writing $\langle c_k^\dagger c_{k'} \rangle = \langle n_k \rangle \delta_{k,k'}$, we transform to frequency space and the equation of motion takes the form:

$$(\omega + i\eta + \epsilon_k - \epsilon_{k+q}) \chi_k(q, \omega) = -\big(\langle n_{k+q} \rangle - \langle n_k \rangle\big) \left(1 - V_q \sum_{k'} \chi_{k'}(q, \omega) \right). \tag{C.6}$$

This is the expression for a specific k-point, so summing over k we obtain the final RPA equation:

$$\chi^{RPA}(q,\omega) = -\frac{1}{\mathcal{V}}\sum_k \chi_k(q,\omega) = \frac{1}{\mathcal{V}}\sum_k \frac{\langle n_k\rangle - \langle n_{k+q}\rangle}{\omega + \epsilon_k - \epsilon_{k+q} + i\eta}\big(1 + V_q\chi^{RPA}(q,\omega)$$

$$\chi^{RPA}(q,\omega) = \frac{\chi_0(q,\omega)}{1 - V_q\chi_0(q,\omega)}. \tag{C.7}$$

Bibliography

[1] H Kamerlingh Onnes. The resistance of pure mercury at helium temperatures. *Commun. Phys. Lab. Univ. Leiden*, 12(120):1, 1911.

[2] Vitalii L Ginzburg and Lev D Landau. On the theory of superconductivity. *Zh. eksp. teor. Fiz*, 20(1064-1082):35, 1950.

[3] J. Bardeen, L. N. Cooper, and J. R. Schrieffer. Theory of superconductivity. *Phys. Rev.*, 108:1175–1204, Dec 1957.

[4] J George Bednorz and K Alex Müller. Possible hightc superconductivity in the ba- la- cu- o system. *Zeitschrift für Physik B Condensed Matter*, 64(2):189–193, 1986.

[5] Md Atikur Rahman, Md Zahidur Rahaman, and Md Nurush Samsuddoha. A review on cuprate based superconducting materials including characteristics and applications.

[6] Yoichi Kamihara, Hidenori Hiramatsu, Masahiro Hirano, Ryuto Kawamura, Hiroshi Yanagi, Toshio Kamiya, and Hideo Hosono. Iron-based layered superconductor: Laofep. *Journal of the American Chemical Society*, 128(31):10012–10013, 2006.

[7] Johnpierre Paglione and Richard L Greene. High-temperature superconductivity in iron-based materials. *arXiv preprint arXiv:1006.4618*, 2010.

[8] Mark D Lumsden and Andrew D Christianson. Magnetism in fe-based superconductors. *Journal of Physics: Condensed Matter*, 22(20):203203, 2010.

[9] Ye Zi-Rong, Zhang Yan, Xie Bin-Ping, and Feng Dong-Lai. Angle-resolved photoemission spectroscopy study on iron-based superconductors. *Chinese Physics B*, 22(8):087407, 2013.

[10] DH Lu, M Yi, SK Mo, AS Erickson, J Analytis, David J Singh, Z Hussain, TH Geballe, Ian R Fisher, and ZX Shen. Electronic structure of laofep? a different type of superconductor. *Nature*, 455(7209), 2008.

[11] S Graser, TA Maier, PJ Hirschfeld, and DJ Scalapino. Near-degeneracy of several pairing channels in multiorbital models for the fe pnictides. *New Journal of Physics*, 11(2):025016, 2009.

[12] Douglas J Scalapino. A common thread: The pairing interaction for unconventional superconductors. *Reviews of Modern Physics*, 84(4):1383, 2012.

[13] Chao Cao, PJ Hirschfeld, and Hai-Ping Cheng. Proximity of antiferromagnetism and superconductivity in lafeaso 1- x f x: Effective hamiltonian from ab initio studies. *Physical Review B*, 77(22):220506, 2008.

[14] David J Singh and M-H Du. Density functional study of lafeaso 1- x f x: a low carrier density superconductor near itinerant magnetism. *Physical Review Letters*, 100(23):237003, 2008.

[15] II Mazin, David J Singh, MD Johannes, and Mao-Hua Du. Unconventional superconductivity with a sign reversal in the order parameter of lafeaso 1- x f x. *Physical Review Letters*, 101(5):057003, 2008.

[16] DN Basov and Andrey V Chubukov. Manifesto for a higher tc–lessons from pnictides and cuprates. *arXiv preprint arXiv:1104.1949*, 2011.

[17] Qimiao Si, Rong Yu, and Elihu Abrahams. High-temperature superconductivity in iron pnictides and chalcogenides. *Nature Reviews Materials*, 1:16017, 2016.

[18] Elena Bascones, Belén Valenzuela, and Maria José Calderón. Magnetic interactions in iron superconductors: A review. *Comptes Rendus Physique*, 17(1):36–59, 2016.

[19] Maria N Gastiasoro and Brian M Andersen. Competing magnetic double-q phases and superconductivity-induced reentrance of c 2 magnetic stripe order in iron pnictides. *Physical Review B*, 92(14):140506, 2015.

[20] Jiun-Haw Chu, Hsueh-Hui Kuo, James G Analytis, and Ian R Fisher. Divergent nematic susceptibility in an iron arsenide superconductor. *Science*, 337(6095):710–712, 2012.

[21] RM Fernandes, AV Chubukov, and J Schmalian. What drives nematic order in iron-based superconductors? *Nature physics*, 10(2):97, 2014.

[22] PJ Hirschfeld, MM Korshunov, and II Mazin. Gap symmetry and structure of fe-based superconductors. *Reports on Progress in Physics*, 74(12):124508, 2011.

[23] Qimiao Si, Elihu Abrahams, Jianhui Dai, and Jian-Xin Zhu. Correlation effects in the iron pnictides. *New Journal of Physics*, 11(4):045001, 2009.

[24] Qimiao Si and Elihu Abrahams. Strong correlations and magnetic frustration in the high t c iron pnictides. *Physical Review Letters*, 101(7):076401, 2008.

[25] John Hubbard. Electron correlations in narrow energy bands. In *Proceedings of the royal society of london a: mathematical, physical and engineering sciences*, volume 276, pages 238–257. The Royal Society, 1963.

[26] Luca de Medici, SR Hassan, Massimo Capone, and Xi Dai. Orbital-selective mott transition out of band degeneracy lifting. *Physical review letters*, 102(12):126401, 2009.

[27] NF Mott and R Peierls. Discussion of the paper by de boer and verwey. *Proceedings of the Physical Society*, 49(4S):72, 1937.

[28] MM Qazilbash, JJ Hamlin, RE Baumbach, Lijun Zhang, David J Singh, MB Maple, and DN Basov. Electronic correlations in the iron pnictides. *arXiv preprint arXiv:0909.0312*, 2009.

[29] Neil W Ashcroft and N David Mermin. Solid state physics (saunders college, philadelphia, 1976). *Google Scholar*, page 29, 2010.

[30] F Hardy, AE Böhmer, L De'Medici, M Capone, G Giovannetti, R Eder, L Wang, M He, T Wolf, P Schweiss, et al. Strong correlations, strong coupling, and s-wave superconductivity in hole-doped bafe 2 as 2 single crystals. *Physical Review B*, 94(20):205113, 2016.

[31] Qimiao Si. Iron pnictide superconductors: electrons on the verge. *Nat Phys*, 2009.

[32] Luca de Medici, Gianluca Giovannetti, and Massimo Capone. Selective mott physics as a key to iron superconductors. *Physical review letters*, 112(17):177001, 2014.

[33] Anna Tamai, AY Ganin, E Rozbicki, J Bacsa, W Meevasana, PDC King, M Caffio, R Schaub, S Margadonna, K Prassides, et al. Strong electron correlations in the normal state of the iron-based fese 0.42 te 0.58 superconductor observed by angle-resolved photoemission spectroscopy. *Physical review letters*, 104(9):097002, 2010.

[34] Ming Yi, DH Lu, Rong Yu, SC Riggs, J-H Chu, Bing Lv, ZK Liu, Minghui Lu, Y-T Cui, Makoto Hashimoto, et al. Observation of temperature-induced crossover to an orbital-selective mott phase in a x fe 2- y se 2 (a= k, rb) superconductors. *Physical review letters*, 110(6):067003, 2013.

[35] Qisi Wang, Yao Shen, Bingying Pan, Xiaowen Zhang, K Ikeuchi, K Iida, AD Christianson, HC Walker, DT Adroja, M Abdel-Hafiez, et al. Magnetic ground state of fese. *Nature communications*, 7, 2016.

[36] Peter J Hirschfeld. Using gap symmetry and structure to reveal the pairing mechanism in fe-based superconductors. *Comptes Rendus Physique*, 17(1):197–231, 2016.

[37] ZP Yin, K Haule, and G Kotliar. Spin dynamics and an orbital-antiphase pairing symmetry in iron-based superconductors. *arXiv preprint arXiv:1311.1188*, 2013.

[38] Markus Aichhorn, Silke Biermann, Takashi Miyake, Antoine Georges, and Masatoshi Imada. Theoretical evidence for strong correlations and incoherent metallic state in fese. *Physical Review B*, 82(6):064504, 2010.

[39] Peter O Sprau, Andrey Kostin, Andreas Kreisel, Anna E Böhmer, Valentin Taufour, Paul C Canfield, Shantanu Mukherjee, Peter J Hirschfeld, Brian Møller Andersen, and JC Séamus Davis. Discovery of orbital-selective cooper pairing in fese. *Science*, 357(6346):75–80, 2017.

[40] Andreas Kreisel, Brian M Andersen, Peter O Sprau, Andrey Kostin, JC Séamus Davis, and PJ Hirschfeld. Orbital selective pairing and gap structures of iron-based superconductors. *Physical Review B*, 95(17):174504, 2017.

[41] Shantanu Mukherjee, A Kreisel, PJ Hirschfeld, and Brian M Andersen. Model of electronic structure and superconductivity in orbitally ordered fese. *Physical review letters*, 115(2):026402, 2015.

[42] Nevill F Mott. The basis of the electron theory of metals, with special reference to the transition metals. *Proceedings of the Physical Society. Section A*, 62(7):416, 1949.

[43] Luca de Medici. HundâĂŹs coupling and its key role in tuning multiorbital correlations. *Physical Review B*, 83(20):205112, 2011.

[44] Henrik Bruus and Karsten Flensberg. *Many-body quantum theory in condensed matter physics: an introduction*. Oxford University Press, 2004.

[45] Gabriel Kotliar and Andrei E Ruckenstein. New functional integral approach to strongly correlated fermi systems: The gutzwiller approximation as a saddle point. *Physical review letters*, 57(11):1362, 1986.

[46] Luca de' Medici and Massimo Capone. Modeling many-body physics with slave-spin mean-field: Mott and hundâĂŹs physics in fe-superconductors. In *The Iron Pnictide Superconductors*, pages 115–185. Springer, 2017.

[47] L De Medici, A Georges, and S Biermann. Orbital-selective mott transition in multiband systems: Slave-spin representation and dynamical mean-field theory. *Physical Review B*, 72(20):205124, 2005.

[48] SR Hassan and L De Medici. Slave spins away from half filling: Cluster mean-field theory of the hubbard and extended hubbard models. *Physical Review B*, 81(3):035106, 2010.

[49] Rong Yu and Qimiao Si. U (1) slave-spin theory and its application to mott transition in a multiorbital model for iron pnictides. *Physical Review B*, 86(8):085104, 2012.

[50] AM Oleś. Antiferromagnetism and correlation of electrons in transition metals. *Physical Review B*, 28(1):327, 1983.

[51] S Raghu, Xiao-Liang Qi, Chao-Xing Liu, DJ Scalapino, and Shou-Cheng Zhang. Minimal two-band model of the superconducting iron oxypnictides. *Physical Review B*, 77(22):220503, 2008.

[52] Hiroaki Ikeda, Ryotaro Arita, and Jan Kuneš. Phase diagram and gap anisotropy in iron-pnictide superconductors. *Physical Review B*, 81(5):054502, 2010.

[53] L Fanfarillo and E Bascones. Electronic correlations in hund metals. *Physical Review B*, 92(7):075136, 2015.

[54] K Haule and G Kotliar. Coherence–incoherence crossover in the normal state of iron oxypnictides and importance of hund's rule coupling. *New journal of physics*, 11(2):025021, 2009.

[55] Takahiro Misawa, Kazuma Nakamura, and Masatoshi Imada. Ab initio evidence for strong correlation associated with mott proximity in iron-based superconductors. *Physical review letters*, 108(17):177007, 2012.

[56] Y Suzuki, T Shimojima, T Sonobe, A Nakamura, M Sakano, H Tsuji, J Omachi, K Yoshioka, M Kuwata-Gonokami, T Watashige, et al. Momentum-dependent sign inversion of orbital order in superconducting fese. *Physical Review B*, 92(20):205117, 2015.

[57] T Shimojima, Y Suzuki, T Sonobe, A Nakamura, M Sakano, J Omachi, K Yoshioka, M Kuwata-Gonokami, K Ono, H Kumigashira, et al. Lifting of xz/yz orbital degeneracy at the structural transition in detwinned fese. *Physical Review B*, 90(12):121111, 2014.

[58] Qisi Wang, Yao Shen, Bingying Pan, Yiqing Hao, Mingwei Ma, Fang Zhou, P Steffens, Karin Schmalzl, TR Forrest, Mahmoud Abdel-Hafiez, et al. Strong interplay between stripe spin fluctuations, nematicity and superconductivity in fese. *arXiv preprint arXiv:1502.07544*, 2015.

[59] MC Rahn, RA Ewings, SJ Sedlmaier, SJ Clarke, and AT Boothroyd. Strong (π, 0) spin fluctuations in β- fese observed by neutron spectroscopy. *Physical Review B*, 91(18):180501, 2015.